SEARCH FOR NEW PHYSICS IN THE EXCLUSIVE $\gamma_{DELAYED}$ + MISSING TRANSVERSE ENERGY CHANNEL IN $P\bar{P}$ COLLISIONS AT $\sqrt{S} = 1.96$ TEV

A Thesis

by

JONATHAN ABRAHAM ASAADI

Submitted to the Office of Graduate Studies of
Texas A&M University
in partial fulfillment of the requirements for the degree of

DOCTOR OF PHILOSOPHY

August 2012

Major Subject: Physics

SEARCH FOR NEW PHYSICS IN THE EXCLUSIVE $\gamma_{DELAYED}$ + MISSING TRANSVERSE ENERGY CHANNEL IN $P\bar{P}$ COLLISIONS AT $\sqrt{S} = 1.96$ TEV

A Thesis

by

JONATHAN ABRAHAM ASAADI

Submitted to the Office of Graduate Studies of
Texas A&M University
in partial fulfillment of the requirements for the degree of

DOCTOR OF PHILOSOPHY

Approved by:

Chair of Committee,	David Toback
Committee Members,	Guy Almes
	Bhaskar Dutta
	Ricardo Eusebi
Head of Department,	George Welch

August 2012

Major Subject: Physics

ABSTRACT

Search for New Physics in the Exclusive $\gamma_{Delayed}$ + Missing Transverse Energy Channel in $p\bar{p}$ collisions at $\sqrt{s} = 1.96$ TeV. (August 2012)

Jonathan Abraham Asaadi, B.S, University of Iowa; M.S., Texas A&M University

This dissertation presents the results of a search in the exclusive photon plus missing transverse energy (γ+ $\not\!\!E_T$) final state in proton antiproton collisions at a center of mass energy of 1.96 TeV using the Collider Detector at Fermilab experiment. The strategy used here is to search for delayed photons coming from gauge mediated supersymmetric events with the exclusive production of $\tilde{\chi}_1^0 \rightarrow \gamma\tilde{G}$. In these models the $\tilde{\chi}_1^0$ is the lightest neutralino and has nanosecond lifetime before decaying to a photon (γ) and gravitino ($\tilde{G}$) which exits the detector unrecorded. In order to search for this process we select collisions that have a single photon plus missing transverse energy and little other activity in the detector and examine the arrival time of the photon. This arrival time is then compared against expectations from a data driven background of the standard model sources. In the data collected from the Fermilab Tevatron collider from December 2004 to June 2010, representing 6.3 fb^{-1} of data, we observe 322 events in the photon arrival timing region from 2 nanoseconds to 7 nanoseconds with a data driven background prediction of 257 $\pm$ 35. An excess of 65 events is observed, equivalent to a standard deviation (N_σ) of 1.65 from the null hypothesis.

ACKNOWLEDGMENTS

There are a great many people to whom I owe an enormous debt of gratitude when it comes to the completion of this body of work. As in most science, and most especially High Energy Physics, no one accomplishment can happen without the endless support and work of countless people who came before me. To their effort in the building, operation, and maintenance of the Fermilab Tevatron collider and the CDF detector, without which no part of this thesis would have been possible, I offer my deepest thanks and appreciation. As it is impossible to mention each person and their work that ultimately went into the making of this thesis, I would like to thank a few select people who have supported me directly during my time working on this analysis.

Dave Toback, my advisor for nearly eight years, has been a mentor, leader, and friend at a level that is rarely found anywhere in this world. I am forever in debt to this man who has helped shape me as a scientist and helped lead me throughout my formative years of my twenties. He has always made time to listen to my thoughts and concerns, both professional and personal, and has offered advice that is been both profound and timely. Dave has kept me on track to becoming a scientist and has always been there to give me a friendly nudge or a hard kick in the pants when I started to stray too far. I am very proud to have my training under such a great scientist and human being and hope that one day I will be able to make him even one-tenth as proud of me and my career.

There are a number of people at Texas A&M University to whom I would like to offer special thanks. I am grateful to Bhaskar Dutta, Ricardo Eusebi, and Guy Almes for serving on my committee and their work in contributing to my research, course work, and time at Texas A&M. I also want to thank Teruki Kamon for all his time, guidance, and support and Sherry Yennello for serving on my masters committee and contributing to my research. A special thanks needs to be made to Peter McIntyre

with whom I did a summer research program with as an undergraduate and without whom I would have never attended Texas A&M, would not have made it through my first year of graduate school, and would have never met my advisor. Additionally, a large sentiment of gratitude is owed to the staff in the physics department who offer their support to all students who pass through their doors. Specifically I would like to thank Sandi Smith, Minnette Bilbo, Scharlotte Jones, Cheryl Picone, and Heather Walker who at various times during my graduate student career have been of enormous help.

There are also a long list of graduate students and post-docs throughout my time at Texas A&M and Fermilab who have been of the highest support and to which I owe a great deal. Firstly, I must express recognition to Adam Aurisano a fellow graduate student and friend who has worked on this project with me throughout my entire time. Joining A&M in the same year, Adam has been an inspiration of brilliance and hard work as well as a great friend and co-worker. His work is found throughout these pages and any credit that is gained through this work is as much his as my own. Additionally I need to thank Dr. Daniel Goldin and Dr. Jason Nett for their work and time on this thesis subject and helping propel me to finish this very difficult analysis.

My friends Dr. Alfredo Gurrola, Dr. Andrey Elagin, Dr. Eunsin Lee, Dr. Vadim Khotilovich, Dr. Peter Wagner, Lucas Naveria, and Michael Cone as well as many others in the physics department helped to make my life full and rewarding during these last eight years and I thank you all. While at Fermilab I have also had the good fortune to meet and work with Dr. Ron Moore and Dr. Homer Wolfe both of whom have become good friends and serve as mentors and models of great scientists that I strive to become.

Finally I need to thank my family for their unending support and love throughout my life. To my mother Jane Asaadi who instilled in me a great curiosity at a young age and always took time to listen to me I owe my life and undying love. To my father

Mohammad Asaadi who taught me to aim high, sacrifice, and work hard; I would be nothing of the man I have become without his life long support and I will never be able to repay that debt. My brother Robert Asaadi who has been an inspiration to me in his own academic endeavors as well as a friend unlike any other. My sister Sheila Asaadi who has shown me love and unwaivering support I am very grateful. Lastly, but not leastly, my wife Heather Asaadi who has driven me to become the man I have wanted to be. Thank you for supporting me despite this taking much longer then I would have ever guessed and being an amazing wife and friend. I love you Heather more then you will ever know.

TABLE OF CONTENTS

Page

Page

Page

LIST OF TABLES

TABLE Page

TABLE Page

TABLE Page

LIST OF FIGURES

FIGURE Page

FIGURE Page

FIGURE Page

FIGURE Page

FIGURE Page

FIGURE Page

FIGURE Page

FIGURE Page

FIGURE Page

FIGURE Page

FIGURE Page

FIGURE Page

1. INTRODUCTION

1.1 Overview

Since time immemorial, mankind has struggled to discover deeper and more fundamental laws associated with the natural phenomena that is observed in nature. In the 20th century this struggle turned to the science of particle physics as the focus of the search for a Grand Unified Theory of all the constituents of matter and their associated forces [1]. More so, the task of testing theories against experimental data and picking the ones that are the most consistent with what is observed and rejecting those that fail such tests has lead to the formation of what is known as the Standard Model of particle physics [2].

Much as Dmitri Mendeleev's table of periodic elements allowed us to understand and predict an enormous amount of phenomena in chemistry, the Standard Model has proven to be overwhelmingly successful for phyics. However, just as we now know that Mendeleev's table was not the fundamental theory of atoms, we believe the Standard Model is not the fundamental theory of particles and their forces and thus must be modified or extended in some way. This belief and its possible ramifications will be explored further in subsequent sections.

Any new theory of particle physics must be capable of making predictions about observable new phenomena, and it is these predictions that we turn our attention to in this thesis. One such prediction, made by a contending theory that extends the Standard Model, is that in experiments where we collide high energy particles, there should exist the possibility of,as yet undiscovered, new particles and/or interactions. During these high energy experiments one could produce one or more collisions (or events) that "differs" from expectations of the Standard Model.

While scientists have been performing such experiments for many years [3], history suggests that many discoveries come from the application of a new tool which allows scientists to consider information previously unavailable. In our case, we have

collisions of high energy particles, at the time the highest available to man, and a detector surrounding the collision that is able to measure the time of arrival of photon (the particles of light) to a precision of just over a half a nanosecond. There are compelling extensions of the Standard Model that predict new particles that have a significantly long lifetime (many nanoseconds). These particles lifetime is long when measuring the arrival time of their decay they would exhibit a time of arrival at the detector which would appear delayed. The details of example theories that might produce such a set of events, as well as our search for events that contain this unique signature, constitutes the majority of the remaining pages of this thesis.

While there are compelling theoretical reasons to look for this experimental signature, in point of fact, the model we are testing is the Standard Model. In order to do this we must first understand the predictions of the SM and thereby understand the model itself in some more detail. In the next section we will present a discussion of the Standard Model of particle physics and some of its known limitations, specifically with an eye towards potential solutions and extensions as well as ways of testing these extensions. Said colloquially, "Once you know the 'rules' of the game we can see if nature has 'changed' any of them."

Before we go further, it is useful to give a more complete description about the full path we will take together. Once we are done with our description of the SM we will describe more about some of the models of most interest to us from both a theoretical and experimental point of view. These models include both the Higgs Mechanism and Supersymmetry, both of which will be described in later sections. With these ideas we look at previous searches for evidence for these models as well as places which are not yet covered by previous experiments. Of particular interest will be a search from the Fermilab Tevatron, the worlds highest energy particle accelerator (at the time of data taking) that produced what could be naively interpreted as evidence for new physics. In this thesis we will discuss this original observation, and in the bulk of the this thesis, do a thorough and systematic study to see if this potential

hint is really evidence for new physics. With this in mind we begin our description of the Standard Model of Particle Physics.

1.2 Theory

In this section we take to the task of giving the details of these 'rules' known as the Standard Model. We begin Section 1.2.1 by providing an overview of this prevailing theory of particle physics known as the Standard Model. With this basis we next draw attention to known experimental and theoretical shortcomings of the Standard Model, in particular, the Higgs Mechanism of Electroweak Symmetry Breaking, with an eye towards potential extensions to the Standard Model. In Section 1.2.2 we put forward one potential extension to the Standard Model known as Supersymmetry. We analyze this theory with attention drawn toward the potential experimental ramifications of such an extension and provide a general overview of Supersymmetry. To allow us to make specific predicitions we must detail the aspects of one particular 'flavor' of theoretical model known as Gauge Mediated Supersymmetry Breaking in Section 1.2.3. All of this detail is provided such that the motivation for looking for evidence for new physics, as well as the basic theoretical underpinnings of collider based searches presented in Section 1.3, can be properly understood. Said in a slightly different way, if the Higgs Mechanism and Supersymmetry (or theories like them) were true in nature, what type of collisions might we expect to see in high energy experiments that we would not otherwise observe?

1.2.1 The Standard Model of Particle Physics

The Standard Model of particle physics, here after denoted by SM, is a theory that describes the known elementary particles and their interactions [1]. The SM asserts that the material which makes up the visibly observable universe is made of

This thesis follows the style of Physical Review Letters D.

elementary particles interacting through fields as well as the particles associated with those interaction fields. This theory successfully describes three of the fundamental forces: the strong nuclear force, the weak nuclear force, and the electromagnetic force; the three of which are responsible for the vast majority of interactions (gravity is excluded) between elementary particles [2].

As shown in Figure 1.1 the SM contains three generations of spin $\frac{1}{2}$ (e.g. $\frac{1}{2}$,$\frac{3}{2}$,$\frac{5}{2}$...) particles called Fermions that make-up the basic constituents of atomic matter. For every fermion there is an associated, so called, "anti-fermion" that possesses the same mass but opposite quantum numbers. These fermions interact with each other via the exchange of the gauge bosons representing the fundamental forces listed on the right hand side of Figure 1.1. The fundamental forces correspond to four integer spin (e.g. 1,2,3..) vector gauge bosons particles which act as the carriers of the various interactions between the particles. These bosons are the photon (electromagnetic force), the gluon (strong force), and the W and Z bosons (weak force).

In mathematical terms, the SM interactions can be described by a local symmetry group of $SU(3)_C \times SU(2)_L \times U(1)_Y$, where $SU(3)_C$ describes the strong force interaction through the coupling of the quarks to the $SU(3)$ gluon particles that carry "color charge" (hence the subscript C) in a theoretical framework known as Quantum Chromodynamics (QCD) [4, 5]. The $SU(2)_L \times U(1)_Y$ terms correspond to the electromagnetic and weak interaction (Electroweak Theory) [6–8] and the couplings to the photon and the W and Z boson with the subscript L denoting the weak current and Y denoting "weak hypercharge". However, we observe the weak force and the electromagnetic force as separate; thus the $SU(2)_L \times U(1)_Y$ symmetry is observed to be broken [8]. It is thus postulated that this symmetry is spontaneously broken by a fundamental scalar field, the Higgs field [9]. This symmetry breaking mechanism, while not verified in experiment yet, gives rise to the familiar mass eigenstates for the gauge bosons, such as the W and Z, and establishes the correlation between

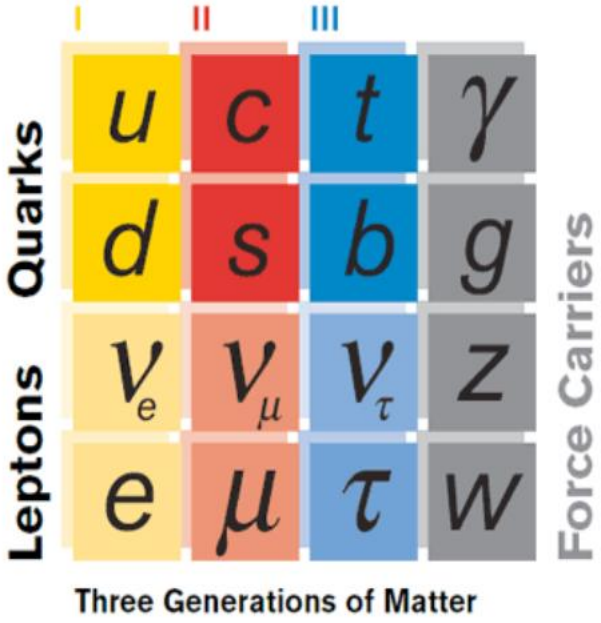

Fig. 1.1. The particles that comprise the Standard Model are arranged into three generations and the interactions between them are communicated by the exchange of the force carrying particles.

charge as we conventionally know it (Q) and "weak hypercharge". These quantities are thus what we measure experimentally [3] and are summarized in Table 1.1.

The mechanism by which electroweak symmetry breaking occurs will be discussed further in the next section, but has long been thought to be by the Higgs mechanism [9]. While the effects of a Higgs mechanism have been verified to a high degree of measurements [3], the particle corresponding to fundamental scalar field (namely, the Higgs boson itself), a primary prediction of the theory, has not yet been observed. For now it is sufficient to remark that the Higgs field can be thought of as a sort-of viscous fluid that all particles have to constantly travel through and the resulting *drag* is what can be thought of as the particle's mass. This field gives rise to an, as yet unobserved, Higgs boson whose couplings to the particles are proportional to their mass [10].

Particle	**Symbol**	**Mass** ($\mathrm{MeV/c^2}$)
Quarks		
Up	u	1.5 - 5
Down	d	3 - 9
Charm	c	1100 - 1400
Strange	s	60 - 170
Top	t	172000
Bottom	b	4100 - 4400
Leptons		
Electron	e	0.511
Electron neutrino	ν_e	$\sim$0 (but not identically 0)
Muon	μ	105.7
Muon neutrino	ν_μ	$\sim$0 (but not identically 0)
Tau	τ	1777.1
Tau neutrino	ν_τ	$\sim$0 (but not identically 0)
Bosons		
Photon	γ	0
W	W	80400
Z	Z	91200
Gluon	g	0

Table 1.1
Table of the Standard Model particles, their symbols, and their measured mass.

The SM is seen as a very successful theory in both precision measurement as well as predicting new particles [11], but there are several theoretical and experimental shortcomings that suggest that it is simply a low-energy approximation to a more fundamental theory. Examples of experimental results that do not immediately fall into the SM come from a variety of measurements. One such example is the observation of neutrino oscillation [12] suggesting that the neutrinos are not in fact massless as predicted by the standard model. Another such measurement is the $\sim 3.4\sigma$ deviation from SM prediction of the muon magnetic moment, $g-2$, observed in experiment [13]. Perhaps the most astounding, is that current cosmological obser-

vations imply that the visible matter in the universe that is described by the content of the SM only constituents ∼5% of the known universe [14, 15].

In addition to these experimental results, an important potential theoretical shortcoming of the SM lies with the Higgs mechanism itself. For instance, the calculation of the Higgs mass in the theory leads to radiative corrections that cause the mass to diverge and is known as the "hierarchy" or "naturalness" problem [17]. These problems are so named because the values computed for the Higgs mass are wildly larger ($\sim 10^{14}$ GeV) then what is observed for the electroweak scale breaking ($\sim 10^{2}$ GeV) thus putting a large "hierarchy" into the theory and making the predicitions lack "naturalness". Without some sort of "ultra-violet cutoff" to the diverging mass calculation this will cause the theory to become not self-consistent. This problem is discussed further in the following section as well as a theoretical solution which can solve some, but not all, of the above described experimental shortcomings of the Standard Model.

1.2.2 Higgs / Supersymmetry Theory

Higgs

The Electroweak Theory requires four gauge bosons (W^+, W^-, Z, γ) all of which would have to be massless in order that the SM be invariant under gauge transformations [6–8]. However, it is experimentally known that while this is true for the photon, the W and Z bosons are massive [3] and any straightforward attempt to add a mass term breaks the gauge symmetry and is thus not allowed. As mentioned before, an elegant solution known as spontaneous symmetry breaking, by which one can introduce massive gauge bosons for the weak interaction without breaking the $SU(2)_L \times U(1)_Y$ invariance. This method of spontaneous symmetry breaking is known as the "Higgs mechanism" [9].

The "Higgs mechanism", by which electroweak symmetry is broken, is the ansatz that this gauge invariant theory undergoes this spontaneous symmetry breaking as the Higgs potential reaches a non-zero value for the introduced scalar field, known as the Higgs field. Figure 1.2 is a schematic drawing of what the Higgs potential looks like (colloquially referred to as the "mexican hat" potential) and thus provides a sense why the non-zero value for the potential spontaneously breaks the symmetry. Namely, since the minimum of the potential is no longer located at the center of this representation for the potential, the symmetry is broken when the particles go to the low energy state. In the SM this spontaneous symmetry breaking generates the mass terms for all the particles including the gauge bosons.

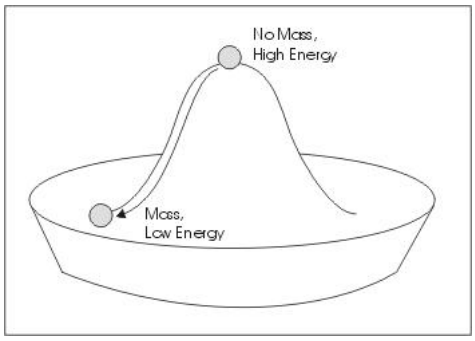

Fig. 1.2. Schematic of the Higgs potential energy demonstrating how the particles of the Standard Model obtain their mass.

In addition to giving mass to the gauge bosons, the Higgs mechanism also predicts a fundamental spin-0 particle known as the Higgs boson [9]. However, the theoretical mass of this boson is not uniquely predicted by the theory. It is in the calculation of this particles mass where aforementioned hierarchy problem arises.

Specifically, the hierarchy problem can be seen when radiative corrections to the Higgs mass are calculated and have the basic form shown in Equation 1.1. Here, m^2_{Bare} is known as the "bare" Higgs mass and δm^2_H is the sum of the corrections due to such radiative corrections shown in Figure 1.3.

$$m_H^2 = m_{Bare}^2 + \delta m_H^2 \tag{1.1}$$

where δm_H^2 can be written for a fermion of mass m_f as

$$\delta m_H^2 \approx \frac{\lambda_f^2}{4\pi^2}(\Lambda^2 + m_f^2) + ... \tag{1.2}$$

and λ_f is the coupling constant of the Higgs boson and Λ is the cut-off energy of the theory [1]. Unlike the fields describing all the other known particles, whose masses are protected by symmetry principles [1] that ensure the radiative corrections are only logarithmically divergent, the Higgs mass diverges quadratically when taking diagrams like Figure 1.3 into account [17]. In order to yield a Higgs mass of the order of 100 GeV, which is favored by the SM [18, 19] to preserve electroweak symmetry breaking, the bare Higgs mass is forced to be the same order of magnitude as the corrections, thus forcing the theory to be "fine-tuned" to an uncomfortable number of digits to keep the Higgs mass from becoming non-physical.

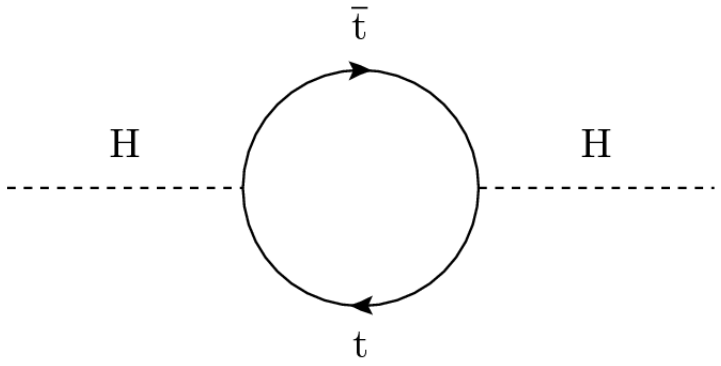

Fig. 1.3. An example of the one-loop quantum corrections from fermion loops (top quark shown here) to the Higgs mass leads that lead to a divergent Higgs boson mass without "fine tuning" in the theory. This is known as the "hierarchy" problem and presents compelling reason to believe that the Standard Model Higgs may not be the complete theory of electroweak symmetry breaking.

Since it seems unlikely that the theory of Electroweak Symmetry Breaking requires this remarkable fine-tuning of one of its physical parameters, physicists have sought other solutions which might reveal a more fundamental understanding. One particularly elegant solution comes by extending the symmetry of the theory further to a symmetry that relates the gauge particles (bosons) and the matter particles (fermions). This theory is known as supersymmetry (SUSY), and offers a solution to the hierarchy problem as well as having many other advantages. Particularly SUSY offers intriguing solutions to other shortcomings of the SM such as an explanation of the previously mentioned anomalous muon magnetic moment and the "dark matter" question [13–15]. While a complete discussion is beyond the scope of this thesis, it is worthwhile to note that SUSY (or something like it) is required for a most grand unified models such as String Theory [16].

On the flip side, it is important to note that the SUSY solution to the hierarchy problem is not without its potential downside. For example, it more than doubles the number of particles; as such it can hardly be said to be an "elegant solution" just on the surface. Furthermore, none of these new particles have been observed, although this makes this theory wonderfully testable at high energy experiments. With this in mind we move towards a description of SUSY.

Supersymmetry

Since SUSY is a compelling theory for many reasons, many independent of the Higgs mechanism, we describe it in some detail here. As we will see, SUSY is not just a single theory but a set of theories each of which have different advantages and disadvantages. We will focus on ones that help the Higgs mechanism, have the potential to solve other problems, and give experimental predictions that can be tested in high energy collisions.

The basic proposal of Supersymmetry [20] is that nature posseses a symmetry law that relates elementary particles of integer spin (e.g. 1,2,3,...) to particles of half

integer spin (e.g. $\frac{1}{2}, \frac{3}{2}, \frac{5}{2}...$). Said differently, SUSY implies that for every type of boson there exists a corresponding fermion partner and vice versa. Mathematically, this transformation can be achieved by having an operator Q that is an anti-commuting spinor [20–22] such that

$$Q\left|Boson\right\rangle = \left|Fermion\right\rangle, Q\left|Fermion\right\rangle = \left|Boson\right\rangle \tag{1.3}$$

where the theory is invariant under Q transformations. This requirement is satisfied by introducing additional supersymmetric fields which correspond to the supersymmetric partners of the SM particles and thus preserve the symmetries of the SM. The consequence of this is that the number of elementary particles is essentially (at least) doubled for minimal supersymmetric standard models (MSSM).

To simplify things, we adopt the standard naming convention for the supersymmetric partners of the standard model particles. For the partners of the fermions (leptons and quarks), we keep the same name but add an "s" to the front; they are thus referred to as "squarks" and "sleptons". The partners of the bosons (gauge bosons) receive an "ino" as a suffix and thus become "gauginos". Additionally, as can be seen in Figure 1.4, the symbols for the squarks, sleptons, and gauginos are the same as the corresponding fermion and boson with the addition of a "~" denoting the supersymmetric version of the particle with a few special cases described below.

The representation of the SUSY algebra that produces the particle content of MSSM are the so called 'supermultiplets' which effect on the mixing between the electroweak and mass eigenstates of the gauginos. The supermultiplets also contain both fermion and boson states for SM and SUSY particles in such a way that the number of degrees of freedom for fermions is the same as for bosons. As shown in Figure 1.4, SUSY theories require a minimum of two complex Higgs doublets rather than just one ordinary SM Higgs [21, 22]. The supersymmetric partner to these Higgs doublets (higgsinos) mix with the supersymmetric electroweak gauge particles (gauginos) because of the effects of the electroweak symmetry breaking, [20–22], such

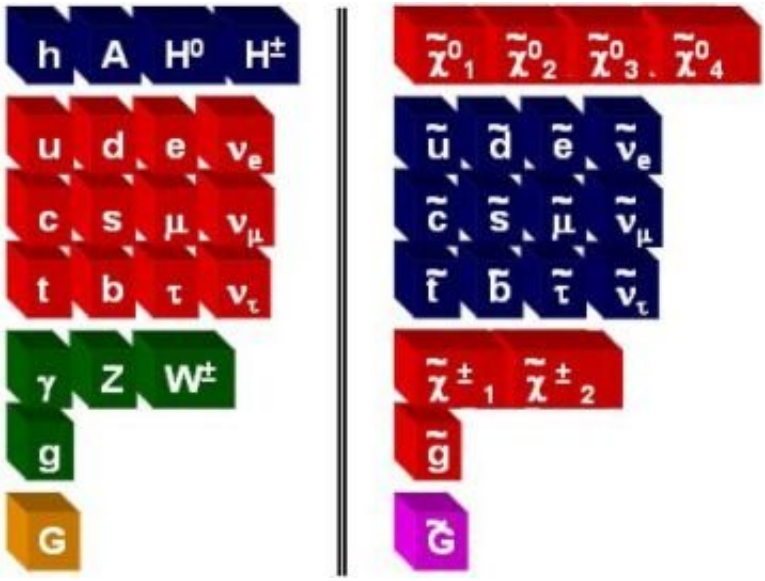

Fig. 1.4. The particles of the Minimal Supersymmtric Model (MSSM) extension to the Standard Model of particle physics.

that the neutral ones combine to form four mass eigenstates called the "neutralinos" ($\tilde{\chi}_i^0, i = 1, 2, 3, 4$) and the charged ones combine to form the "charginos" ($\tilde{\chi}_i^{\pm}, i = 1, 2$) shown in Figure 1.4 where the numbering i corresponds to the ordering of the mass eigenstates. Additionally SUSY also postulates the gravitino, the SUSY partner to the as-yet-undiscovered spin 2 boson graviton [20].

With a basic understanding of SUSY we can now come back to how SUSY can help solve the hierarchy problem. SUSY solves the hierarchy problem by introducing loop diagram corrections to the Higgs mass from the superpartner particles as shown in Figure 1.5 which gives corrections similar to those in Equation 1.2 but with opposite sign since they are now scalar loops, such as

$$\delta m_H^2 \approx -\frac{\lambda_{\tilde{f}}^2}{4\pi^2}(\Lambda^2 + m_{\tilde{f}}^2) + ... \tag{1.4}$$

These correction terms thus are enticingly close to being exactly what is needed to cancel out the quadratic divergences from δm_H^2 and thus solves the hierarchy problem [23].

However, this solution comes at a cost; namely this theory introduces new superpartner particles none of which have been discovered as of the writing of this thesis [3]. However, if SUSY was a perfect symmetry the SUSY particles would have the exact same masses as their SM counterparts and thus have been detected long ago [3]. Since this is a compelling solution, and there are other reasons to think SUSY might still be correct in nature, we move onto what we think is most likely to be true about SUSY in an attempt to help discover it. In the next sections we will consider the resonable assumption that SUSY is a broken symmetry whereby it is supposed that a spontaneous supersymmetry breaking takes place via some other field, since none of the fields in MSSM can develop a non-zero vacuum expectation without spoiling the gauge invariance of the theory.

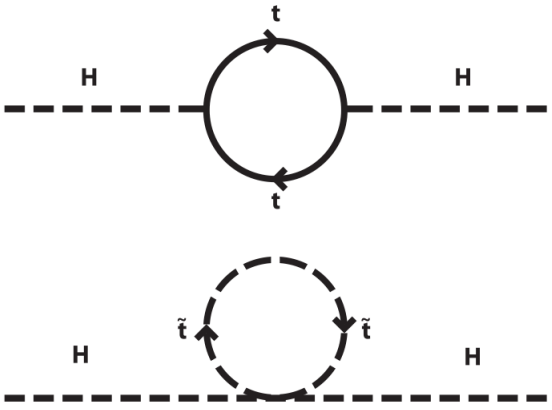

Fig. 1.5. One-loop quantum corrections to the Higgs mass leads to a divergence mass in the theory known as the "hierarchy" problem. In Supersymmetric extensions to the Standard Model the quantum corrections for fermions and their bosonic "SUSY-partners" have opposite signs and thus lead to a cancellation that prevents the Higgs mass from becoming divergent.

While the exact mechanism of SUSY breaking is not yet understood, a common and well motivated method of supersymmetry breaking is known as "hidden sector" symmetry breaking [27]. Hidden sector symmetry breaking is the idea that there is an ensemble of, as-yet-unobserved, quantum fields and particles that cause the breaking of supersymmetry. These quantum fields and particles would exist at much higher energies, would do not directly interact with the known lower energy SM, and thus remain "hidden". Only through a weak coupling of this "hidden sector" to the MSSM particles are the SUSY breaking terms introduced.

This description of SUSY breaking thus has two sectors, known as the "visible" sector (to which all the ordinary matter belongs) and the "hidden" sector (containing new fields and particles). The two sectors interact through the exchange of some "messenger" field that mediate the information about how the SUSY breaking occurs. It is to this mechanism that the next section describes in greater detail its implications on observables at collider experiments.

1.2.3 Gauge Mediated Symmetry Breaking

The non-observation of SUSY particles thus far in nature points to the fact that if SUSY exists it must be a broken symmetry. One possibility, and the central phenomenology focused on in this thesis, is that SUSY breaking originates in a "hidden sector", which is not further specified, and "mediates" the breaking through "messenger fields" to the "visible" sector. This type of breaking mechanism causes the fields that couple to the messenger field to acquire a vacuum expectation value, denoted as <F>, and thus give the masses to the MSSM fields dynamically via loop corrections [23]. A schematic view of this SUSY breaking mechanism, commonly referred to as "soft" SUSY breaking, is shown in Figure 1.6. An appealing consequence of this solution to SUSY breaking is that if it is spontaneously broken in the hidden sector, with no direct coupling to the Standard Model particles, one can avoid quadratic

divergences of the SUSY breaking terms [27] which plagued the Higgs mechanism of electroweak symmetry breaking.

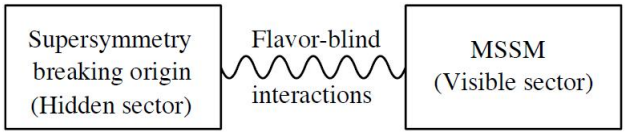

Fig. 1.6. Schematic of Gauge Mediated Supersymmetry Breaking.

Before we can move to predictions of SUSY in collider experiments, we note that a more complete description of the mechanism of soft SUSY breaking must be specified. While there are many theoretical ways that this symmetry breaking can occur [20,23], historically there have been two main competing theories for what the mediating interaction between the "hidden" sector and the "visible" sector may be. The first one of these approaches assumes that the mediation is due to gravitational interactions and is commonly referred to as minimal Supergravity (mSUGRA) symmetry breaking [28, 29]. The second possibility assumes that the mediation is due to the gauge interactions and is referred to as Gauge Mediated Supersymmetry Breaking (GMSB) [30–32].

While many searches for both types of models have been performed [3] and yielded null results up to the time of the writing of this thesis, the majority of collider searches have focused on mSUGRA type models owing to the prediction of a heavy dark matter candidate [33]. GMSB models provide a compelling alternative to mSUGRA models as well as having advantages such as natural suppression of "flavor" violating interactions [30–32]. "Flavor" is a common term to explain the assigning of quantum numbers to the various particles in the standard model such as lepton number, baryon number, isospin, etc. Simple flavor conservations have been observed in SM interactions [3], such as lepton number conservation, and thus any theory that can avoid "flavor" violation that has not been previously observed is seen as favorable.

With all these new particles and couplings there must be a mechanism to prevent the known stable particles from decaying away. For this reason, it is typically assumed that there is a new conservation law in SUSY. In particular a value known as "R-parity" is introduced where R is a quantum multiplicative number and defined as

$$R = (-1)^{3(B-L)+2s} \tag{1.5}$$

where B, L, and s represent the baryon, lepton, and spin of the particle respectively [24]. The reason for the introduction of this conservation principal is in the most general MSSM models there are terms introduced into the theory that allows the violation of baryon and lepton number. However, since both baryon and lepton number conservation have been tested to a high degree of precision [3]. This quantity is designed to be $R = +1$ for SM particles and $R = -1$ for the SUSY counterparts. Interestingly, if R-Parity is violated in the most general of ways such that all B and L violating terms are allowed this would imply that the proton would become unstable and decay in a very short period of time [25]. While this phenomenological consequence of proton decay can be avoided by introducing additional terms into the SM, it is generally thought to be more theoretically appealing to simply posit R-Parity conservation [26].

R-Parity being postulated to be conserved implies a number of important phenomenological consequences:

1. Any initial state created in laboratories using pairs of SM particles (such as colliders) has $R = +1$ and thus any SUSY particles created must be created in pairs.

2. All individual SUSY particles, which have $R = -1$, will decay (except the lightest supersymmetric particle) into a state that contains an odd number of SUSY particles.

3. The lightest supersymmetric particle (LSP) must be stable and cannot decay further into SM particles, thus making it a captivating candidate for dark matter if it is also electrically neutral [15].

GMSB models also offer distinctive phenomenological features that make them appealing for searches at particle colliders. One of these features is that the weakly interacting Gravitino ($\tilde{G}$), the supersymmetric partner of the as-yet-unobserved Graviton, is the lightest supersymmetric particle (LSP) and has a mass range of $\sim$eV/c^2 to $\sim$GeV/c^2 [30]. Another feature is the next-to lightest supersymmetric particle (NLSP) is often the neutralino ($\tilde{\chi}_1^0$) which can decay almost exclusively to via $\tilde{\chi}_1^0 \rightarrow \gamma\tilde{G}$ making for a very distinctive signature in high energy collider experiments. While not all versions of GMSB models have this distinctive signature, we describe our model parameters next and indicate which ones have this final state and give a feel for the regions of parameter space that give phenomenology.

Before proceeding further with the collider phenomenology of GMSB models, it is worthwhile to go into more detail as to the basic parameters used in most minimal GMSB models. This will aid in our understanding of previous searches performed at collider experiments which assume certain constraints based on these model parameters. Furthermore, since a great deal of data has been gathered on the masses and other characteristics of the SM particles, we list some of the current constraints that help us choose these parameters as well as bound their values.

For GMSB models the hidden sector particles are at a mass scale denoted as $\sqrt{F}$ and the messenger sector mass scale is given as M_{mess}. To avoid flavor breaking we require $M_{mess} > \sqrt{F}$, meanwhile M_{mess} is bounded on the other side as being below the Plank scale in order to realize SUSY breaking and help solve the hierarchy problem [35]. Thus, these values must be of the order of $\sqrt{F}$ $\approx$10 TeV/c^2 and M_{mess} $\approx$100 TeV/c^2 [35]. With this, as well as assumptions on charge-parity (CP) conservation, the number of free parameters in the minimal GMSB model are reduced from over one hundred free parameters of the MSSM to 6 free parameters which are:

1. N_{mess}**:** The number of messenger fields. We note that while this can have any value in principle, phenomenologically low values of N_m lead to the next-to lightest stable particle (NLSP) being the neutralino $\tilde{\chi}_1^0$.

2. $\Lambda = \frac{F}{M_{mess}}$**:** The mass scale of the visible sector of SUSY breaking. For sparticles with masses on the order of the electroweak scale Λ is on the order of 100 TeV / $\sqrt{N_{mess}}$.

3. M_{mess}**:** The overall messenger scale of the messenger sector. All the masses of the SUSY particles depend on M_{mess} logarithmically while the lifetime of the NLSP, which is important in this analysis, depends quadratically on M_{mess}.

4. tan β**:** The ratio of the vacuum expectation values of the Higgs. Large values of tanβ remove the $\tilde{\chi}_1^0$ from being the NLSP and thus remove the final state $\tilde{\chi}_1^0 \rightarrow \gamma\tilde{G}$ so we don't explore those scenarios any further. While the values can range from $1.5 < tan\beta < 60$ [35], for this analysis we consider small values of tan$\beta < \mathcal{O}(10)$.

5. sgn(μ)**:** This is the sign of the Higgs and Higgsino supersymmetric mass parameter μ. The absolute value of μ is determined by the electroweak breaking condition. Sgn(μ) is correlated with the sign of the MSSM correction to the anomalous magnetic moment of the muon, $g-2$, which is thus favored to be positive to account for this discrepancy [35].

6. C_{grav}**:** Represents the ratio between the scale of SUSY breaking and the scale of the intrinsic SUSY breaking parameter ($\frac{F_0}{F}$). This parameter contributes to the tuning of the gravitino mass and the NLSP lifetime.

Even though this parametrization of MSSM adopted within GMSB considerably simplifies the possible phenomenological scenarios, even a six-dimensional space is too broad to be covered by any single study at a high energy experiment. For this reason, great effort has been made to create sets of combinations of the parameters that all

have similar "types" of final states and phenomenologies at colliders. These model points, two of the most important are representative of the type which lead to the final state we are searching for in this analysis. At this point we will shift our focus away from general and minimal GMSB theory and focus more on collider phenomenology of two different GMSB model types that have been previously searched for as well as collider signatures which have yet to be excluded. This will help provide the final pieces of focus for where we will concentrate our effort, in particular in high energy collision events that produce a photon and a Gravitino in the final state.

1.2.4 GMSB Collider Phenomenology

In order to help simplify the GMSB parameter space we will refer to two types of models each of which have a unique collider phenomenology. Both models have $\tilde{\chi}_1^0 \to \gamma\tilde{G}$ in their final state, but can be divided by the various ways they produce this final state. Equally important, from the perspective of the detection of these final states, is a second bifurcation of the types into two subtypes which affect how they will detected. We will discuss both separately. The goal of understanding these differences in the phenomenology is to aid us in understanding the previous search results presented in the next section.

The most commonly discussed production models in the literature are ones where $\tilde{\chi}_1^0 \to \gamma\tilde{G}$ is produced at the end of a long decay chain. An agreed upon convention was arrived at during a workshop and is known as the Snowmass Points and Slopes (SPS) [36]. These are a set of benchmark points and parameters in which the MSSM parameters corresponding to different scenarios in SUSY that were formalized at the 2001 Snowmass Workshop on the Future of Particle Physics [36]. Of particular importance in this formulation is that the models have fixed mass relationships between the sparticles. This further simplifies the models and we are left with two free parameters: (1) The mass of one of the particles (all others are derived from there) and (2) the lifetime of the NLSP. Since the masses of the sparticles and their

couplings are well specified, this uniquely determines their production cross sections in different types of high energy collisions, as well as their and branching fractions and final state topologies.

A typical example of the resulting decay chain from an SPS-8 scenario for proton antiproton collisions at a center of mass energy of $\sim$2 TeV is shown in Figure 1.7 on the left hand side where the dominant production mode is chargino pair production [37]. As will be discussed further in the next section, for low lifetimes of the NLSP ($\tau_{\tilde{\chi}_1^0} << 1$ ps) both photons could be observed in the detector. Similar production and decay diagrams occur at LEP, Tevatron and the LHC (each with slightly different diagrams) and searches for these final states have been performed at LEP in reference [38], the Tevatron [39], and the LHC [41]. However, these models all assume SPS-8 type relations which keep the production cross-section high but also place constraints on the possible masses of the sparticles.

The second of these type of production mechanism comes from models where only the $\tilde{\chi}_1^0$ and the $\tilde{G}$ have masses low enough to be produced in collider experiments [43]. In these models the large direct sparticle production rates vanish. This scenario is important because they release these SPS-8 type relations such that seems to complicate the models. Most interestingly, the previous limits from LEP, the Tevatron, and the LHC no longer exclude these models because the production mechanisms which were favored in SPS-8 models no longer produce events, thus the limits are no longer relevant. Models of this sort are shown on the right hand side of Figure 1.7 and are referred to as the Light Neutralino and Gravitino (LNG) scenario in the literature [43]. Particularly relevant to the search performed in this thesis are models in which production of the lightest supersymmetric Higgs (h^0) and its decay to $\tilde{\chi}_1^0$ pairs is that the only substantive production of sparticles. The phenomenology of $h^0 \rightarrow \tilde{\chi}_1^0\tilde{\chi}_1^0$ in LGN models, where sparticle production is dominated by (h^0) events decaying to $\tilde{\chi}_1^0$ pairs, is significantly different from those seen in SPS-8 models which

produce $\tilde{\chi}_1^0$ pairs at the end of long decay chains. The final state is thus $\gamma\gamma\tilde{G}\tilde{G}$ plus little else.

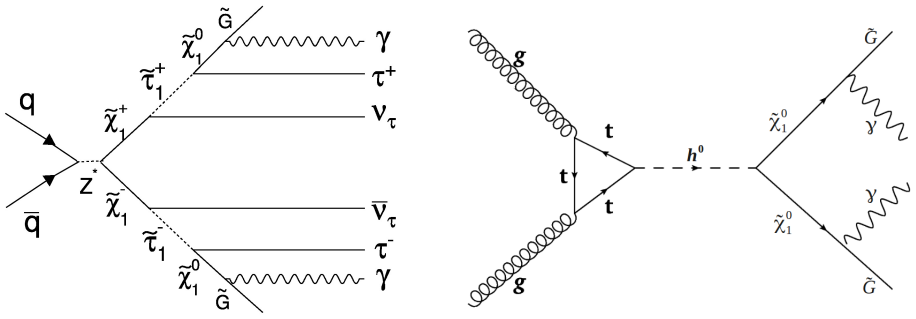

Fig. 1.7. Two example Feynmann diagrams illustrating SUSY $\tilde{\chi}_1^0$ $\tilde{\chi}_1^0$ pair production event that, in the simplest GMSB models, can produce a signal of a delayed photon and Missing Transverse Energy ($\not{E}_T$).

Equally important for experiments with high energy collisions is the finite size of the detector which makes the lifetime of the $\tilde{\chi}_1^0$ particularly important as it affects when and how the photon is produced. The $\tilde{\chi}_1^0$ lifetime ($\tau_{\tilde{\chi}_1^0}$) given by [44]:

$$c\tau_{\tilde{\chi}_1^0} = 48\pi \frac{m_{3/2}^2 M_{Pl}^2}{m_{\tilde{\chi}_1^0}|P_{1\gamma}|^2} \tag{1.6}$$

where $m_{3/2} = \frac{|F|}{\sqrt{3}M_{Pl}}$ and F is related to the value of the superpaticle masses and M_{Pl} is the Plank mass [20]. For theoretically resonable squark masses between 2 TeV and 10 TeV [20] bounds the typical lifetime ranges of 0.4 ns $< \tau_{\tilde{\chi}_1^0} <$ 180 ns for the $\tilde{\chi}_1^0$. This allows us to divide the possible production of $\gamma\gamma\tilde{G}\tilde{G}$ into three possible search prospects [37]. Namely:

1. $\tau_{\tilde{\chi}_1^0} << 1$ ns: In this case the photons from the decay of the $\tilde{\chi}_1^0$ are produced promptly and are thus too difficult to distinguish in time from photons from other sources in high energy collisions.

2. 1 ns $< \tau_{\tilde{\chi}_1^0} <$ 50 ns: This case the final state $\tilde{\chi}_1^0 \to \gamma\tilde{G}$ occurs at a displaced spatial location from the collision which produced the h^0 and causes the arrival time of the photon to be delayed relative to expectations from promptly produced photons. This scenario will be discussed in greater detail in the following section.

3. $\tau_{\tilde{\chi}_1^0} >$ 50 ns: In this scenario both $\tilde{\chi}_1^0$ pairs can travel a large distance before decaying and SUSY in this channel would not produce photons in a detector surrounding the collision point. Thus this scenerio be indistinguishable in typical collider experiments from other versions of SUSY (e.g. mSUGRA) and would be largely undetectable using direct methods.

These possibilities are what determine the last important part of the GMSB phenomenology in a detector. Namely, the question becomes whether the neutralinos will, typically, produce two promptly produced photons, one delayed photon or no photons in the detector. It is the second scenario that is the focus of this thesis where the $\tilde{\chi}_1^0$ has a long enough lifetime to produce a photon whose reconstructed time of flight will arrive later ("delayed") than a photon promtly produced by the collision.

At this point it is useful to introduce the notion of how measurements are made in high energy experiments. These ideas will be explained in much greater detail in Sections 2.1 and 2.2 but are useful here in order to obtain a basic understanding of how a search for long-lived neutral particles that decay to photons is performed.

The basic idea of how we produce high energy collisions comes from when two beams of energetic particles (e.g. protons and antiprotons) are made to intersect each other at a large center of mass energy. We surround the points where the beams are made to collide with large multi-purpose detectors (such as the CDF detector) that are capable of recording information relevant to the subsequent particles produced in the collisions. This information includes such quantities as energy, collision location, collision time, as well as the arrival time of the produced particles in the detector.

Since the collision occurs with approximately no momentum in the plane transverse to the collision we can infer, by conservation of momentum, the vector sum of the transverse momenta of the inital state particles should be approximately zero. Particles that do not interact with the calorimeter, such as neutrinos, can be inferred from the transverse energy imbalance of the detected particles in the collision. The measured missing transverse energy ($\not\!\!E_T$) is defined as the negative of the vector sum of the transverse energy measured in the detector. From this information it is possible to reconstruct and identify the particles produces in the collision as well as search for new particles such as those predicted in SUSY models.

Coming back to the GMSB phenomenology descibed above, we can now understand how these interactions can produce the case where one of the $\tilde{\chi}_1^0$s escapes the detector entirely making $\gamma_{delayed}+\not\!\!E_T$ final state the most sensitive channel [37]. Furthermore, since only $\tilde{\chi}_1^0$ pairs are produced, the final state must be what is known as exclusive $\gamma_{delayed}+\not\!\!E_T$. In this case, exclusive means that we expect little other activity in the detector to accompany the detection of the photon. A summary of the various scenarios described above and their resulting final states is given in Table 1.2.

	$\tau_{\tilde{\chi}_1^0} < 1$	$\tau_{\tilde{\chi}_1^0} \sim 5$
SPS-8	$\gamma\gamma+\not\!\!E_T + H_T$	$\gamma_{delayed}+\not\!\!E_T + Jet$
LGN	Exclusive $\gamma\gamma+\not\!\!E_T$	Exclusive $\gamma_{delayed}+\not\!\!E_T$

Table 1.2
Table of various final states resulting from SPS 8 models as well as LGN model types for $\tilde{\chi}_1^0$ lifetimes of interest in this analysis.

1.3 Previous Results for Collider Searches

Now that we have finished describing the basic properties of GMSB SUSY phenomenology, we now highlight a few of the searches previously performed for the various lifetimes in the SPS-8 scenarios. As part of this process we will describe the

differences between the various types of searches. This will useful as we move towards a better understanding of the search strategy employed in this thesis, specifically going after the topology for LNG with a lifetime in the 5 ns range. After we have completed this description we will detail a standard photon timing variable in Section 1.4, known as the corrected time, that allows powerful discrimination between SM sources of photons and photons that may originate from $\tilde{\chi}_1^0 \to \gamma\tilde{G}$. Finally, we will highlight an unpublished preliminary result in the exclusive $\gamma + \not{E}_T$ final state. This study was performed in 2008 and a very intriguing excess was found in the corrected timing distribution, the bulk of this thesis is dedicated to following up on this result.

Previous Searches and Model Constraints

The results of various searches from LEP and the Tevatron are shown in Figure 1.8 for SPS-8 type scenarios. This figure demonstrates the parameter space that has been constrained as a function of neutralino lifetime versus mass. A few words are in order about the searches that produced these results. We begin with the e^+e^- results from the Apparatus for Large Electron Positron PHysics (ALEPH) are a combination of direct searches for $\tilde{\chi}_1^0$'s as well as indirect searches for sleptons and chargino. In the direct searches for low lifetime $\tilde{\chi}_1^0$'s at ALEPH the channel $e^+e^- \to \tilde{\chi}_1^0\tilde{\chi}_1^0 \to \gamma\tilde{G}\gamma\tilde{G} \to \gamma\gamma + \not{E}_T$ was used where the neutralino lifetime was assumed less than 1 ns. This implies that the photons were required to originate directly from the beam line. In the case where the lifetime was assumed larger (1 ns$< \tau_{\tilde{\chi}_1^0} <$ 10 ns) the direct searchs at ALEPH would used photon "pointing" method [38]. Photon pointing measures the implied photon direction and extrapolates this direction to determine if the photon came from the center of the detector. No evidence for SUSY was observed in these searches with the limiting factor in the mass of the neutralino, as the center-of-mass energy for LEP was only 205 GeV. We also note that while these

scenarios were based on an SPS-8 like production, only the gauginos and sleptons were assumed to be light here.

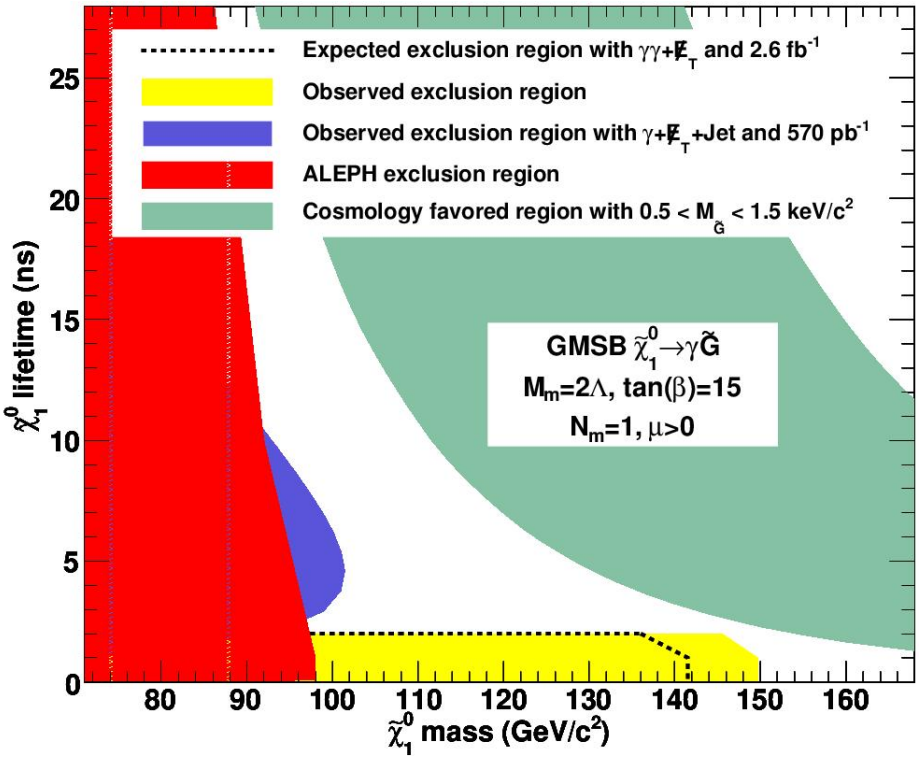

Fig. 1.8. The predicted and observed exclusion regions from the ALEPH detector at LEP as well as the previous GMSB photon searches at CDF. The green shaded bands shows the cosmologically favored region where $0.5 < m_{\tilde{G}} < 1.5$ keV/c^2 [39].

The low lifetime result ($\tau_{\tilde{\chi}_1^0}$ <1 ns), shown in yellow, as well as a long lifetime search (1 ns < $\tau_{\tilde{\chi}_1^0}$ <10 ns), shown in blue, are the result searches performed at CDF [39]. The low lifetime search was published in 2010 and assumed both $\tilde{\chi}_1^0$'s would decay inside the detector and the final state would appear as $\gamma\gamma + \not\!\!E_T$. The long lifetime search was performed in 2007 in the $\gamma + \not\!\!E_T + jet$ final state [39]. Recall both these CDF results assume SPS-8 model parameters and thus makes the dominant production of SUSY particles gaugino pair production. Figure 1.9 shows the results of another SPS-8 model style search for GMSB SUSY that was recently

performed (2010) at the Tevatron's D0 experiment searching for $\gamma\gamma + \not{E}_T$. This analysis set experimental exclusions as a function of Λ for GMSB models assuming a low lifetime scenario for the charginos and neutralinos [40]. Again, these results assume SPS-8 model parameters and thus make the dominant production of SUSY particles gaugino pair producion.

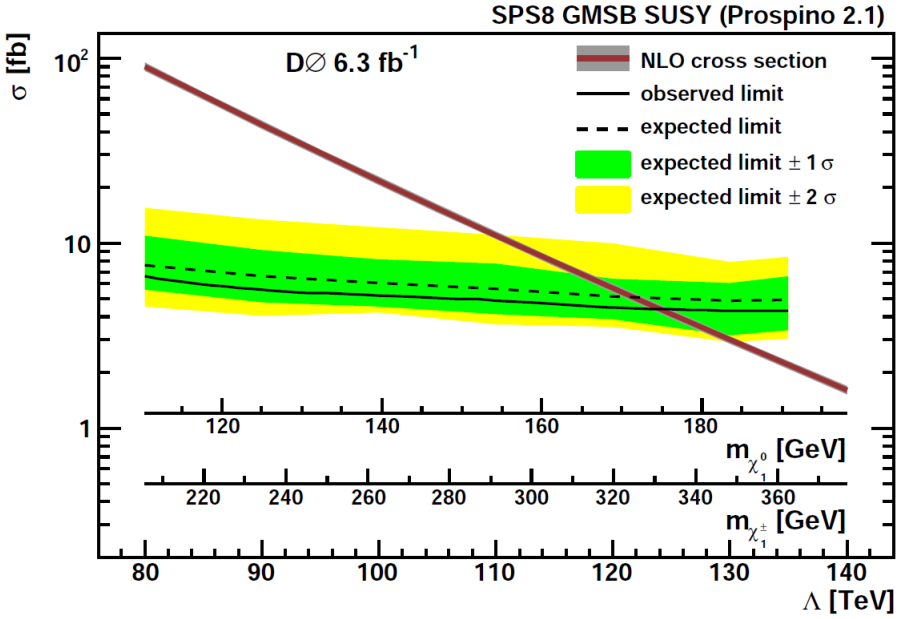

Fig. 1.9. The predicted cross section for the benchmark GMSB model $M_{mes} = 2\Lambda$, $N_{mes} = 1$ $tan(\beta) = 15$ and $\mu > 0$ and the 95% confidence limit expected and observed exclusion limit as a function of Λ from a search in $\gamma\gamma$ + missing energy performed at the $D\emptyset$ experiment in 2010. This search assumes SPS-8 model parameters and thus makes the dominant production of SUSY particles gaugino pair production. The corresponding masses are shown for the lightest chargino $\chi_1^{\pm}$ and neutralino χ_1^0 [40].

A similar result at even higher energies, but using different type production mechanisms is shown in Figure 1.10 performed at the Large Hadron Collider in 2010 and 2011 [41]. The exclusion presented here looks for the decay of $\tilde{\chi}_1^0 \rightarrow \gamma\tilde{G}$ produced in conjunction two hadronic jets and missing energy with the CMS detector. For $\tilde{\chi}_1^0$

lifetimes up to 3 ns the expected exclusion limit on neutralino mass is > 200 GeV/c^2 with 200 pb^{-1} of data at a center of mass energy of 7 TeV. While this search is also for SPS-8 models, it presumes a squark-gluino production unlike the searches at the Tevatron which assume gaugino pair production. Thus, while the parameter spaces shown for the searches are the same, the assumptions for the LHC searches are different.

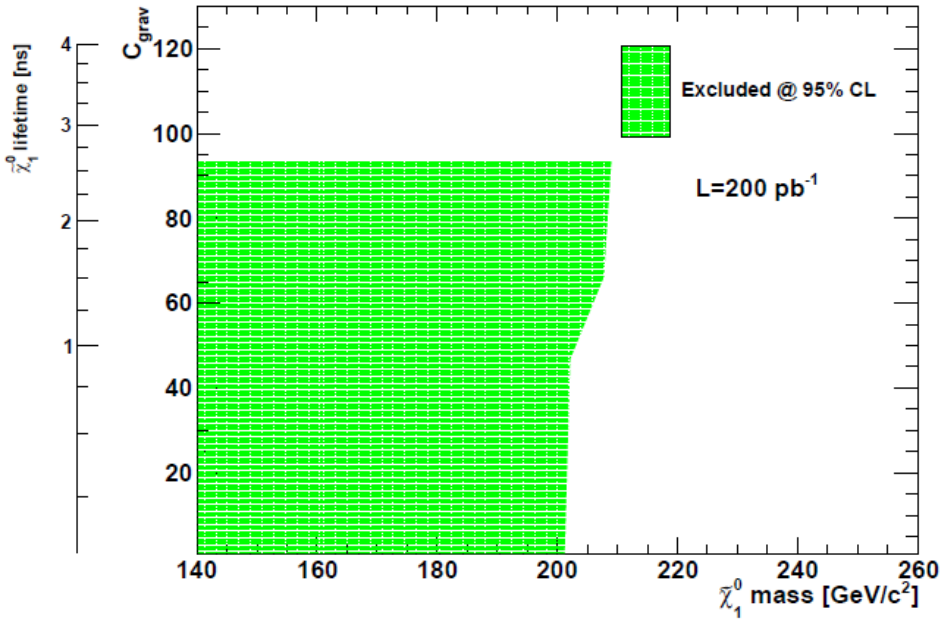

Fig. 1.10. The predicted exclusion regions from a GMSB search performed at the LHC in 2011 for lifetimes up to ∼3 ns for neutalino mass > 200 GeV/c^2 with 200 pb^{-1} of data. This search assumes SPS-8 model parameters but presumes squark-gluino production. This result supersedes the previous search performed at the Tevatron and LEP for low lifetime neutralinos.

While the searches described above go very far to exclude a great deal of minimal GMSB model scenarios, many of these limits may not apply if the assumptions made in the SPS mass hierarchies are relaxed. Thus, as we move out of the narrow SPS-8 interpretation these results can be considered to be covering different regions, or in

some sense complementary. However, we are left with the inescapable fact that there is no evidence for GMSB SUSY in either of these three sets of searches has been observed. That being said, we also notice that none of these searches cover models in the lower right hand side of Table 1.2. This leaves these models largely unsearched for and the limits discussed above do not apply. This provides a clear motivation to do a first search in the exclusive $\gamma_{delayed}$+$\not\!\!E_T$ final state as was first described in reference [43] and [37]. With clear vision of what types of models to focus on, we will go into more detail about for this analysis the central tool in the CDF detector; the timing measurement.

1.4 Overview of Searches for Long Lived Neutral Particles that Decay to Photons

Having motivated our search in the exclusive $\gamma_{delayed}$+$\not\!\!E_T$ final state, we turn to the details of how the search is done. We begin with the definition of a corrected timing variable used to calculate the arrival time of particles in the calorimeter. We then do a cursory summary of the typical backgrounds and their corrected time distributions as well as methods we will use in the exclusive $\gamma_{delayed}$+$\not\!\!E_T$ to measure and/or reject these backgrounds. This discussion will be especially useful as we look at some preliminary results in the next section.

Standard Photon Timing Variable

If GMSB models are correct, then a small fraction of high energy collisions should produce sparticles which will decay down to photons and missing transverse energy ($\not\!\!E_T$) in the final state. These photons may arrive in our detector "delayed" with respect to expectations from Standard Model backgrounds. To better quantify the term we look at a typical photon timing variable used known as corrected time of arrival [42], t_{corr}, defined as:

$$t_{corr} \equiv (t_f - t_i) - \frac{|\vec{x_f} - \vec{x_i}|}{c} \tag{1.7}$$

where $t_f - t_i$ is the time from the collision to the arrival time of the photon at the calorimeter, and $|\vec{x_f} - \vec{x_i}|$ is the distance between the collision and the position where the photon his observed. In Figure 1.11 we show in a schematic of what these variables are for both promptly produced photons as well as what these would look like for the production of a long-lived $\tilde{\chi}_1^0 \to \gamma\tilde{G}$ event.

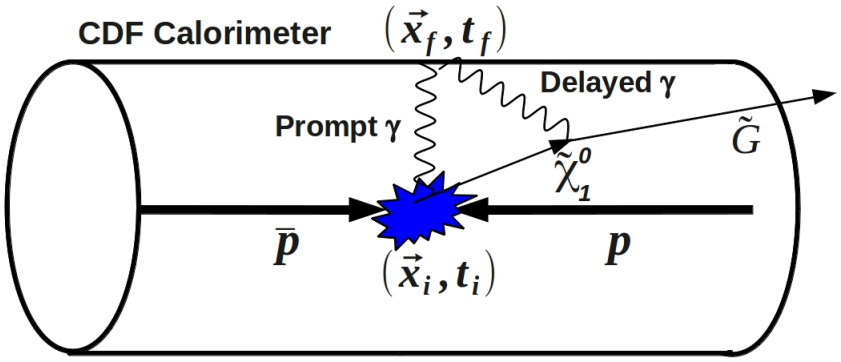

Fig. 1.11. A schematic of production of long-lived $\tilde{\chi}_1^0$ at the Tevatron decaying to a Gravitino ($\tilde{G}$) and a photon (γ) inside the CDF detector with the photon arriving with a delayed time.

For a promptly produced photon, with perfect measurements, $t_{corr} = 0$ ns. Since our detector is not in fact perfect this measurement has an intrinsic resolution and is thus represented by a Gaussian centered at $t_{corr} = 0$ as shown in Figure 1.12 (LHS). We refer to this distribution as the "right vertex" corrected time because it represents the timing distribution when we have correctly identified the origin of the collision. Photons from the decay of a long-lived $\tilde{\chi}_1^0$ would have $t_{corr} > 0$ and thus arrive at a time that is "delayed" relative to expectations from the Standard Model (SM) as shown in Figure 1.12 (RHS). The t_{corr} variable allows for good separation between nanosecond-lifetime $\tilde{\chi}_1^0$'s and promptly produced SM photons [42] since timing res-

olution is known to be ∼0.65 ns. This will be described in more detail in Section 2.2.3.

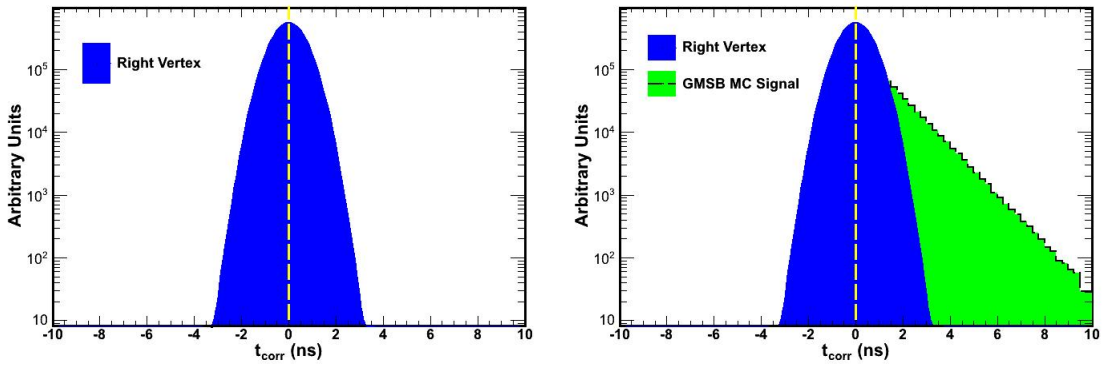

Fig. 1.12. Monte Carlo example of the corrected time variable, t_{corr}, for both promptly produced photons (LHS) as well as photons from a simulated long-lived $\tilde{\chi}_1^0$ (RHS).

Unfortunately, there are other sources of events with large t_{corr} events which make our search more complicated. Specifically, the presence of other collisions occurring in the data taking window that do not have anything to do with the produced photon, as seen in Figure 1.13, can lead to ambiguity in the selection of x_i, t_i. When the incorrect initial interaction point (vertex) is selected in an event we call this a "wrong vertex" event and this results in the "smearing" out of the Gaussian distribution of the t_{corr} variable. The resulting RMS of the t_{corr} distribution becomes ∼2.0 ns where this number comes from timing resolution of the systems involved in measuring the initial and final positions and is discussed further in Section 2.2. With this understanding of right and wrong vertices, we can see that when we select a single vertex for use in an event we will have some chance of having correctly assigned the t_0 and x_0 and some chance of having selected incorrectly. Thus the resulting corrected timing distribution will be the combination of the right and wrong vertex Gaussians as shown on Figure 1.14 where we include what signal from $\tilde{\chi}_1^0 \to \gamma\tilde{G}$ would look like as well.

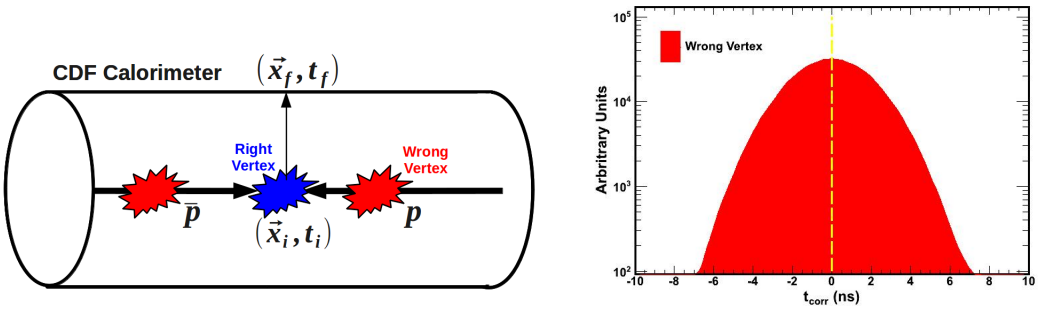

Fig. 1.13. (LHS) Schematic showing how selecting a incorrect vertex (i.e. Wrong Vertex) can cause an errant calculation of the time-of-flight ($\frac{|\vec{x_f}-\vec{x_i}|}{c}$) thus leading to a t_{corr} described by a (RHS) Gaussian with an RMS $\approx$ 2 ns for Wrong Vertices.

Secondly, photon candidates that have nothing to do with the collision and originating from sources external to the detector, typically from 'cosmic rays', present another source of large t_{corr} events. These events are discussed in more detail in Section 4.2. For now it is sufficient to remark that these events have nothing to do with the collision and effectively show up randomly in time and thus present a 'flat' background signature in the t_{corr} distribution, as shown in Figure 1.14. A signal region is readily seen between about 2 ns and 7 ns. Other regions are dominated by right vertex, wrong vertex, or cosmic rays. Each of which can potentially be measured as a background using data.

In the next section we present an overview of a preliminary search, but using simple background estimation technique and no rejection against subtle, yet insidious, backgrounds with large times.

1.5 2008 Preliminary Result

In early 2008 a preliminary search looking for a single photon (identified using criteria described in Section 2.4) plus missing transverse energy (defined in Section 2.4) and little other activity in the detector was performed. In this previous analysis

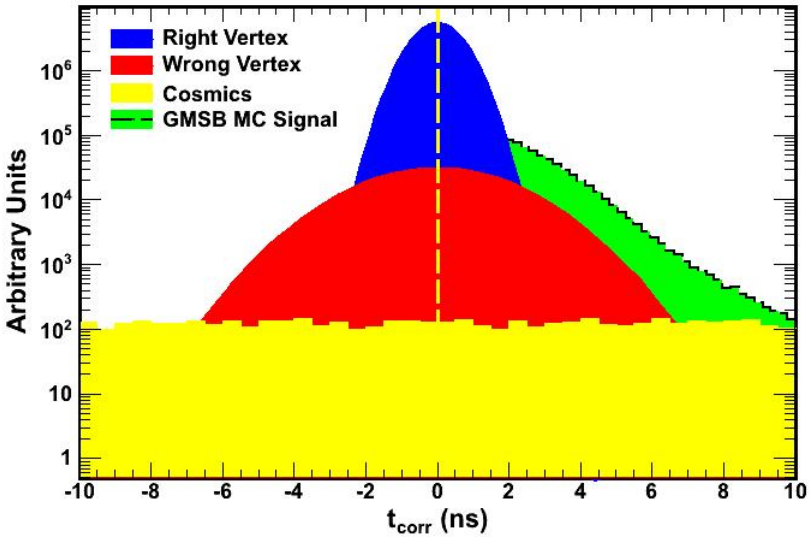

Fig. 1.14. A toy simulation of t_{corr} including GMSB signal events along with a set of collision events. Here the right vertex (blue), wrong vertex (red), and cosmic ray (yellow) distributions are shown. Note, a full description of the cosmic ray background will be given in Section 4.2.

a search for new phenomena know as Large Extra Dimension [52] and was published in reference [53]. This search differed from the exclusive $\gamma_{delayed}$+$\not\!\!E_T$ final state in that the arrival time of the photon was not considered as a way to discriminate between SM and new phenomenon.

Following the publication of this result, even though this search was not optimized for a search for GMSB, the corrected time distribution for the sample of events was examined using the simple prescription described in [42]. This search was shown to be sensitive to the phenomenological regions where 120 GeV/c^2 $< m_{h^0} <$ 160 GeV/c^2, 30 GeV/c^2 $< m_{\tilde{\chi}_1^0} <$ 80 GeV/c^2, and 1 ns $< \tau_{\tilde{\chi}_1^0} <$ 20 ns [43]. The background estimation method used in that preliminary result employed methods used in earler CDF searchs for delayed photons [39]. In particlar, the background estimation method assumed the symmetry in the t_{corr} distribution shown in Figure 1.14 for both the right and wrong vertex distributions. By exploiting the seemingly benign fact that only GMSB

MC signal events were asymmetrically distributed about t_{corr}= 0 ns it seemed very straightforward to predict the number of events expected between 2 ns and 7 ns (signal region) by using the number of events from -7 ns to -2 ns. The results of this prelimnary search are shown in Figure 1.15.

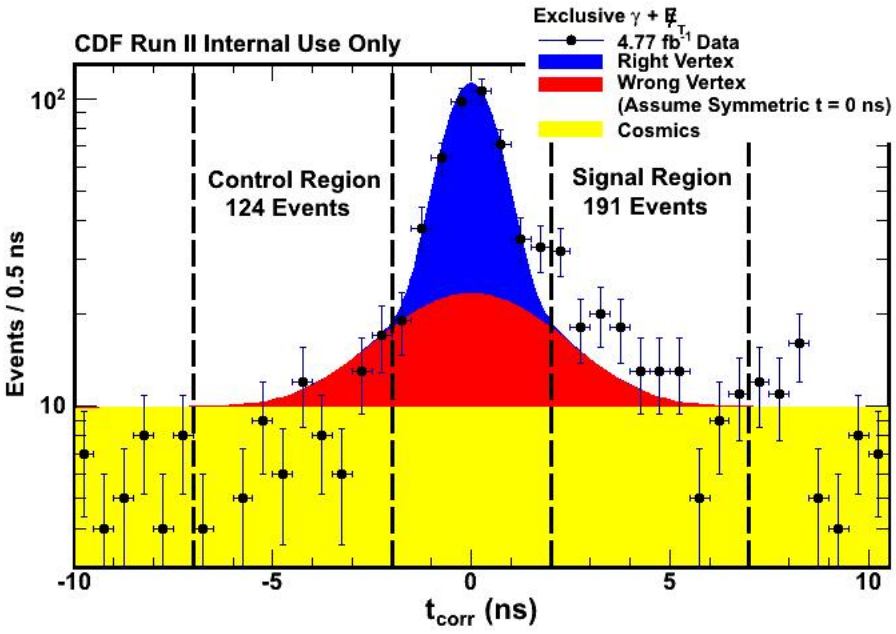

Fig. 1.15. The result of a preliminary search for delayed photons performed in 2008 in the exclusive $\gamma+$ $\not\!\!E_T$ final state showing an excess of events in the region 2 ns$< t_{corr} <$ 7 ns.

What can be seen in the corrected time distribution is a clear excess of events in the region 2 ns$< t_{corr} <$7 ns. There are 191 events are observed in the signal region with a background prediction of only 124 events. This excess is predicated on the assumption that the number of events in the control region (-7 ns to -2 ns) accurately predicts the number of events expected in the signal region from SM sources. Clearly, this is a very interesting result and demands a follow up as well as cross-checks to the underlying assumptions of the analysis.

In many ways, this thesis is the follow up to this reported excess. As discussed before it is possible that this result hints at the discovery of SUSY and possibly even

the Higgs boson. However, extraordinary claims require extraordinary evidence. This thesis is the discussion of the process and what we have learned. In particular, we have done a thorough and systematic search for other sources of events which might produce large time photons in exclusive γ+$\not\!\!E_T$ final state, as well as checked the validity of the background assumptions. In the next section we will lay out the outline for this search as we follow up on the intriguing excess observed and describe the new methods we developed for predicting the number of events from SM sources in the signal region.

1.6 Outline of the Search

This analysis is constructed to follow up on an intriguing excess that was observed in the exclusive $\gamma_{delayed}$+ $\not\!\!E_T$ final state. We focus on doing a search in as model-independent a method as possible. For this reason, we do not focus on GMSB of Higgs specifically, rather we focus on the model of the production of a heavy neutral object that decays, after a few nanoseconds, to a photon plus something that leaves the detector without depositing any energy. While this signature is embodied in $h^0 \rightarrow \tilde{\chi}_1^0\tilde{\chi}_1^0 \rightarrow \gamma\tilde{G}\gamma\tilde{G}$, we use nothing about this decay except that the γ+$\not\!\!E_T$ final state should not be accompanied by any other high energy final state particle.

That being said, this interpretation is amenable to GMSB SUSY scenarios where the $\tilde{\chi}_1^0$ has long enough lifetime to produce a delayed photon and assume that only $\tilde{\chi}_1^0$ pairs are produced in the final state thus making the most sensitive channel the exclusive $\gamma_{delayed}$+ $\not\!\!E_T$ [37]. Due to the length requirements (of the time spent as a Ph.D. student, not dissertation page length), we have focused on a full follow-up of the preliminary result rather than the interpretation of any final result in terms of a new physics prediction.

Our analysis strategy is to study a large number of high energy proton antiproton collisions and to select interactions where the collisions produced a single photon plus missing transverse energy and little other activity in the detector. We next

examine the corrected time distribution of those photons in order to look for evidence that the photons' source is non-SM in origin. The dominant backgrounds for the exclusive $\gamma_{delayed}+ \not\!\!E_T$ final state comes from cosmic rays that interact with the detector producing a fake photon signal in coincidence with a collision as well as wrong vertex events where we incorrectly assign the initial time and time of flight for the photon found in the detector.

One of the most important facts uncovered during the data analysis is that the wrong vertex timing distribution is not symmetric about $t_{corr} = 0$ ns. This makes the analysis far more complicated because this leads to the necessity to develop a new method for estimating the mean of the wrong vertex of our final sample of exclusive $\gamma_{delayed}+ \not\!\!E_T$ events. A significant portion of this analysis is dedicated to understanding the causes of bias in WV events, and with that understanding now fully in hand it is not hard to show create biased samples. For example, the top part of Figure 1.16 shows the corrected timing distribution for one particular SM background ($W \rightarrow e\nu$) using the assumption of a symmetric background timing distribution and the identical selection criteria as the 2008 preliminary result. Clearly this assumption does not accurately model the data, and would lead to the erroneous conclusion that the SM backgrounds do not necessarily have the same number of events in the control region as the signal region. The bottom of Figure 1.16 shows the timing distribution if we release the assumption that the mean of the wrong vertex must be 0.0 ns, but keep the Gaussian description of the data and allow allow the mean to find a value that best matches the data. What we can see here is the double Gaussian assumption of the corrected time distribution does accurately model the SM background with a wrong vertex mean of 0.45 ns.

The observed fact that the mean of the wrong vertex distribution can vary significantly complicates the analysis. We need new ways of predicting the number of events from SM sources in the signal region. Allowing the wrong vertex mean to vary

removes the most straightforward way to predict how many events from SM sources we can expect in the signal region.

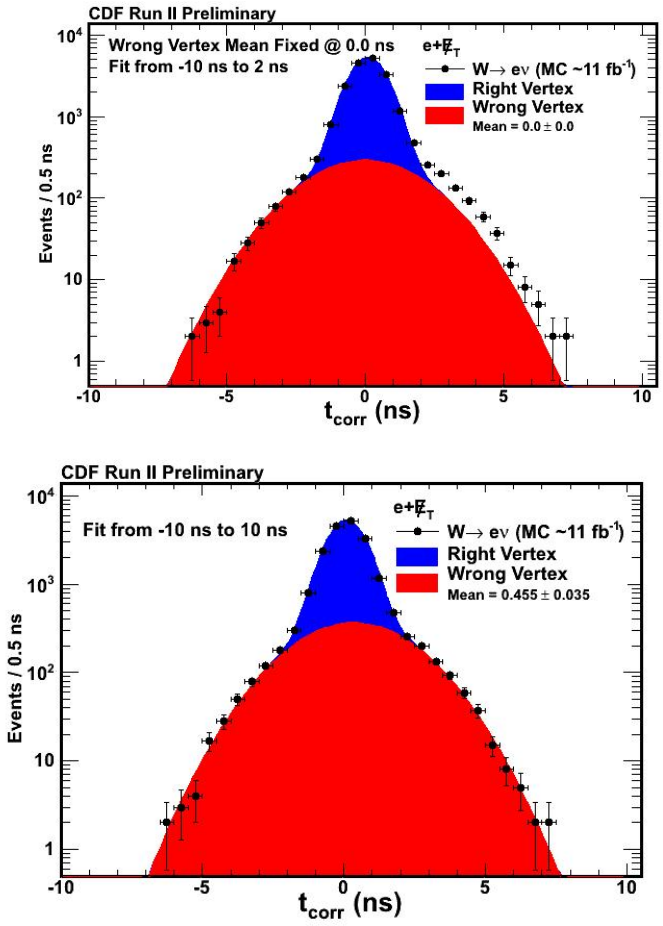

Fig. 1.16. Examining one potential background to the exclusive $\gamma + \not\!\!E_T$ final state shows that the assumption the backgrounds are symmetric about $t_{corr} = 0$ is not accurate. Thus, the assumption that the number of events from standard model sources in the region -7 ns $< t_{corr} <$ -2 ns is not equal to the number of events from standard model sources in the region 2 ns $< t_{corr} <$ 7 ns.

The subject of this thesis revolves around two important and related tasks. The first of these tasks is to understand and mitigate the contributing factors that cause SM backgrounds to give large times. As we will see, there are effects that both

produce large mean shifts as well as effects that can cause the wrong vertex timing distribution to be asymmetric around zero. We will describe the methods to mitigate these factors and leave our data with only sources which are symmetric and have small mean values. The second task then being to develop a method to predict the number of events in the signal region from SM sources now that the simple background method doesn't work.

New features to this analysis since the preliminary result in 2008 are as follow:

1. **Robust Timing Calibrations**: A new and more robust set of timing calibration procedure has been developed that does not suffer from the wrong assumptions of previous methods. Namely, using a selection of $W \to e\nu$ events selected from data in order to ensure that all the objects used in the search have well understood and calibrated timing distributions. This procedure is described in detail in Chapter 3.

2. **Additional Cosmic Ray Rejection**: Two new rejection parameters are implemented in order to help reject the dominant background from cosmic rays that interact with the detector producing a fake photon signal in coincidence with a collision. This is described in Chapter 4.

3. **Identification and Minimization of Pathological Event Reconstruction**: A systematic set of studies have been done to identify and minimize many pathological reconstruction problems that lead to a positively biased event times. As a result a suite of new rejection methods have been implemented. These studies and rejection methods are detailed in Chapter 5.

4. **New $e \to \gamma_{fake}$ Rejection**: The source with the largest wrong vertex timing bias comes from events where an electron fakes a photon due to interactions of the electron in the detector. This particularly insidious background required the innovation of a new variable in order to reject as many of these events

without rejecting real photons coming from collisions. This rejection variable is detailed in Chapter 4.

5. **New Data Driven Background Estimation**: Finally, a new background estimation method is developed and presented which shows that it is possible to derive the underlying wrong vertex mean and thus make a prediction of the number of events we expect in the signal region from Standard Model sources. The details and results of this background estimation method is shown in Chapter 6.

6. **Addition of More Data:** Along with all the improvements to this analysis, we add 25% more data the what was used in the 2008 result. The final result is discussed in Chapter 7.

With all these new tools will will have a robust and reliable search that will be able to answer many of the questions about the search results from 2008.

1.7 Outline of the Dissertation

In Chapter 2 we present the experimental tools used in this analysis, including the Fermilab Tevatron collider as well as the Collider Detection at Fermilab (CDF) detector which surrounds the collision point and records the activities of the resulting interactions. In particular we describe the relevant subsystems used at CDF in the timing measurement. Chapter 2 also describes the various object identification that is performed from the information read out from the CDF detector as well as laying out the various useful data samples used in this analysis. In Chapter 3 the new calibration procedure is detailed in order to ensure that we have accurate and reliable timing information associated with photons in this analysis. Chapter 4 details non-collision backgrounds and new selection requriements used to minimize their presence in our final sample of events. In Chapter 5 we turn our attention to

the various Standard Model backgrounds and the pathological event reconstruction which results in the corrected timing distribution being asymmetric about $t_{corr} = 0$ as well as the methods we use to mitigate many of these effects. Chapter 6 focuses on the development and validation of a new data driven background estimation of the underlying timing distribution from Standard Model sources. Finally, Chapter 7 presents the results of the search in the exclusive $\gamma_{delayed}+\not{E}_T$ final state utilizing the data driven background estimation method. Chapter 8 ultimately summarizes these results and provides an interpretation to the results as well as proposing possible extensions to the search which could be performed in the future.

2. EXPERIMENTAL TOOLS

This chapter describes the experimental apparatus used for this analysis. This includes the Fermilab Accelerator complex, a description of the detector that surrounds the collision point and many of the algorithms used to identify our γ+$\not\!\!E_T$ events. We begin with a description of the Fermilab accelerator complex, most importantly the Tevatron circular particle accelerator [54]. The Tevatron collided proton-antiproton beams at energies which were, until 2008, the most energetic collisions in the world and continued colliding till September 2011. Surrounding one of the collision points is the experiment known as Collider Detector at Fermilab (here after referred to as CDF) which recorded the energy and trajectory as well as identified the various particles produced by the proton-antiproton collisions. The various subsystems most relevant to this analysis will be described in greater detail along with details about the information they report. The readouts of these various subsystems allow us to filter out, in real time, photon events from the millions of collisions every second that are being produced.

From this subset of events we then search for the evidence of new physics by selecting candidate collisions ("events") with the signature of γ+$\not\!\!E_T$. We then use information about the arrival time of the photon and the collision time to see if any arrive delayed relative to expectations and thus possess a signature of coming from new physics. With this in mind, we turn our discussion to the Tevatron, CDF, and the process by which collisions are read out of the detector in general and reconstructed in particular.

2.1 The Fermilab Tevatron

We begin by summarizing Fermilab's accelerator chain that produce a beam of protons (p) and antiprotons ($\bar{p}$) suitable for collisions in the Tevatron. The accelerator chain is described in great detail in Reference [54,55], but we give a brief overview

here. Fermilab's accelerator chain is shown schematically and in aerial view in Figure 2.1. The particles begin as hydrogen gas that is ionized to make hydrogen ions in a Cockcroft-Walton accelerator [54]. The ions are then passed to the linear accelerator (Linac) that accelerates the ions to 400 MeV and then passes them through a carbon foil in order to strip off remaining electrons before passing these protons to the next part of the accelerator known as the "booster". The booster consists of 18 Radio Frequency (RF) ferrite-tuned resonators, commonly referred to as "cavities" which accelerates the protons to 8 GeV as well as brings them closer together, commonly referred to as "bunching". During the bunching process the particles are captured into 37.7 MHz "buckets" before being passed to the next part of the accelerator known as the "Main-Injector". The Main-Injector accumulates, accelerates, and stores protons taking them to energies of 150 GeV and combining the previous set of bunches into a single bunch. This process of bunching the protons is then repeated 36 times until a total of 36 bunches of protons have been produced. Taken together this set of 36 bunches is commonly referred to as a "train". These protons can now be passed to the final part of the accelerator chain, namely the Tevatron.

In addition to providing protons to the Tevatron, the Main Injector provides a source of protons to be used in order to produce antiprotons. The antiprotons are created by accelerating the protons in the Main-Injector to 120 GeV and then colliding them into a target of nickel alloy. The byproduct of the collisions with the nickel target is a varied array of particles, from which antiprotons are selected and decelerated (reducing their momentum spread) in a part of the accelerator known as the "debuncher". From the debuncher the antiprotons are then passed to another accelerator system known as the "Accumulator". The Accumulator is located in the same tunnel and, as the name suggests, is where the antiprotons are accumulated and where they undergo stochastic cooling before being passed to another system known as the "Recycler". The Recycler is located in the same tunnel as the Main Injector and uses permanent magnets to store high intensity beams of 8 GeV antiprotons. It

is in the Recycler where "electron cooling" is used to allow a more intense source of antiprotons to be produced. Electron cooling introduces a low emittance electron beam collinear to the antiproton beam and through momentum transfer the antiprotons are "cooled". The antiprotons are then bunched in 36 bunches and accelerated to 150 GeV. When this process is complete, there are 36 bunches of protons and antiprotons ready to be transferred ("injected") into the Tevatron main ring to be used for high energy physics collisions [54, 55].

In the main ring (typically just referred to as The Tevatron), which is a superconducting circular accelerator, the proton-antiproton beams are accelerated from 150 GeV to 980 GeV with $\sim 3 \times 10^{11}$ protons/bunch and $\sim 7 \times 10^{10}$ anti-protons/bunch. The Tevatron consists of 774 superconducting dipole magnets and 240 quadrupole magnets. The former are used to bend the beam around the 3.9 mile circumference ring and the latter are used to focus the beams while electrostatic potentials accelerate the particles.

These beams couter rotate in the Tevatron during data taking and are made to collide at two points along the ring, the CDF and D0 detectors. The focusing parameter, known as β^* ("beta star"), focuses the crossing of the beams to a $\sim$27 cm region in z. The beams remain for several hours during collisions (often referred to as a "store"). The smallest unit of data taking, referred to as a "run", is some interval of uninterrupted time during a store (or stores) where no change in detector setup or data-acquisition has occurred. The beams collide at a center of mass energy of 1.98 TeV every 396 ns with a typical RMS in z of $\sim$28 cm and an RMS in t of $\sim$1.28 ns. A basic summary of the various Tevatron parameters that existed during the data taking for this thesis is presented in Table 2.1. With a good understanding of the collisions, we move to the detector that surrounds the collision point, and eventually on to the algorithms that help us identify γ+$\not\!\!E_T$ events.

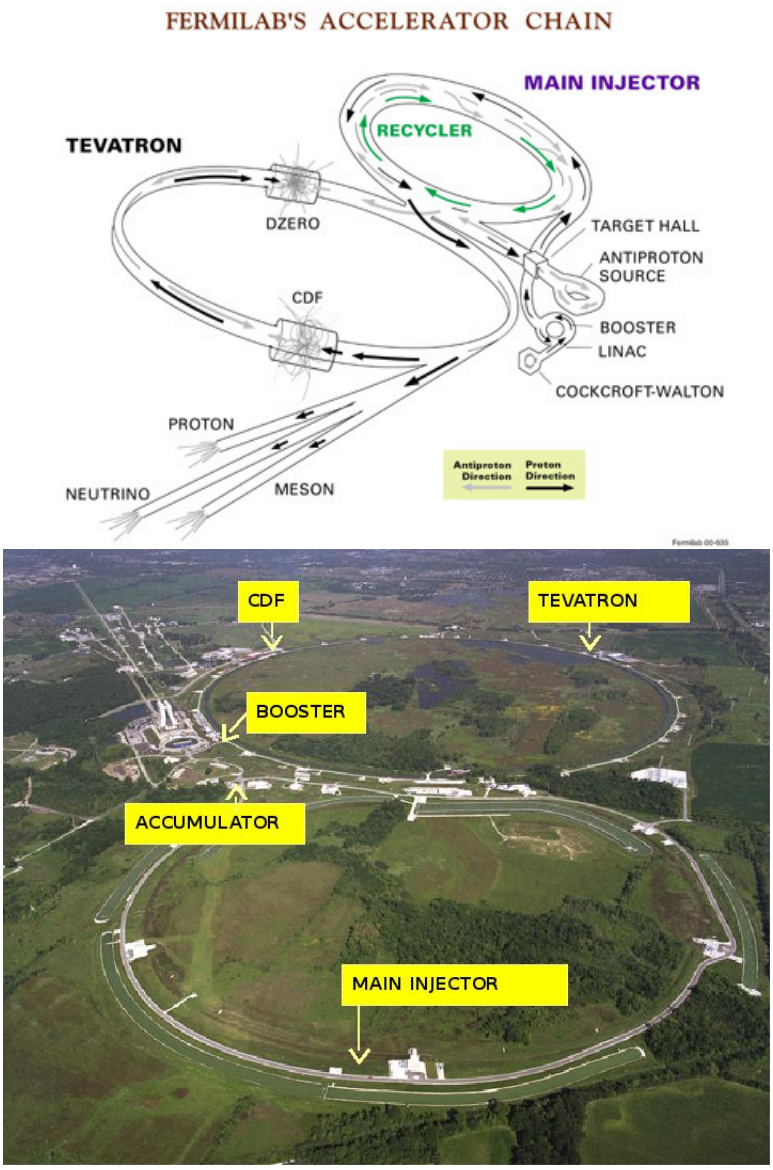

Fig. 2.1. Overview of the Tevatron accelerator complex.

2.2 The Collider Detection at Fermilab

The Collider Detection at Fermilab (CDF) detector is described in detail in Reference [56], but we summarize here portions of the detector most relevant to this analysis. CDF is a cylindrical multi-purpose detector that surrounds the collision

Parameter (Units)	Value
Energy per Beam (GeV)	980
Number of Bunches	36
Bunch Spacing (ns)	396
Protons per Bunch (N_p)	$\sim 3\times10^{11}$
Antiprotons per Bunch ($N_{\bar{p}}$)	$\sim 7\times10^{10}$
Collision Point RMS in z (cm)	28
Collision Point RMS in t (ns)	1.28

Table 2.1
Summary of the Tevatron accelerator parameters during "Run II" data taking.

point and is designed to study $p\bar{p}$ collisions at the Tevatron. The design of the detector, as seen in Figure 2.2, is symmetric in cylindrical coordinates and identify and measure the 4-momentum of a particles produced in $p\bar{p}$ collisions [56].

CDF makes use of a cylindrical coordinate system where the positive z axis is defined along the direction of the incoming proton beam, ϕ is the azimuthal angle, and θ is the polar angle defined with respect to the x axis. Additionally, a useful angular variable (η) known as pseudorapidity that is used throughout the remainder of the thesis is defined as

$$\eta = -ln(tan(\frac{\theta}{2})). \tag{2.1}$$

Within the central part of the CDF detector a 1.4 T magnetic field along the z direction generated by a superconducting solenoid 1.5 meters in radius and 4.8 meters long. Within this magnetic field the various tracking detectors are located to measure the trajectory of the charged particles produced during collisions. The magnetic field allows for a measurment of the sign of the charged particles, as well as their momentum as they traverse the tracking chamber. Surrounding the tracking chambers in concentric sub-detector systems are the various energy measuring

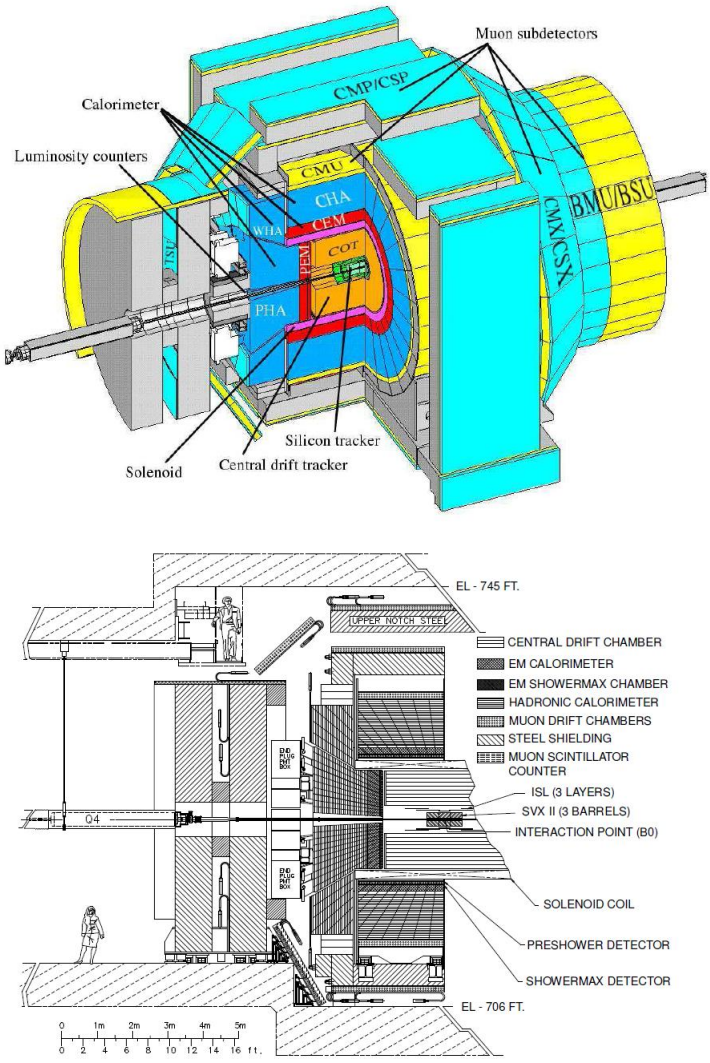

Fig. 2.2. Isometric (top) view and elevation (bottom) view of the CDF detector.

detectors (calorimeters) and chambers used to measure and identify muons are located outside of the solenoid and provide further particle identification and energy measurements.

The combinations of the various detector components consists of concentric subdetectors that allow for the identification of particles such as photons, electrons, muons, taus as well as measure the energy and momentum of the particles. The

various identification criteria used in this analysis are described later in Section 2.4. In the following sections we characterize in greater detail the subdetectors having the most impact on this analysis. We begin with the inner most tracking detectors and work our way out to the calorimeters and eventually the muon chambers. After this description we will discuss how each is used as part of the reconstruction of a collision and identification of our final state particles.

2.2.1 The Tracking Systems

The part of the CDF detector closest to the beam line is made up of a set of tracking detectors used to determine the momentum and charge of charged particles passing through the various subsystems by using their measured paths and curvatures in the magnetic field. Groupings of the particles' trajectories are projected back to the beam line and allow reconstruction of both the position and time of the interaction (referred to as the event vertex).

The tracking system includes two detectors: an inner Silicon VerteX detector (SVX) and a Central Outer Tracker (COT) which surrounds it. The SVX detector is described in greater detail in Reference [57], but we summarize the important features here. The SVX consists of a silicon microstrip system used for precision position measurements as well as giving additional 3D tracking reconstruction capability. The SVX spans radially from the beam pipe from 2.5 cm$< r <$10.6 cm and covers a distance in the z-direction of 175 cm. The SVX provides pattern matching with the outer tracking system as well as standalone tracking for charged particles independent of the COT. While the SVX provides a higher spatial resolution on individual tracks (which is also used for vertexing), there is no timing information from the SVX system and thus it does not improve our t_0 measurement.

The COT surrounds the SVX system and is a cylindrical open-cell drift chamber that spans a radius of 44 cm $< r <$ 132 cm and covers a distace in z of 310 cm extending to $|\eta| = 1.0$. The COT chamber is described in Reference [56], but we

highlight the important features here. The COT is filled with a 50:50 mix of argon and ethane gas along with a small admixture of isopropyl alcohol and oxygen. This provides the COT with a maximum drift time of 100 ns (small compared to the 396 ns bunch spacing in the Tevatron). As charged particles pass through the chamber they ionize the gas leaving a trail of electrons which are attracted to the sensor wires by the electric field generated by the potential wires and cathodes.

Within the COT a the wires are grouped into sections of into 96 layers of sense wires which are grouped into eight "superlayers" of 12 wires each. This allows for a high quality measurement of the kinematics of the track in the magnetic field, it's charge, as well as its initial position and time at the beam line.As shown in Figure 2.3 the superlayers alternate between axial wires (running parallel to the beam line) and stereo wires that are tilted by 3 degrees with respect to the beam line. This configuration allows particle trajectories to be reconstructed in three dimensions and a hit resolution of 140 μm. Simultaneously, the COT provides a track momentum resolution of $\sigma(p_T)/p_T^2 \approx 0.3\%$ $(\mathrm{GeV/c})^{-1}$ and a track z position at the beam line of $\sim$0.22 cm. The time information associated with each hit allows for a timing measurement of the track along the trajectory and can also be used to derive the initial time (t_0) that the particle was produced. The COT is found to have a t_0 resolution for well measured tracks to be $\sim$0.27 ns [56].

As will be discussed further in Section 2.4, the z and t information obtained from the combined SVX/COT is used to create verticies that are produced along the beam line indicating where the primary collision of the proton and antiproton was likely to have occurred.

2.2.2 Electromagnetic Calorimeter

The calorimeter system at CDF is used to measure the energy and position of particles as well as provide particle identification and a full measurement of the missing transverse energy. The system itself is is described in detail in Reference [56],

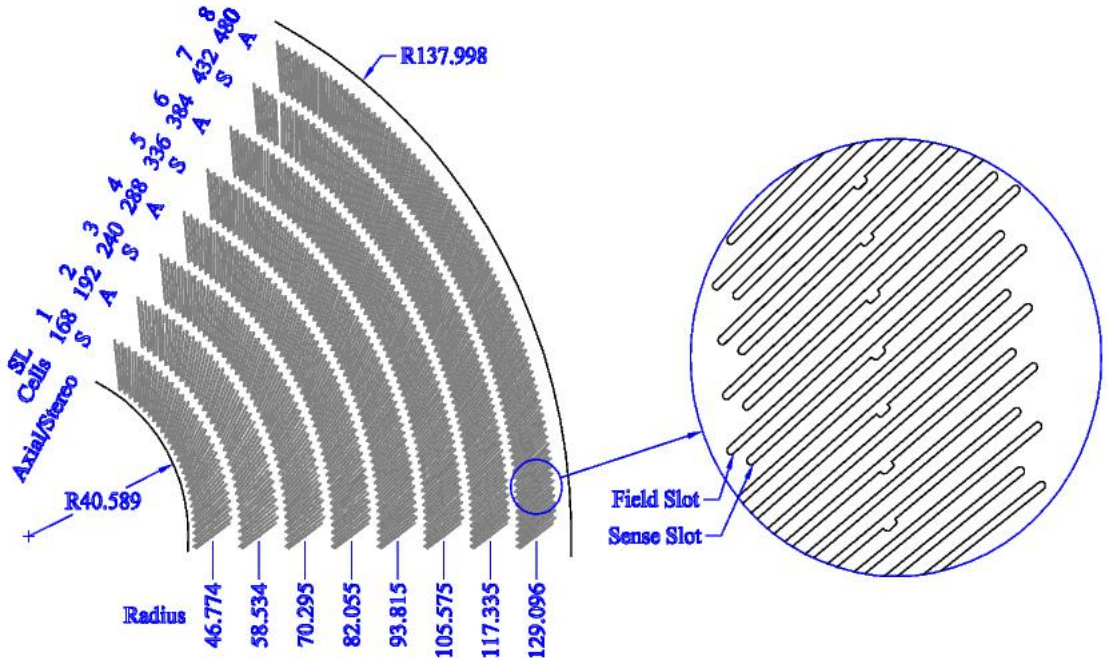

Fig. 2.3. A 1/6 section of the Central Outer Tracker (COT) end plate. The COT has eight conentric "superlayers" seperated in ϕ into "supercells", with each containing 12 sense wires between field sheets. For each "superlayer" the total number of "supercells" , the wire orientation (axial or stereo), as well as the average radius is given in centimeters.

and we provide an overview here. The calorimeters are housed just outside the solenoid and is used to measure the energy deposited by particles out to $|\eta| < 3.64$. Having accurate measurement of the energy deposited in the various calorimetry systems is important in order to distinguish photons from other particles (as will be discussed in Section 2.4) as well as identify any energy imbalance due to particles escaping the detector. This becomes of particular significance when deciding which events to record from the detector based on energy measurements such as is done in this analysis.

The calorimeter is constructed using a tower structure projected to the most probable collision point at the center of the detector. Towers cover 15 degrees in ϕ and $\sim$0.10 in η, where all towers at the same ϕ on one side of the detector are physically grouped into what is referred to as a "wedge". Within each calorimeter tower there are two components, known as the electromagnetic (EM) and the hadronic (HAD) components. During normal beam operations both the electromagnetic and hadronic calorimeter systems integrate the energy deposited in each tower of 132 ns time intervals that contain the collision time. Closest to the beam line is the EM and the majority of any interaction of an electromagnetic interaction (like from photon or electron) will deposit the overwhelming majority of their energy in this compartment. Radially just outside the EM is the hadronic calorimeter, which has the same tower/wedge geometry as the EM but using instead iron sampling in order to measure the energy and shower of hadronic particles. Using both the EM and Had we can identify and measure the energy of jets with an energy resolution of $\sigma \frac{E}{=}$ $0.1E_T$ +1.0 GeV. Considering the entire calorimeter a full measurement of the $\not\!\!E_T$ can be typically measured to a few GeV.

Since we want high quality measurements and identification of the photons in this analysis, this analysis restricts itself to only considering photons that come from the "central" ($|\eta| < 1.0$) region and thus only use the Central Electromagnetic calorimeter (CEM) shown in Figure 2.4. Restricting ourselves to photons from the "central" region allows us to take advantage of the tracking having full coverage of the calorimeter and thus is the best for photon identification.

A second advantage of using the central region is that it is well instrumented inside the calorimeter itself. The CEM uses 23 lead and polystyrene scintillator layers alternating in radial direction with $\sim$5 mm thickness and covering 21 radiation lengths (X_0) that fully contain the energy cascade showers of most electromagnetic particles such as photons and electrons. Light deposited in the scintillators strips is directed out in wavelength shifting fibers to two phototubes located on opposite sides

of each tower and provide an energy measurement with resoltuion $\frac{\sigma(E)}{E} = 0.1E_T +$ 1.0 GeV.

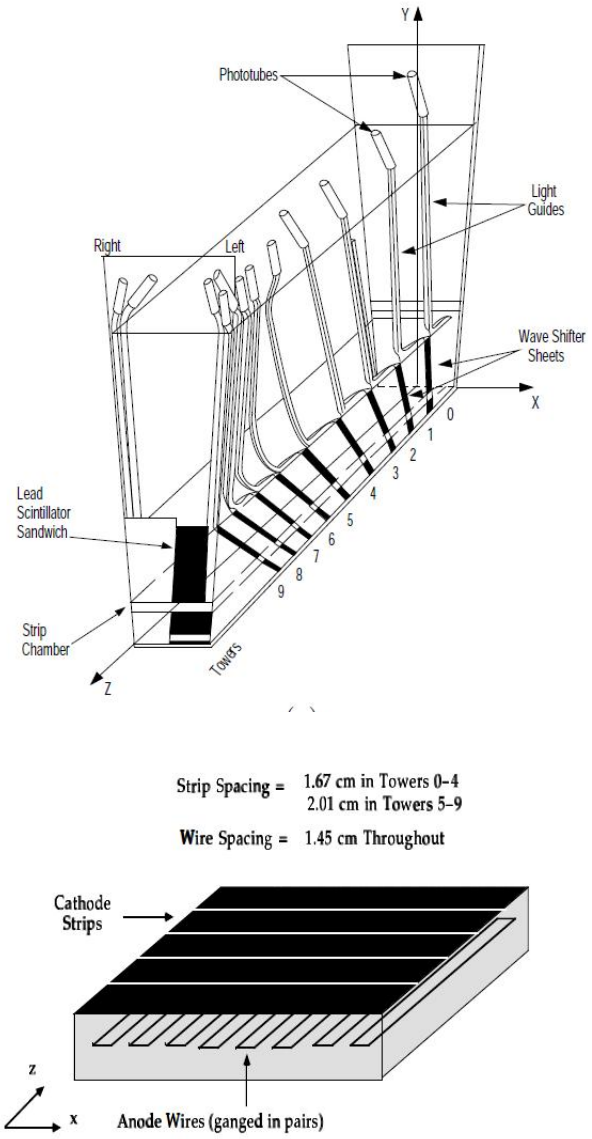

Fig. 2.4. (Top) A schematic drawing of the Central ElectroMagnetic calorimeter (CEM) including the (Bottom) Central Electromagnetic Shower (CES) sub-detector showing the strips and wires.

A proportional strip and wire chamber, known as the Central Electron Strips (CES), is located at a depth of $\sim 6X_0$ corresponding to the "shower maximum" of electrons and photons [56]. The CES consists of 256 cathode strips running in the ϕ direction and measure the position and profile in z as well as 128 anode wires running in the z direction that measure the position and profile in the ϕ with a resolution of $\sim$2 cm.

2.2.3 EMTiming System

One system that plays a central role in this analysis is the ElectroMagnetic calorimeter Timing system (EMTiming system) as it allows the calorimeter system to record the time of arrival of the particles as well as the energy deposited for all high energy particles with $|\eta| < 2.1$. This system is described in more detail in Reference [58] and we provide a summary of this system here. The timing information created by the EMTiming system allows the ability to separate potential new physics signal events coming from "delayed" photons from promptly produced photons. In particular it provides a measurement of t_f from Equation 1.7. Additionally, the system allows us to estimate and reject energy deposits that may have come from cosmic rays or beam related effects.

Within the CEM Figure 2.5 shows a schematic of the measurement hardware showing how the EMTiming system measures the arrival time using the signal from the energy in the electromagnetic shower. The EMTiming system is attached to the outputs of the photomultiplier tubes (PMTs) which collect the scintillated light from the interaction in the calorimeter on opposite sides of each tower in the CEM and convert this energy into an analog signal. This signal is then sent to a transition board and an Amplifier-Shaper-Discriminator which converts the analog signal into a digital one. This digital signal is the sent to time-to-digital converters (TDCs) for a time measurement that is then read out by the CDF data acquisition system.

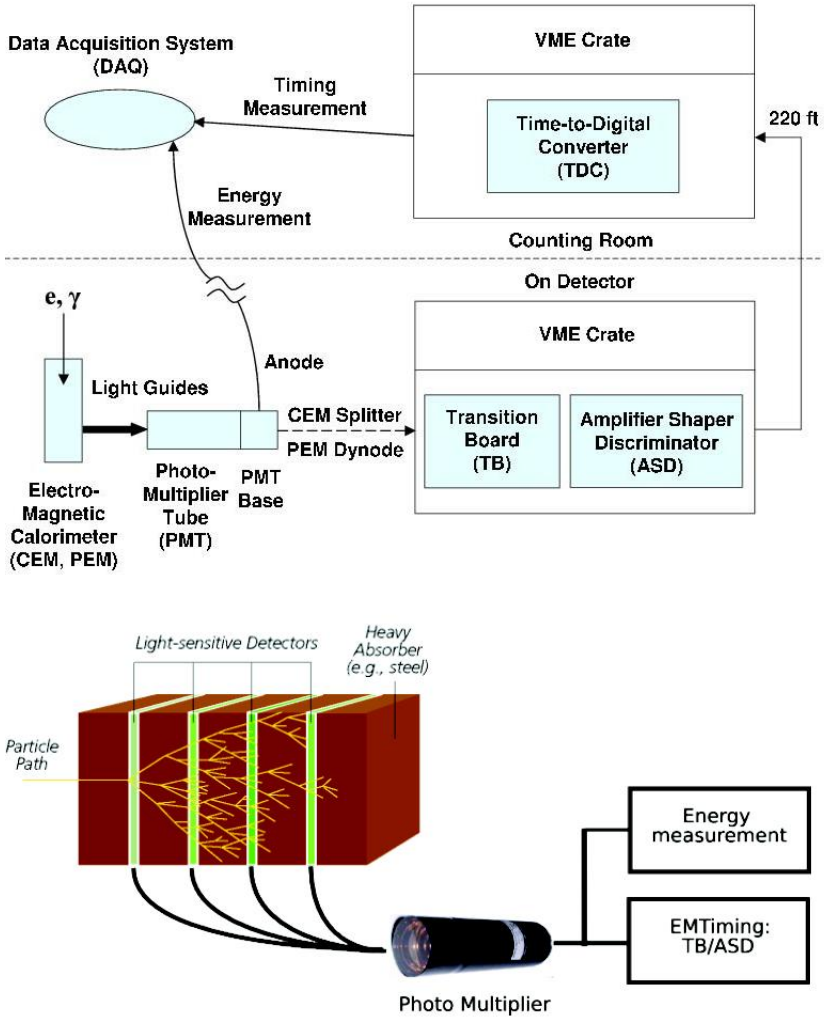

Fig. 2.5. (Top) A schematic view of the EMTiming system. (Bottom) A diagram demonstrating how the energy and timing measurement of a particle that showers in the calorimeter is made using the light obtained from the Photo Multiplier Tube.

The EMTiming system is observed to be 100% efficient for energies above 3 GeV in the CEM with a system resolution of ∼0.5 ns [58]. The calibration and overall uniform performance of the EMTiming system is discussed in greater length in Section 3.1.1 but is worth noting that the system has performed with nearly 100%

efficiency and negligible downtime since its installation and commissioning in the fall of 2004. This translates to ∼6600 hours of of live time or over 13 million PMT-hours of successful running.

2.3 The Data Acquisition and Trigger Systems

Collisions occur at the center of the CDF detector every 396 ns making the selection and storage of useful physics events while rejecting uninteresting collisions a formidable task . The Data AcQuisition system (DAQ), shown in Figure 2.6, and described in greater detail in Reference [59], at CDF performes this task with the necessary rejection rate of approximately 10^6:1 as only about 100 events per second could be written to record at the average logging rate of ∼23 MB/s.

To this end the CDF DAQ was built into a three-level trigger system creatively referred to as Level 1 (L1), Level 2 (L2), and Level 3 (L3). The beginning two levels consist of custom built hardware which allowes a gradual reduction of the event rate to $<$ 50 kHz at L1 and to 300 Hz at L2. Level 1 makes decisions based on simple physics quantities using a subset of information from the detector. Level 2 uses a combination of hardware and software to perform a limited event reconstruction and chooses whether or not to accept events based on calorimeter algorithms, shower information, and combined tracking information. After L2 accepts an event, the data from all the various subdetectors is combined into a single event by the event builder [60] and passed to L3. Level 3 consists of a farm of computers that filter the data coming from the event builder to 100 events per second and then sends that data to be stored. The DAQ system is designed such that there is no or minimal loss of data (no dead time).

The events selected for this analysis are selected by a set of 3-level trigger requirements summarized in Table 2.2, and referred to as the "WNOTRACK" trigger (pronounced W no track). This selection requires an EM cluster (which can be seen as a very loose selection criteria for a photon candidate) and missing trans-

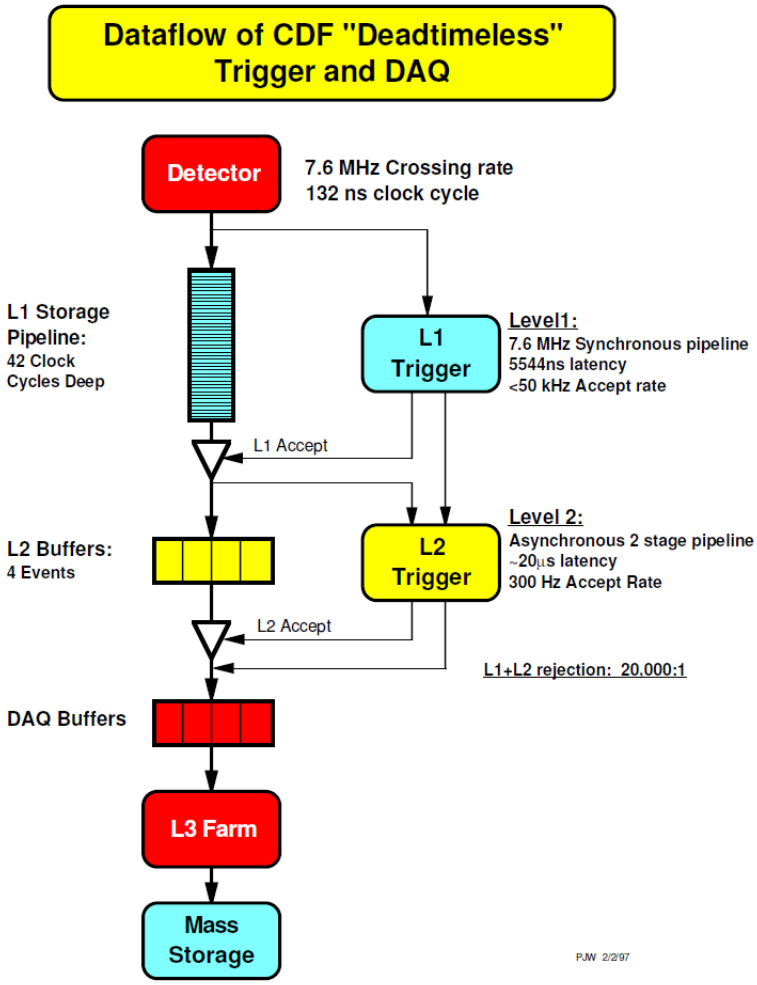

Fig. 2.6. (Top) Data flow diagram of the deadtimeless trigger and Data Aquisition system at CDF [59].

verse energy ($\not\!\!E_T$) to be present in the event. As the name suggests, this trigger was originally used as a backup trigger for selecting $W \to e\nu$ events without relying on tracking measurements. We use this trigger in this analysis primarily because it is one of the only triggers available for a photon selection without an isolation or CES-χ^2 requirements which has been found to be inefficient for photons from long-lived particles [61].

Object Type	**Trigger**		
	Level 1	**Level 2**	**Level 3**
Electromagnetic Cluster	≥ 1 Central EM Cluster $E_T > 8$ GeV $\frac{E_{Had}}{E_{EM}} < 0.125$	$\lvert\eta\rvert < 1.1$ $E_T > 20$ GeV $E_T^{SeedTower} > 8$ GeV	≥ 1 EM Cluster $E_T > 25$ GeV $\frac{E_{Had}}{E_{EM}} < 0.125$
Missing Energy	$\not\!\!E_T > 15$ GeV $\Sigma E_T > 1$ GeV		$\not\!\!E_T > 25$ GeV

Table 2.2
Online Event Selection for the WNOTRACK Trigger.

Events passing the full set of WNOTRACK requirements are then written to permanent storage to be analyzed in greater detail later. This trigger has been found to be nearly 100% efficient [61] for electrons and photons. In addition to this primary trigger, we also allow the logical *.OR.* of many of the other associated photon triggers which all overlap with the requirements of the WNOTRACK trigger (shown in Table 2.2). We use these additional triggers to help ensure that we come as close as possible to 100% efficiency for selecting potential γ+$\not\!\!E_T$ events. The summary of these other triggers can be found in Table 2.3.

Events constituting the data sample analyzed for this thesis represent data taken from approximately December 2004, when the EMTiming system was fully commissioned, to June 2010. In conjunction with the triggering system, a list of data taking periods for which all the necessary subsystems are functioning properly is established in what is known as a "Good Run List". In the this analysis we use a "Good Photon Run List" [64] which requires that the Shower Max, Central Outer Tracker, Silicon, and Muon subsytems were operational during data taking. Moreover, we apply a unique GoodEMTiming Run List that both disregards runs where the EMTiming system was not functioning properly (this accounts for <0.1 fb^{-1} reduction in luminosity). We furthermore require that all the runs within the good run lists must have an integrated luminosity ≥ 100 nb^{-1} to ensure there are sufficient statistics to

Object Type	Trigger		
	Level 1	**Level 2**	**Level 3**
ZNOTRACK			
Electromagnetic Cluster	≥ 1 Central EM Cluster $E_T > 8$ GeV $\frac{E_{Had}}{E_{EM}} < 0.125$	≥ 2 EM Cluster $\lvert\eta\rvert < 1.1$ Both w/ $E_T > 16$ GeV Both w/ $E_T^{SeedTower} > 8$ GeV	≥ 2 EM Cluster Both w/ $E_T > 16$ GeV $\frac{E_{Had}}{E_{EM}} < 0.125$
SUPERPHOTON70			
Electromagnetic Cluster	≥ 1 Central EM Cluster $E_T > 10$ GeV	$\lvert\eta\rvert < 1.1$ $E_T > 70$ GeV $E_T^{SeedTower} > 8$ GeV	≥ 1 EM Cluster $E_T > 70$ GeV $\frac{E_{Had}}{E_{EM}} < 0.2$
PHOTON25ISO			
Electromagnetic Cluster	≥ 1 Central EM Cluster $E_T > 8$ GeV $\frac{E_{Had}}{E_{EM}} < 0.125$	$\lvert\eta\rvert < 1.1$ $E_T > 21$ GeV $E_T^{SeedTower} > 8$ GeV $E_T^{ISO} < 3$ GeV $\frac{E_{Had}}{E_{EM}} < 0.125$	≥ 1 EM Cluster $E_T > 25$ GeV Iso$^{Total} < 2.0$ $\chi^2 < 20$ $\frac{E_{Had}}{E_{EM}} < 0.055$

Table 2.3
List of additional triggers accepted on the logical *or* of the WNOTRACK trigger.

calibrate over that given run period (again resulting in only a < 0.1 fb^{-1} reduction in luminosity). After these various requirements the data analyzed corresponds to an integrated luminosity of 6.3 ± 0.4 fb^{-1} as shown in Table 2.4.

2.4 Object and Event Reconstruction

Once the events are selected from the DAQ system they are processed "offline" where event reconstruction occurs. Offline processing consists of a series of steps to ensure the events are classified by their identified objects. The goal of this framework is to use various detectors in order to reconstruct high level objects such as tracks,

Period	Run Range	SAM #	≈ Luminosity (pb^{-1})
1-4	190851-203799	bhelbh	460 pb^{-1}
5-10	203819-233111	bhelbi	1020 pb^{-1}
11-13	233133-246231	bhelbj	660 pb^{-1}
14-17	252836-261005	bhelbk	410 pb^{-1}
18-28	261119-289197	bhelbm	3030 pb^{-1}
29-30	289273-293800	bhelap	720 pb^{-1}
Totals	190851 - 293800		6300 pb^{-1}

Table 2.4
Table summarizing High P_T Data Set used in this analysis and luminosity over the various run ranges.

vertices, electrons, muons, clusters of energy (jets). The details of how each of these objects is reconstructed is given in the following sections and in Appendix A. From this data we select a subset of events that contain a γ+$\not\!\!E_T$. This is a sophisticated procedure thus we outline the various event reconstruction (Object Identification) performed on the data taken as well as lay out the selection of various presamples that will constitute the events to be analyzed in the exclusive γ+$\not\!\!E_T$ analysis.

The way objects are identified in the detector will be used in many ways, for example to identify candidate events online, as well as for crude preselection and then later precise final selection. Indeed, many algorithms use other algorithms as their basis for selection. For example, electrons, photons and jet candidates all start by looking for clusters of energy in the calorimeter. Photons and electrons are the subset of those clusters that are mostly in the electromagnetic calorimeter. Of the EM clusters, electrons are identified as EM clusters with a high P_T track associated with it, and photons are selected by virtue of the absense of such a track. Meanwhile "jet" is the catch all for clusters of energy which are neither of these, and can be due to a tau lepton, a poorly identified photon or electron, or radiation from a quark or gluon.

We begin with a general description of clusters of energy found in the calorimeter known as "jets". From this generic definition we will lay out the object-id for tracks, photons, and electrons in the CDF calorimeter and tracking chamber. Next we describe the technique to cluster together tracks at the beam line in order to identify the origin of the collision, known as the event vertex. Finally we describe the definition of Missing Energy by looking for imbalance of energy throughout the event in the CDF calorimeter.

Jets

A "jet", as defined at CDF, is identified as a cluster of energy in the calorimeter. This definition is generic enough to include energy from electrons and photons as well as that of the hadronic decays of τ-leptons in addition to the more typical definition of the hadronization of high energy quarks or gluons coming from the collision.

Jets are first identified by looking for energetic "seed" towers (defined in Appendix A). Additional towers within a radius in $\eta - \phi$ space are then added to the jet and a new jet center is calculated using a weighted average of every tower in the jet. This process is then repeated until the jet no longer changes and overlapping jets are merged if two jets overlap by $> 50\%$. Functionally, this process's primary goal is to determine the energy of the particle that produced the jet. Therefore, a number of standard corrections are applied to correct for calorimeter response, un-insturmented regions of the detector, and fraction of energy that falls outside the search cone. A detailed explanation of the CDF jet calibration is beyond the scope of this thesis and can be found in reference [65]. In Table 2.5 we define the variables used to identify jets in the CDF detector using the standard jet-cone algorithm. The detailed variable definitions used here can be found in Appendix A.

Variable	Cut
Seed Tower	$\geq$ 1.0 GeV
E_T^0	$>$ 1.0 GeV
$\|\eta\|$	$<$ 3.4

Table 2.5
Table for the standard CDF jet identifcation variables.

Tracks

As a charged particle passes through the COT it ionizes the gas in the chamber. As previously described, the trajectory of charged particles through the SVX and COT can are reconstructed as tracks with high quality charge, 4-momentum, and z and t_0 information about when they originated at the beam line. It is this path of the charged particle that we refer to as a track. We will use tracks in three different ways in this analysis:

1) **For photon identification:**

   These tracks distinguish between electrons and photons. We reject any photon candidate if there is a track containing readout coming from both the silicon and COT tracking system with P_T >0.3 GeV/c that points to the electromagnetic cluster in the calorimeter.

2) **For vertex time information:**

   These tracks are later used in the vertexing algorithm when attempting to reconstruct the initial time (t_0) and position (z_0). The variables used to describe these tracks are standardized within CDF and are described in more detail in Appendix A. The requirements used to select track for use in the vertexing are given in Table 2.6.

3) **For our event veto:** In the final event selection, we will reject events that have a high probability of being from backgrounds. For this reason we will reject events with a high momentum track as part of requiring that our γ+$\not\!\!E_T$ events be exclusive. These tracks we consider for vetoing have a less strict definition since we are only looking for evidence that the final state is not exclusive $\gamma_{delayed}$+$\not\!\!E_T$ and are summarized in Table 2.4.

Variable	**Cuts**
P_T	≥ 0.3 GeV
$\|\eta\|$	< 1.6
$COTStereoSeg(5)$	≥ 2
$COTAxialSeg(5)$	≥ 2
$\|Z\|$	≤ 70 cm
$\|d_0\|$	≤ 1.0 cm
T_0 σ	$0.2 < T_0$ $\sigma < 0.8$ ns

Table 2.6

Standard good timing track identification variables. Note, these cuts are used in order to ensure a good timing measurement on the track in addition to a good position measurement. These variables are defined in more detail in Appendix A.

Variable	**Cuts**
P_T	≥ 10 GeV
$COTAxialHits$	≥ 2
$nCOTHits$	$> 60\%$ of last layer of the COT

Table 2.7

Table outlining the definition of tracks that we veto against in the exclusive $\gamma + \not\!\!E_T$ final state.

Photons

From this list of general jet definitions we can apply further discrimination in order to identify photons. The CDF detector has been used to accurately identify and measure high energy photons for over 25 years using well established identification requirements [66]. For this analysis we only consider photons found in the central part of the detector ($|\eta| < 1.0$) owing to the fact that the central region is not only better instrumented, but the EMTiming system has been fully calibrated and validated in this region.

The list of photon identification requirements given in Table 2.8 allow us to correctly select photons in the fiducial region of the CEM as well as being able to distinguish them from decays of $\pi^0 \to \gamma\gamma$, hadronic jets, and electrons. The full description of the standard photon identification variables is given in Appendix A, but we do draw attention to the fact that the list here differs slightly from the standard photon ID in five ways.

I **Eliminate CES χ^2 Variable:** The lateral shower shape of the photon at shower maximum as measured by the CES is normally compared to that resulting from test beam and a χ^2 fit < 20 is usually required. However, it has been shown that this is a poor cut to use in searches for delayed photons which come from the decay of some long lived heavy object [42]. This is mainly due to the fact that no good prediction of what the CES χ^2 exists for real photons coming from different angles. Thus as was done in previous delayed photon searches we exclude this cut.

II **PMT Aysmmetry Cut:** In the Central Electromagnetic Calorimeter (CEM) an energy deposit is identified from the output of the two photo-multiplier tubes (PMTs) that collect the light from the scintillator in the CEM. A high voltage breakdown in the PMT unrelated to an energy deposit in the CEM and can create a false electron candidate if this happens to correspond with an

unrelated collision track. As the rate of this potential background is small and the rejection power offered by the introduction of the cut is nearly 100% we simply cut away any spurious deviation from the symmetric PMT distribution expected from photons.

III **EMTiming Requirement:** Requiring that the EMTiming system have a reasonable readout associated with the arrival of the photon (electron) is necessary since we will use this information for calibrations. The default value in the analysis code for the EMTiming variable is set to be -999 ns and cut requiring times less than $|900|$ ns ensures there was a timing measurement made.

IV **Additional Hadronic Energy Requriement:** In addition to the standard Hadronic Energy fraction cut ($\frac{\text{HadronicEnergy}}{\text{ElectromagneticEnergy}}$) we requrie a sliding Hadronic energy cut (**Had E** $\geq -0.30 + 0.008 \cdot E_T$) in order to reject against cosmic ray events. This "cut" is described in full detail in Section 4.2

V **Total CES Energy:** We use the total of CES energy to help distinguish from high energy collision photons and photons coming from cosmic rays ($CES(E)$). By requiring $CES(E) > 10\ GeV$ we add to our ability to reject events originating from cosmic ray events. This "cut" was first used and is described in full detail in reference [42].

VI **Fraction of CES Energy to the total Energy:** We use the fraction of CES energy over the total energy to help distinguish from high energy collision photons and photons coming from cosmic rays ($\frac{CES(E)}{TotalE}$). By requiring $\frac{CES(E)}{TotalE} > 0.2$ we add to our ability to reject events originating from cosmic ray events. This "cut" is described in full detail in Section 4.2.

Variable	Cuts
$\|\eta\|$	< 1.0 (Central)
Photon E_T *(Measured from Z = 0)*	≥ 30 GeV
Fiducial (Ces $\|X\|$ <21 cm, 9< Ces $\|Z\|$ <230 cm) Tower 9 excluded	$= 1$
$\frac{HadronicEnergy}{ElectromagneticEnergy}$	< 0.125
Energy Isolation $E_T^0 \geq 20$ GeV	$E_{cal}^{iso} < 2.0 + (0.02 \cdot (E_T^0\text{-}20))$
Track Isolation	$\leq 2.0 + (0.005 \cdot E_T^0)$
N3D Track Rejection If N3D Track = 1	≤ 1 Track $P_t \leq 1.0 + (0.005 \cdot E_T^0)$
2^{nd} CES Cluster Energy $E_T^0 < 18$ GeV $E_T^0 \geq 18$ GeV	$E^{2nd}CES \leq 0.14 \cdot E_T^0$ $E^{2nd}CES \leq 2.4 + (0.01 \cdot E_T^0)$
$\|PMTAysmmetry\|$	< 0.6
$\|EMTime\|$	< 900
Had E *Hadronic Energy deposited*	$\geq$ -0.30 + $0.008 \cdot E_T$
CES(E) *Total Energy in the CES*	≥ 10 GeV
CES(E)/Total E *Fraction of Energy Deposited in the CES over the total Energy*	≥ 0.2

Table 2.8

Standard central photon identification requirements used to identify photon candidates in the delayed photon analysis. Note, these cuts are the standard CDF definition for photons in addition to requiring PMT Aysmmetry, EMTiming variables, total CES Energy, a sliding CES Energy fraction and additional hadronic energy requirement as well as removing CES χ^2. These variables are defined in more detail in Appendix A.

Electrons

We identify electron candidates in the central region as an isolated central track with information coming from both the silicon tracker as well as the COT associated

with energy that is deposited in the electromagnetic calorimeter [67]. As such, in addition to the standard electron identification variables which have been used successfully at CDF for 25 years, we include a PMT asymmetry cut and a EMTiming time requirement that was defined for photons in the previous section. These electrons are the objects, summarized in Table 2.9, are used in Section 3.1.1 to allow us to calibrate further our timing information associated with these objects.

Variable	**Cuts**
Electron E_T *(Measured from Z = 0)*	>30 GeV
$\frac{\text{HadronicEnergy}}{\text{ElectromagneticEnergy}}$	$< 0.055 + 0.00045 \cdot \text{E}$
P_T	> 10 GeV
$\lvert\Delta Z\rvert$ CES	<5 cm
$\lvert\Delta X\rvert$ CES	<3 cm
Isolation	$< 0.1 \cdot E_T$
E/P_T	< 2 *For P_t < 50 GeV*
L_{shr}	< 2
Fiducial (Ces $\lvert X\rvert$ <21 cm, 9< Ces $\lvert Z\rvert$ <230 cm) Tower 9 excluded	$= 1$
$\lvert Z\rvert$	< 60 cm
$\lvert PMTAysmmetry\rvert$	< 0.6
$\lvert EMTime\rvert$	< 900

Table 2.9

Table of standard central electron identification variables. Note, in addition to the standard CDF variables PMT Aysmmetry and EM-Timing requirements have been added to ensure a good timing measurement is made. These variables are defined in more detail in Appendix A.

Further information about the variables used to identify electrons can be found in Appendix A.

Verticies

Generically, a vertex is grouping of tracks near the beamline which indicate that a paticular point in space was the origin of the tracks. In this section we define what is refered to as a "Good" SpaceTime Vertex. The choice of these cuts insure that the SpaceTime Vertexing algorithm is fully efficient and is described in full detail in Reference [62]. Previous vertexing algorithms at CDF [68] have been demonstrated to reconstruct the initial position (z_0) to a high enough degree of accuracy to calculate all the identification variables of interest. However, it is important to this analysis to be able to calculate the initial time of that vertex (t_0) associated with a photon to a higher degree of accuracy then what was previously demonstrated [62]. As such the SpaceTime Vertexing algorithm was developed which allows the ability to seperate verticies that are close in space but happen at different t_0. This vertexing algorithm was used in previous delayed photon searches and is discussed in greater detail in reference [42] and in Appendix A.

Quantity	Cut
ΣP_T	≥ 5 GeV
N_{track}	≥ 3
$\|Z\|$	≤ 60 cm

Table 2.10
Table of standard good SpaceTime vertex identification variables. These variables are defined in more detail in Appendix A.

As shown in Figure 2.7 we can see that the reconstructed distributions for a sample of $W \rightarrow e\nu$ events defined in section 3.1.1. In this sample we require only one electron matched to a vertex thus allowing us to probe the resolution of the SpaceTime vertexing algorithm. Furthermore we exclude the electron track itself from the vertexing in order to properly measure the resolutions without biasing the algorithm.

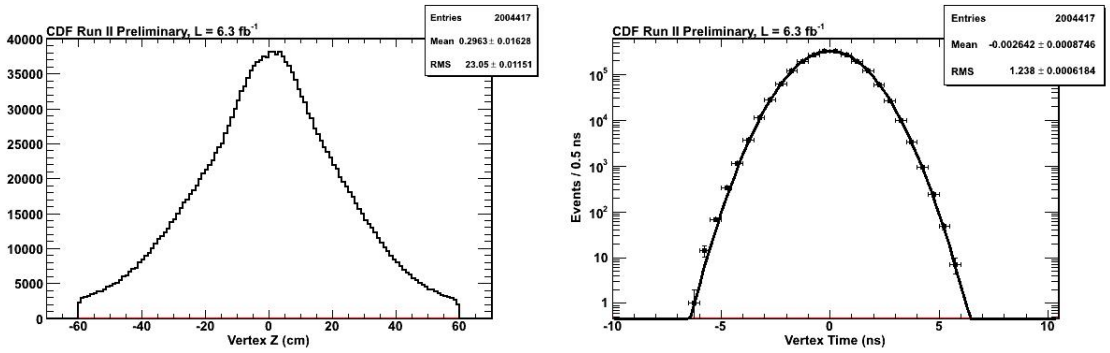

Fig. 2.7. Figure showing the SpaceTime Vertex z RMS to be $\sim$25 cm and the t RMS to be $\sim$1.25 ns for a sample of electrons selected using cuts defined in Table 3.1.

We note that both of these distributions are very Gaussian in nature and the z resolution is $\sim$25 cm and the t resolution $\sim$1.25 ns. These resolutions come from the nature of the longitudinal beam parameters for the proton and antiproton bunches. The details of the particle beam and the underlying collision distribution that can be seen with the SpaceTime vertexing algorithm is discussed in reference [70].

Missing Transverse Energy

At collider experiments, including CDF, collisions occur with nearly no momentum in the plane transverse to the collision, thus by conservation of momentum the vector sum of all the momenta in the final state particles should be zero in the transverse plane. However, particles that do not interact with the calorimeter, like the Standard Model neutrino or the SUSY gravitino ($\tilde{G}$) will cause a momentum imbalance in the detected particles. This missing transverse energy ($\not\!\!E_T$) is defined as the negative of the vector sum of all the transverse energy in the calorimeter towers with $|\eta|$ <3.6. In this analysis the total deposited energy in the calorimeter is calculated relative to $z = 0$ and the x and y coordinates are taken from the beamline position information. Studies of minimum bias events give an estimate of the $\not\!\!E_T$ resolution

of $\sim 0.4 \times \sqrt{\Sigma E_T}$ where ΣE_T is the scalar sum of the transverse energy of the towers in the calorimeter.

It is important to note that there are both non-collision and collision sources of $\not\!\!E_T$. As will be explored in the next sections, transverse energy will not be conserved if particles come from outside the beam or result from instrumental failure.

We next turn to the various "triggers" used in this analysis for selecting events that have been reconstructed offline.

2.4.1 Presamples and Data Sets

We now turn our attention further subdividing our data in various catagories referred to as "presamples". These presamples are used throughout this analysis and allow us to easily create and refer to selection criteria that is specific to a given use case. Each specific set of selection requirements for the various presamples will be given later, for now we simply summarize what the presamples are. The three main presamples used in this analysis include:

1. **Calibration Sample:** This presample will define a selection of data containing an electron that is matched in space and time to a vertex and missing energy (e+$\not\!\!E_T$). We require a match between the electron and the vertex to ensure we are calibrating the time measurements relative to the correct collision time. A vertex that has a $\Delta T < 1.5$ ns ($|t_{electron} - t_{vertex}|$) and $\Delta Z < 1.5$ cm ($|z_{electron} - z_{vertex}|$) is identified as a "Right" vertex and is considered to be well matched. In order to insure that we have an accurate measurement of the initial time of the event we require that only one such right vertex be present in the event. (Note: The electron track is removed from the vertexing algorithm as described Ref [62]).

2. **Exclusive Electron and Missing Energy Sample:** This presample will mirror our final state that we perform the search for new phyiscs in, except

instead of a photon we require an electron. Since the electrons in these events are excluded from use in the SpaceTime vertexing algorithm this presample provides a very good analog to the sample in which the 2008 excess was found (see section 1.5) as well as a data based test of methods explained in section 6.1. The use of the electron track seperate from the vertex will allow us important information about the initial position and time of the event as well as provide a testing ground for our analysis. A summary is given in Table 2.11 and will be described in detail later.

Event Selection
Pass Trigger and Good Run List *(See Table 2.2 and Section 2.4)*
Pass Electron requirements w/ $E_T^0 >$ **45 GeV and** $\not\!\!E_T^0 >$ **45 GeV** *(See Table 2.9 and Section 2.4)*
Pass Beam Halo Rejection *(See Table 4.2)*
Pass Track Veto for Tracks with $P_T >$ **10 GeV** *(See Table 2.4)*
Pass Jet Veto for Jets with $E_T^0 >$ **15 GeV** *(See Table 2.5)*

Table 2.11
List of cuts summarizing the exclusive $e+\not\!\!E_T$ presample.

3. **Exclusive Photon and Missing Energy Sample:** This presample is designed to mirror the selection used in the prelimnary result from 2008 and allow us to study the effects of various background processes in this final state. A summary of this presample is given in Table 2.12.

2.5 Monte Carlo Methods and Samples

Owing to the complexity of the interactions that take place in the detector during collisions, Monte Carlo (MC) simulation often provides the only way to accurately

Event Selection
Pass Trigger and Good Run List *(See Table 2.2 and Section 2.4)*
Pass Tight Photon requirements w/ $E_T^0 > 45$ GeV and $\not\!\!E_T^0 > 45$ GeV *(See Table 2.8 and Section 2.4)*
Pass Beam Halo Rejection *(See Table 4.2)*
Pass Cosmics Rejection *(See Table 4.1)*
Pass Track Veto for Tracks with $P_T > 10$ GeV *(See Table 2.4)*
Pass Jet Veto for Jets with $E_T^0 > 15$ GeV *(See Table 2.5)*

Table 2.12
List of cuts summarizing the exclusive γ+$\not\!\!E_T$ presample.

model both the background and signal processes. A complete generation, simulation, and reconstruction process is available in the standard CDF MC tools [72]. While these tools are expected to do a good job of reproducing many of the interactions in the detector, they are not sophisticated enough for us to trust the true event rates of the production of the various backgrounds as a way to estimate our backgrounds.

The simulation begins by running an event generator known as PYTHIA [73] to generate $p\bar{p}$ collisions and then uses various theoretical cross-sections, initial and final state radiation, as well as hadronization mechanisms to simulate the decay and possible outcomes of various physics processes. The software package known as GEANT3 [74] is then used to simulate the interaction of these particles with the complete detector simulation, thus giving us detector level hit information [63]. This simulation has been used for many years with great success and remarkable accuracy.

Additional effects, such as the additional collisions, during various data taking conditions are simulated and added to the simulation by adding extra collisions (referred to as Min-Bias events). The output of this simulation has been shown to

be an excellent approximation of the production and reconstruction of the physical processes that occur in our detector. Thus, we will be able to use this simulation as a guide for understanding possible biases which could be present in our data and potentially causing an artifical excess above background predictions.

As the EMTiming system is not part of the standard calorimeter simulation, the arrival time is obtained using information already available in the MC simulation. Namely:

$$t_{arrival} = t_{produced} + \frac{|\vec{x}_f - \vec{x}_{produced}|}{|\vec{v}_{part}|} \tag{2.2}$$

where $\vec{v}_{part}$ is the velocity of the particle and $\vec{x}_{produced}$ is the initial position and $t_{produced}$ is the initial time [63].

The true vertex time, $t_{produced}$, takes into account the simulation of the primary vertex position and time as well as the decay parent time needed to propagate through the detector volume. Since in the actual data the calibrations assume that the particle comes from the center of the detector ($z = 0, t = 0$), the arrival time is corrected for the time of flight assuming the particle trajectory is approximately a straight line. Finally, the simulation checks to see if the particle actually interacts with the detector and then applies a Gaussian smearing of the $t_{arrival}$ of 0.5 ns in order to model the intrinsic EMTiming resolution. This information is then recorded in the event and thus allows us to simulate the EMTiming time of MC events to compare to the data. This process has been shown to accurately reproduce the EMTiming system response and resolution to a high degree of accuracy [75].

Having firmly established the tools needed to perform the search for new physics in the exclusive $\gamma_{delayed}$+$\not{E}_T$ final state, we now turn our attention to the calibration and validation of the various timing systems used in this analysis.

3. TIMING CALIBRATION METHODS AND VALIDATION

In this chapter we go into detail about the calibration procedure and the performance of the Electromagnetic Calorimeter Timing System (EMTiming) and the Central Outer Tracker (COT) systems for use in the final photon timing measurement. We use W$\rightarrow e\nu$ events corresponding to the same data taking period as the exclusive $\gamma_{delayed}$+$\not\!\!E_T$ as these W$\rightarrow e\nu$ events have the particular advantage of mimicking our final state (γ+ $\not\!\!E_T$) if we simply ignore the track from the electron when performing the vertexing. As we will see, the combination of timing systems have a combined resolution of 0.65 ns for events well matched to the vertex and that the EMTiming and COT systems show no systematic variations as a function of all the important event observables to less than <100 ps.

We begin by laying out the importance of the accuracy of the timing calibrations as well as the general procedure that will be followed in the timing calibration procedures. From there we describe the data selection requirements as well as more detail on the reasoning behind selecting this subset of events. Next we go into detail about the various calibration distributions and procedures for the tracks from the COT, for vertices constructed using tracks from the COT, and finally for the EMTiming system used in combination with the tracking. Lastly, we present results that demonstrate that the system is well calibrated and has systematic variations that are small compared to the needed tolerances.

Before proceeding, we note that the set of precision calibrations described below are performed after a preliminary calibration has already been done on both the COT and EMTiming systems. These calilbrations on the data are discussed in detail in reference [76], of which we give an example here. Specifically, a preliminary calibration take into account the time required for the PMT signal to travel to the TDC, an initial energy-dependent (slewing) correction due to the use of fixed height ASD's, and a correction that takes into account the energy difference deposited in

the two PMTs. This set of calibrations to the EMTiming system is described in greater detail in Reference [58] and is determined from fits for each channel using high statistics jet data samples. This calibration is done tower-by-tower, but only is done relative to the mean time and collision position of the sample used to select events. Since the mean time and position can vary from tower to tower this means that the calibrations can be off by almost a nanosecond which is outside our tolerance window. We next move to our procedure which is more rigorous in this methodology.

3.1 Overview and Methods

Accurate measurement and understanding of the performance of the various timing systems used in the delayed photon analysis is of the utmost importance in identifying any evidence for new physics using the variable t_{corr} as defined in equation 1.7. Figure 3.1 shows an example of how a mis-measurement of the data could result in a shift of the mean of the wrong vertex distribution. This bias could lead to an "artificial excess" of events in the signal region and may be misidentified as evidence for new physics. This artificial excess could appear in the wrong vertex distribution owing to a systematic shift being present in one system but may not be present in the other. For example, an artificial shift in the arrival time (EMTiming time) that is not corrected for when selecting an incorrect initial time (vertex time) can lead to a bias in the resulting corrected time (t_{corr}). This bias would tend to show up in the wrong vertex distribution since any artificial shift in the timing systems would be exasperated by the fact that a random inital time was chosen from the wrong vertex.

Figure 3.2 illustrates how a large timing shift in the measurement of t_{corr} translates into a potential excess in the number of large time events. Doing a simple calculation where we assume the WV timing distribution is given by a Gaussian with an RMS of 2.0 ns we can integrate the probability for a sample of events to show up in the control region and in the signal region. A timing shift of $\approx$500 ps

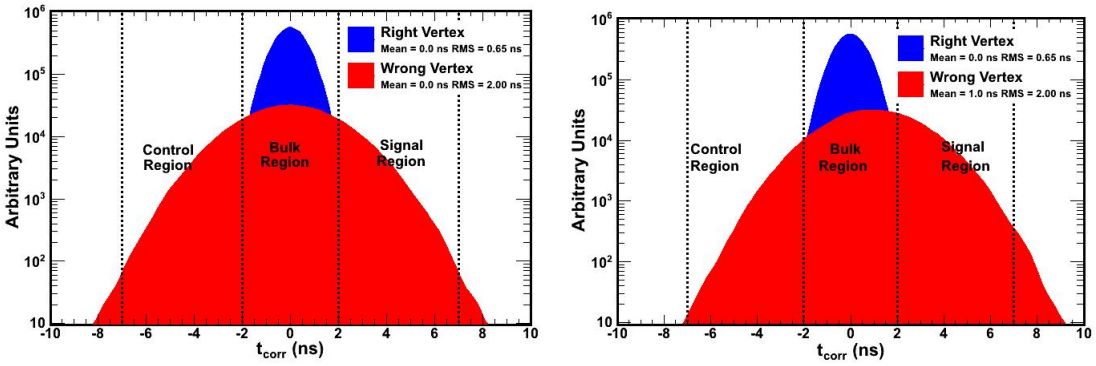

Fig. 3.1. Monte Carlo simulation of a shift in the mean of our timing distribution that can cause an excess in the ratio of the number of events in the signal region to number of events in the control region.

in the wrong vertex distribution (dashed blue line) can lead to an excess of 2 times more events in the signal region than would be found in the control region from SM sources. Moreover, Figure 3.2 allows us to understand what the tolerance for calibrations on the t_{corr} variable should be, specifically as shown by the solid green lines which indicate that variations of less than 100 ps (0.1 ns) have a negligible effect (<10%) in terms of creating an artificial "excess" or "deficit" of events expected in the signal region. With this knowledge, we are able to lay out a general procedure for calibrating the various timing subsystems that go into the t_{corr} variable.

In the next section we describe the event selection for the W$\rightarrow$eν data events as well as the broad overall calibration procedure. It is worthwhile to mention that for use here we use the term 'calibrate' to generally mean that we will calculate the mean of the timing distribution for events which are selected as right vertex events (using the electron track to tell us the vertex of origin of the electron). We will use this mean of the timing distribution as a function of various variables and perform corrections as a function of those variables to ensure that it is always att_{corr}= 0. The goal of these corrections will be to zero mean of the distribution as a function of

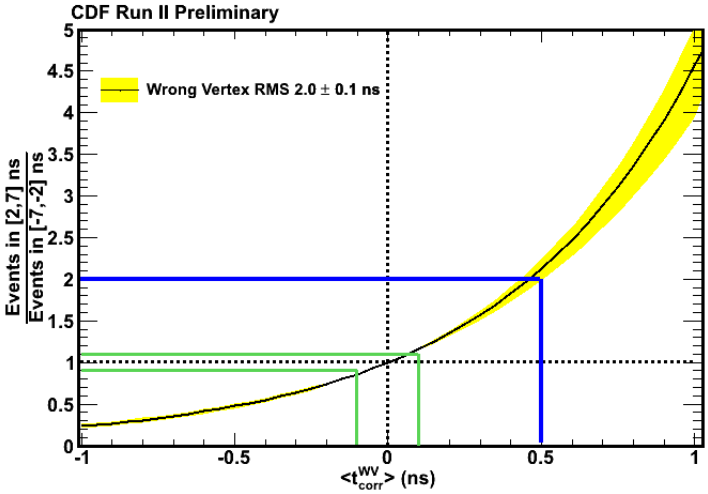

Fig. 3.2. A calculation of how a shift in the mean of the wrong vertex timing distribution can cause an excess in the ratio of the number of events in the timing region 2 ns to 7 ns (Signal Region) to number of events in the timing region -7 ns to -2 ns (Control Region). The nominal ratio of one for a wrong vertex mean of 0.0 ns shown by the dashed black line. The blue line demonstrates a shift of 0.5 ns in the wrong vertex mean can lead to an excess of events expected in the signal region. The solid green lines indicate the desired tolerance, 100 ps, on systematic variations in the t_{corr} variable. This tolerance was chosen because a shift of 100 ps in the wrong vertex mean has less than a 10% effect in terms of an artificial "excess" or "deficit" of events expected in the signal region.

those variables. This procedure includes the calibration of COT tracks, SpaceTime vertices, and the EMTiming system.

3.1.1 Outline of the Calibration Procedure

We begin this section by selecting a series of events in data which pass the W$\rightarrow e\nu \rightarrow e + \not\!\!E_T$ presample. The event reduction for these cuts is given in Table 3.1. We next describe the matching criteria and how they were selected.

Event Selection	Number of Events
Pass Trigger and Good Run List requriments *See Table 2.2 and Section 2.4*	4,858,466
$\not\!\!E_T^0 > 30$ GeV	3,893,252
Identified Electron w/ $E_T^0 > 30$ GeV *(See Table 2.9)*	3,221,638
Passing Beam Halo Rejection *(Discussed in detail later)*	3,184,983
Good Space Time Vertex *Note: Electron Track is removed from the Vertexing* *See Table 2.10*	2,605,338
Only one SpaceTime Vertex is matched to the electron track $\lvert\Delta T\rvert = \lvert t_{electron} - t_0\rvert < 1.8$ *ns* and $\lvert\Delta Z\rvert = \lvert z_{electron} - z_0\rvert < 3.0$ *cm*	2,010,699

Table 3.1
Event reduction table summarizing the cuts used to generate the $e+\not\!\!E_T$ timing calibration sample. Note, the final number of events quoted here is after all calibrations have been applied.

Electrons from W$\rightarrow$ eν events are chosen as an excellent sample for calibrating the detector systems as an electron in the event allows us to correctly identify the origin of the event and thus correctly calibrate the timing systems to this origin. Figure 3.3 shows the variables by which we match the electron track to the vertex as they appear before our precision timing calibrations. Here, ΔT is the difference between the reported track time and the vertex time ($|t_{electron} - t_0|$) and ΔZ is the absolute value of the difference between the reported track initial z position and the vertex z position ($|z_{electron} - z_0|$). A cursory glance at these variables shows evidence for the need of more detailed timing calibrations. This can be seen by noting that the matching between the electron track and the vertex is 'skewed' to a positive time bias as well as having systematic variation as a function of η and ϕ of the electron

track. We note that the Z distribution looks well matched so we do not consider it further.

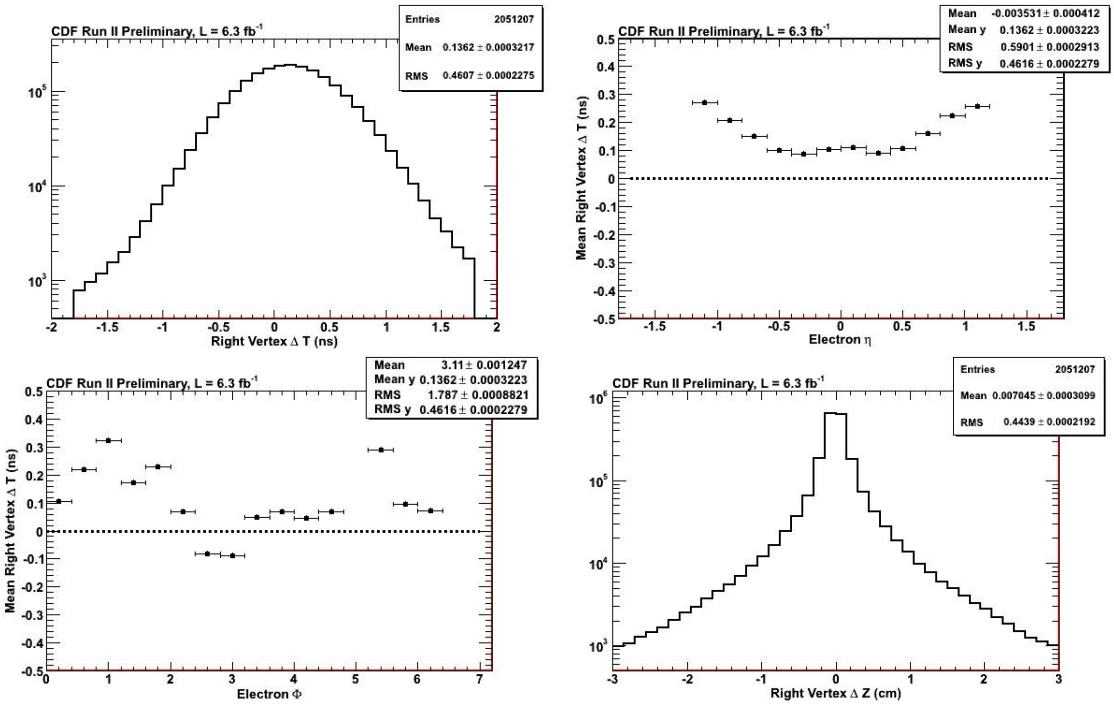

Fig. 3.3. The ΔT between the electron track and the vertex, ΔT vs. electron η, ΔT vs. electron ϕ, and the ΔZ between the electron track and the vertex before calibrations demonstrating the need for further timing calibrations. Note, despite the timing bias, these figures show that the required matching requirements are very efficient.

The first place to begin when calibrating the e+$\not\!\!E_T$ events described above is with the calibration of track timing which are reconstructed from hits in the COT. The calibration of COT tracks is outlined in Section 3.2 and highlights the goal to calibrate the t_0 of the tracks to much less than the individual track resolution which is $\pm$0.4 ns ns. The track resolutino is shown in Figure 3.4. The calibration tolerances are obtained from the tracks by observing the limitations to calibrate the initial time of the track (t_0) given by the resolution of the hit.

As is shown in Figure 3.4 the measured uncertainty on the timing measurement of a track used in the SpaceTime Vertexing ($T_0\sigma$) is ~0.4 ns. Furthermore, the RMS of the tracks within the SpaceTime vertices themselves is ~0.5 ns, indicating that the $T_0\sigma$ of the tracks is likely a low end approximation. This implies that any systematic variations which are under the uncertainty of the measurement of the track itself will not significantly contribute to the systematic variation in t_{corr}. Thus we begin the calibration procedure described in Section 3.2 with the goal to calibrate the t_0 of the tracks such that the systematic variation is less than $\pm$0.4 ns.

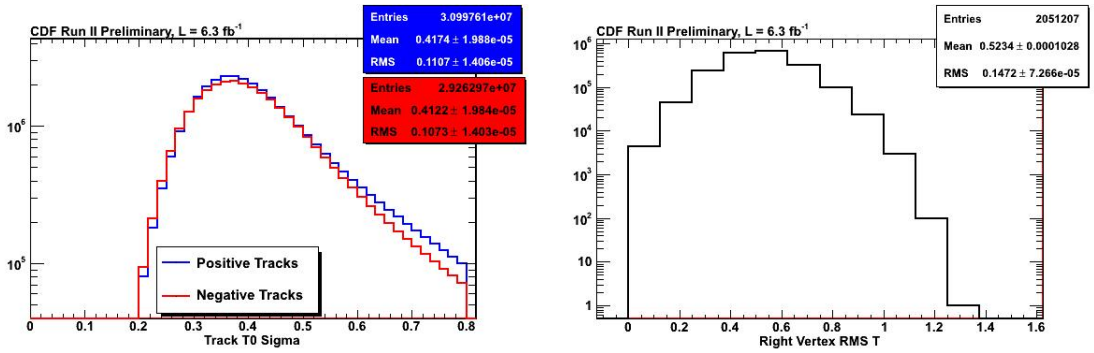

Fig. 3.4. (LHS) COT track $T_0\sigma$ (Blue = positively charged tracks & Red = negatively charged tracks) and (RHS) vertex time RMS distributions. The track $T_0\sigma$ as well as the vertex RMS allow us to infer the intrinsic uncertainty of the timing measurement associated with the tracks and allow us to infer the necessary sensitivity of the calibrations of the track times.

Once the tracks t_0 have been calibrated, these tracks are then used in the SpaceTime vertex algorithm [62]. Said differently, after calibration of the tracks the vertexing can do a better job of combining tracks and give a better overall measruement of the collision position and time. While this will make better measurements, we note that as the track time changes and the vertex time changes after calibrations, this has the possibility of making individual events just pass or fail the selection requirements of the matching. However, since our sample has high statistics, we expect

these issues to be small and only affect the tails of our distribution which are not important to the central value of the measurement. As such, we proceed to check for any bias in the vertex time after track corrections and proceed to remove any systematic variation.

Last but not least, we turn to the arrival time as recorded by the EMTiming system. A proper calibration of the EMTiming system ensures accurate measurement of the arrival time of objects in the calorimeter while avoiding artificial biases due to event topology. The details of calibration of the EMTiming system is given in Section 3.4. We note that the RMS of the EMTiming measurement is approximately 0.5 ns, but what we are interested in is whether there is a bias in the mean of the distribution, any of which will be calibrated out.

The summary of the calibration procedure used to calibrate the COT, vertexing, and EMTiming systems for this analysis is summarized in Table 3.2 and briefly goes as:

Calibration Procedure Summary
Select a sample of W$\rightarrow$eν events with a well-matched electron to a vertex
Re-run the vertexing algorithm, re-select W$\rightarrow$eν events with a well-matched electron to a vertex and calibrate the vertex time
Re-select W$\rightarrow$eν events with a well-matched electron to a vertex and calibratethe EMTiming system

Table 3.2

Table summarizing the calibration procedure for tracks, SpaceTime vertices, and EMTiming times which is repeated until the track, vertex, and t_{corr} timing distributions fall within the tolerances defined for each.

In more detail the procedure is:

I **Select a sample of W→eν events:** Here we use the selection requirements outlined in Table 3.1 to select a sample of W→eν events corresponding to 6.3 fb^{-1} of data.

II **Select and calibrate a set of "good" COT tracks:** For each event we select a set of tracks from our events using the track requirement in Table 2.6 in order to insure that we have good timing and z measurements associated with those tracks. We then pick a set of variables that have a strong impact on the track time and fit the data using polynomials as well as cross terms in order to create track-by-track corrections which are then applied run-by-run (The variables as well as the procedure is described in more detail in the Section 3.2). These corrected tracks are then used to create SpaceTime vertices.

III **Calibrate "good" SpaceTime vertices:** After the vertexing has been performed we select "good" SpaceTime vertices as defined in Table 2.10 and reselect event that have a well matched electron to the vertex. We next study these vertices to see if there is any variation as a function of any important variables. We note that this step is necessary because not all of the run-by-run biases associated with the tracking are removed in the previous step. The vertexing provides a more unbiased estimate of the collision time and position by using the combination of their measurements. For this reason, we note a bias in the overall vertexing measurement and, at this stage, calibrate this out (described in Section 3.3) on a run-by-run basis.

IV **Calibrate the EMTiming System:** After vertexing calibrations are done we reselect events and calculate t_{corr} for each electron so that we can calibrate the EMTiming system. In a manner similar to that of tracks, we find the mean of the t_{corr} for these well matched electrons as a function of many variables and look for variations. Our calibration versus variables which have a strong impact on the EMTiming time (described further in Section 3.4). It should be

noted that we calibrate this variable based on t_{corr} and not the raw EMTiming time in order to avoid introducing any artificial biases due to event topology and are instead calibrating against real detector effects. Such a potential bias will be shown in Section 3.5 and fixes the procedure that was originally used in [42].

In the next sections we lay out the individual procedures for COT Tracks, Space-Time Vertices, and the EMTiming system. Finally, we present the results of all these individual calibrations on the t_{corr} variable and demonstrate that we have removed systematic variations as a function of all the important event observables to less than <100 ps.

3.2 Calibrating COT Tracks

In this section we detail the procedure for calibrating "good" COT tracks for use in the SpaceTime vertexing. As described previously, we begin the calibration procedure with the goal to calibrate the t_0 of the tracks such that the systematic variation small compared to the intrinsic resolution of the track itself of ± 0.4 ns. Table 3.3 gives the summary of the track calibration procedure, a more detailed description follows:

COT Track Calibration Procedure Summary
Selection of W$\rightarrow$eν candidate events
Select variables that have an impact on the track time (Run Number, $T_0\sigma$, ϕ, η, d_0, and q)
Create the mean track time as a function of each of these variables and apply the timing corrections

Table 3.3
Table outlining the COT track calibration procedure.

1. **Selection of W→eν candidate events:** Select W→eν candidate events where the electron track is well matched to any good SpaceTime vertex (See Table 3.1).

2. **Select variables that have an impact on the track time:** Use a set of variables that have a strong impact on the mean of the track time. We find that the following variables are important: Run Number, $T_0\sigma$, Φ, η, Impact Parameter, and Charge where each variable is described in Appendix A.2. These five tracking parameters are used because they uniquely describe the 3 dimensional track trajectory and have large systematic variations which effect the mean time.

3. **Create the mean track time as a function of each of these variables and apply the timing corrections:** All tracks are grouped by charge and run number and then we determine the mean of the timing distribution is determined. The calibration procedure is to perform a polynomial fit of the timing distribution as a function of these variables, taking into account correlations from their cross-terms as many variables are highly correlated in the original tracking fit procedure. We the apply these corrections and iterate, including re-selection of matched events, until they converge within ±0.4 ns.

The 1-dimensional results for the mean of the timing distributions, after first event selection but before calibrations, is shown in Figure 3.5. As is clear, positive and negative charge appear very different and there is significant variation in the mean time as a function of many of the variables. Not only is the mean track times not centered at $t_0 = 0$, but they also show systematic variations on the order of 1 nanosecond. Additionally, these variations change independently over time (as a function of run number) as well as becoming increasingly worse for low p_T tracks. This is especially troublesome for the exclusive $\gamma_{delayed}+\not{E}_T$ analysis since we explicitly veto any event that has large p_T tracks, thus most of our vertices are made up of

these poorly calibrated tracks. Figure 3.6 shows how these poorly calibrated tracks effect even our selection of e+$\not\!\!E_T$ events by looking at the individual electron track time variables before calibrations. We draw attention to the fact that the electron track mean time is not well centered at $t_0 = 0$ but there is large systematic variation as a function of η, ϕ, and run number.

Next, a polynomial fit is applied to these distributions to calculate the amount that needs to be subtracted off taking into account that these variables are correlated accounting for all the cross terms. Figure 3.7 shows the mean track times as a function of the 1-d variables after applying the calibrations and iterating multiple times. We note that for the COT tracks calibrated there is no longer any significant difference between positive and negative tracks as was seen before the calibrations. Additional studies showed that the tracks are well calibrated in two dimensional profile plots as well. Furthermore, the systematic variations of the track t_0 are all well within the 0.4 ns tolerances versus the dominant variables. It is important to draw attention to the fact that the range of the y-axis in the plots before calibrations (Figure 3.5) was large ranging from -1.5 ns to 1.5 ns while the range shown after calibration (Figure 3.7) is now -0.5 ns to 0.5 ns. Thus, the structure that is visually present in Figure 3.7 is significantly exaggerated when compared to the plots before calibrations. Furthermore, Figure 3.8 shows the effect these track calibrations have on the electron track time showing that much of the variation is now gone, despite the fact that some residual variation in ϕ remains. This variation in ϕ is well within the individual track resolution and is thus not considered a problem for vertexing. With a well calibrated COT timing system, we next move to vertex calibrations.

3.3 Verticies

Once the tracks t_0 have been calibrated using the procedure described in the previous section these tracks are then used in in the SpaceTime vertexing algorithm described in Section 2.4. Since the measurement of the initial time of the event is

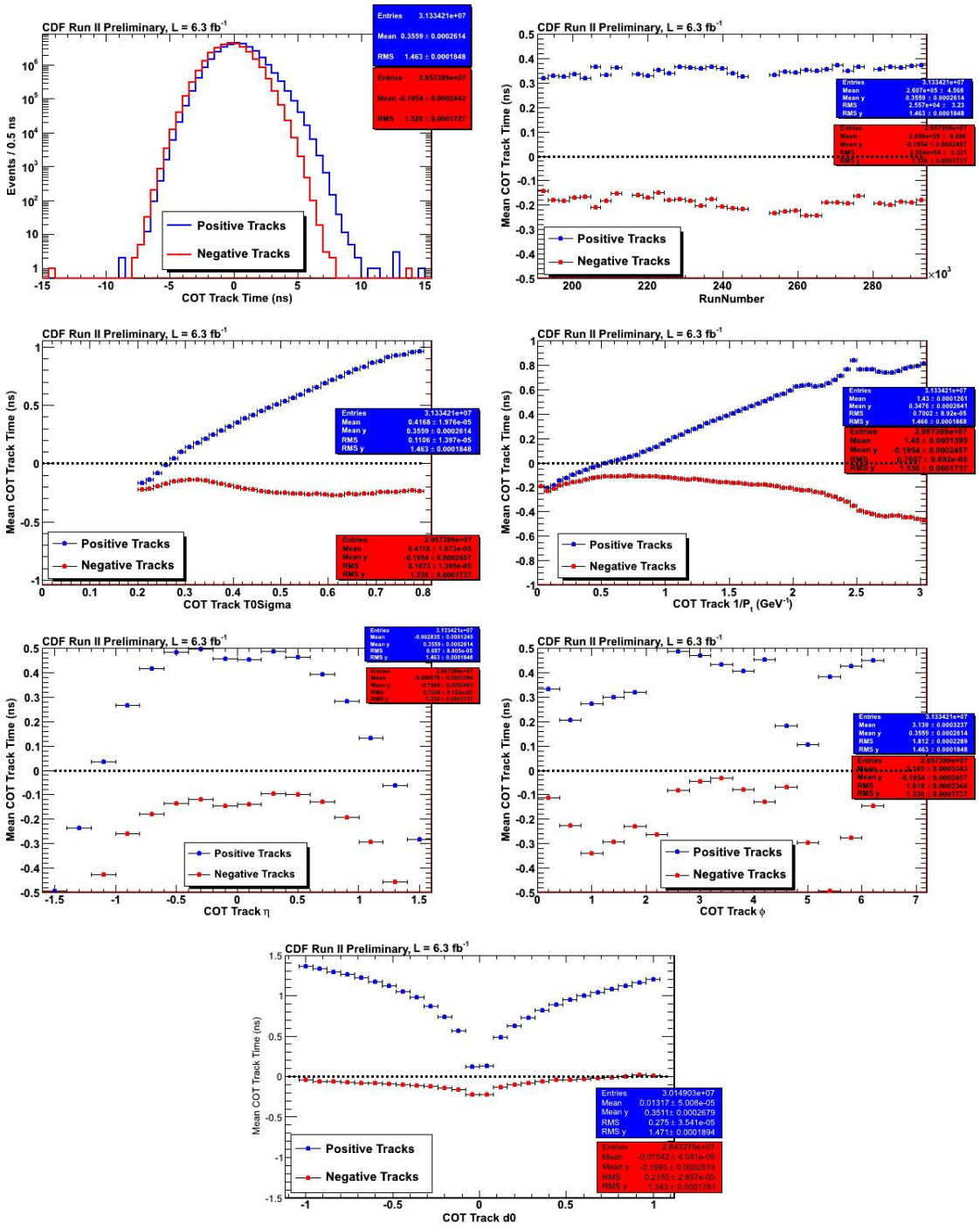

Fig. 3.5. The COT track time for positive (blue) and negative charges (red) in the top left and the mean time of the COT tracks plotted as a function of various variables. Note the scale on the y-axis in some of the plots is much larger than others.

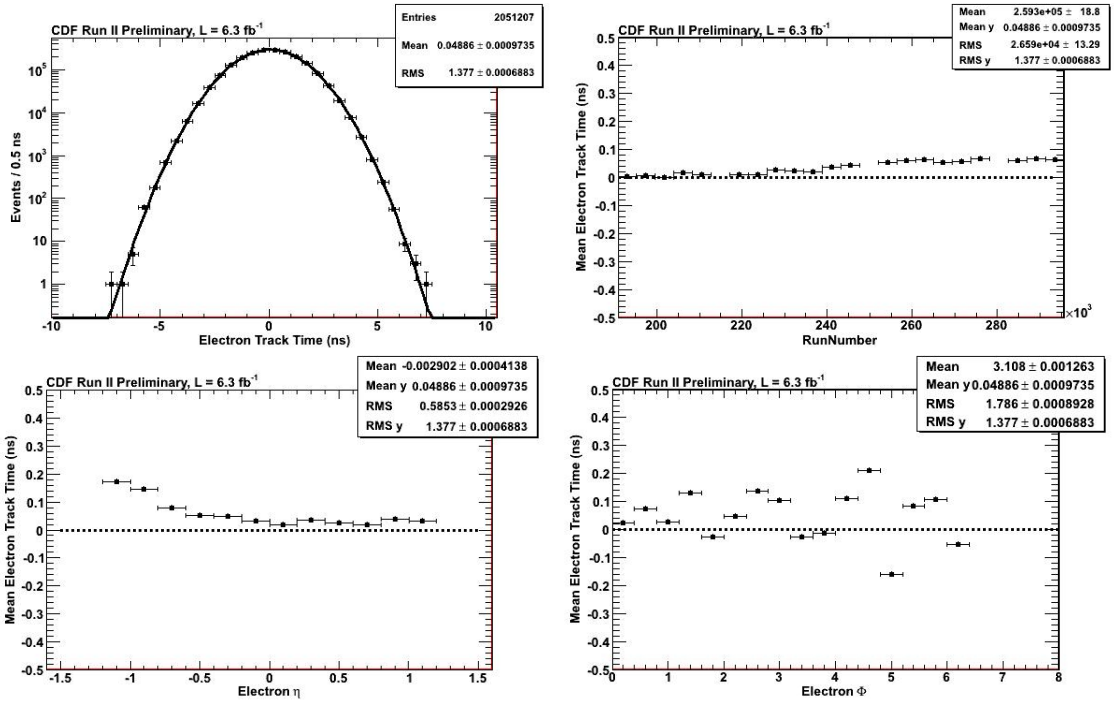

Fig. 3.6. Electron track timing, and mean time as a function of RunNumber η and ϕ variables before calibrations.

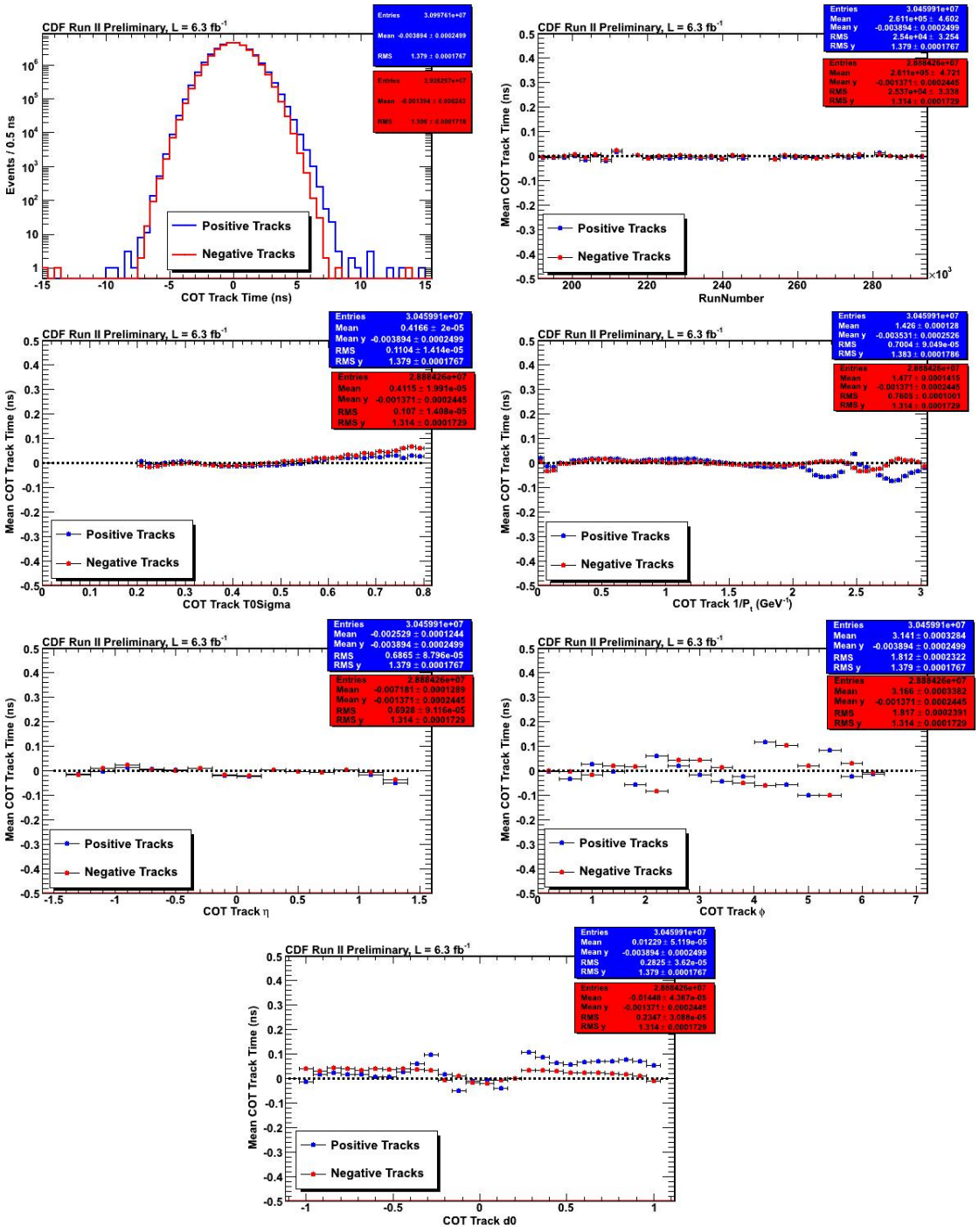

Fig. 3.7. The COT track time after calibrations for positive (blue) and negative charges (red) in the top left and the mean time of the COT tracks plotted as a function of various variables. Note the scale on the y-axis in some of the plots is much larger than others.

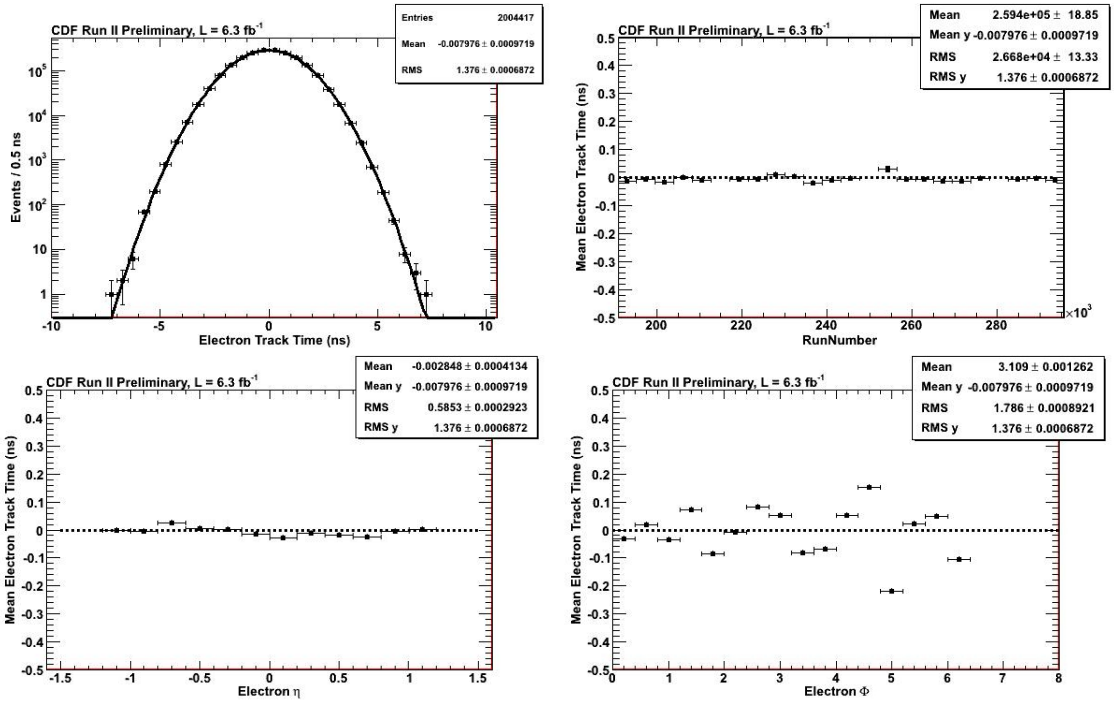

Fig. 3.8. Electron track timing, and mean time as a function of RunNumber η and ϕ variables after calibrations.

directly extracted from the vertex time information, this is a particularly important quantity to have calibrated as accurately as possible. Thus, we define our tolerance for systematic variation in the vertex calibration to be <0.1 ns.

The vertex timing distribution after track calibrations and re-selecting the sample can be seen in Figure 3.9. We quickly see that there is still a systematic shift in the vertex mean time. This likely results from the fact that the SpaceTime vertex algorithm only selects a subsample of all the tracks which were previously uncalibrated. As a result any bias in the algorithm may introduce a slight offset in the mean time and thus need to be corrected for. We note that this effect is small, only has a shift of ∼55 ps, and we have more that enough statistics to determine it and thus can remove this offset. We describe the vertex timing calibration procedure which is summarized in Table 3.4.

Vertex Calibration Procedure Summary
Reselect W→eν candidate events
Select variables that have an impact on the vertex time (Run Number)
Create mean vertex time as a function of these variables and apply the timing corrections

Table 3.4
Table outlining the SpaceTime vertex calibration procedure.

1. **Reselect W→eν candidate events:** Reselect W→eν candidate events where the electron track is well matched to a good SpaceTime Vertex (See Table 3.1).

2. **Select variables that have an impact on the vertex time:** Use a set of variables that have a strong impact on the mean vertex time. Namely: run number since this variable has the overall systematic shift in the mean time.

3. **Create mean vertex time as a function of these variables and apply the timing corrections:** For every event read out the SpaceTime vertex time

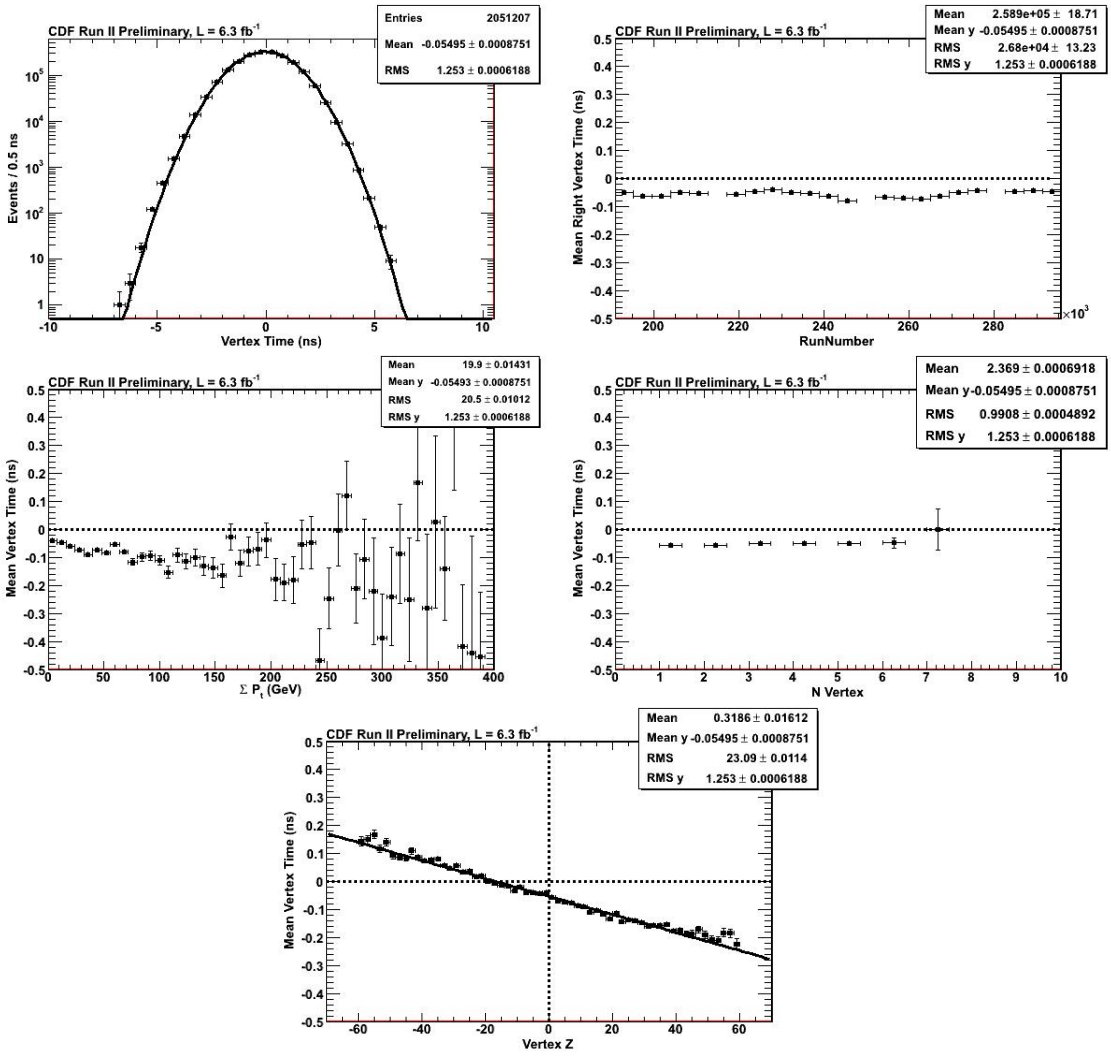

Fig. 3.9. Spacetime vertex time versus various variables demonstrating that even following the COT track calibrations there is still a systematic offset of the mean time on the order of 55 ps, thus necessitating a simple calibration subtraction.

as well as the associated run number. Average all the times within the same run number and subtract off the difference from $t_0 = 0$ in the average. Apply the generated corrections and repeat until the iterated correction becomes <0.1 ns per run.

The results of this calibration can be seen in Figure 3.10. Clearly, these corrections maintain the vertex time distribution to be Gaussian to many sigma and well centered at $t_0 = 0$. Figure 3.10 also shows the mean vertex time versus other variables (vertex ΣP_T, number of vertices present in the event, vertex z position) in order to demonstrate that none of the calibrations have introduced any unforeseen biases. Finally, coming back to the issue raised at the beginning of this chapter, Figure 3.11 also shows that the COT track calibrations and the vertex calibration maintain their balance between the track times and the vertex times by plotting the ΔT and ΔZ between the vertex and the electron track versus Run Number and showing them to be well centered and flat over time.

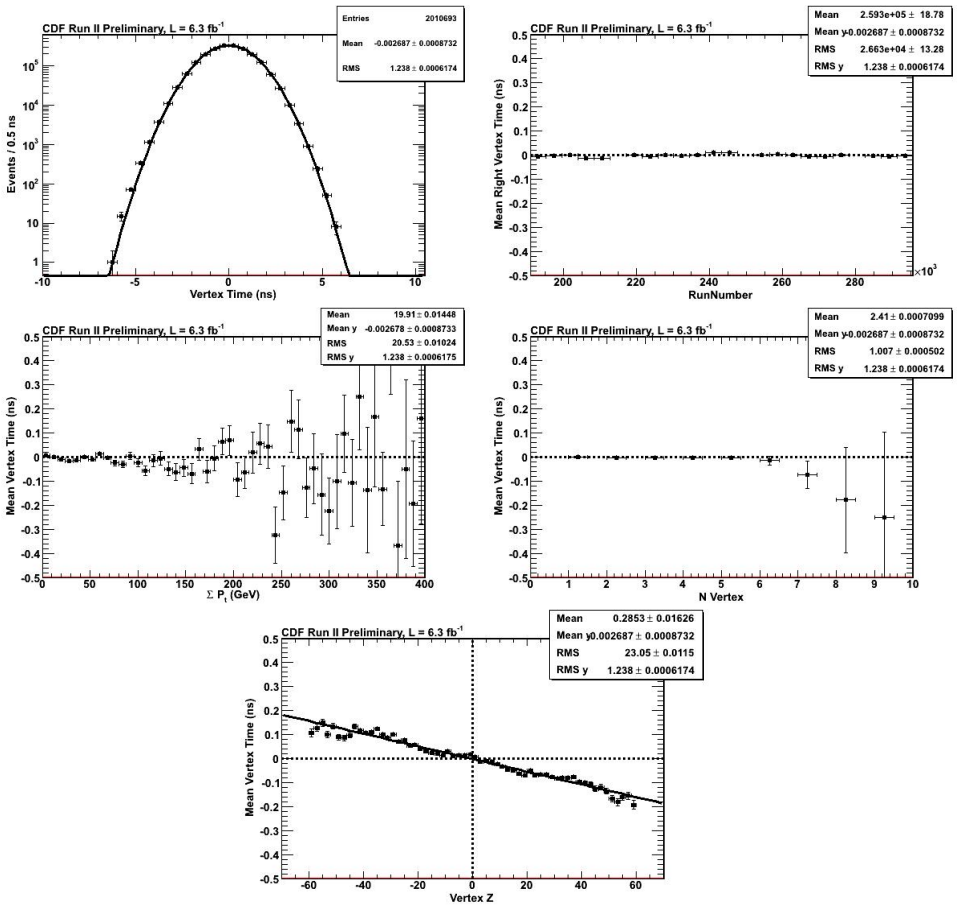

Fig. 3.10. SpaceTime variables after calibrations.

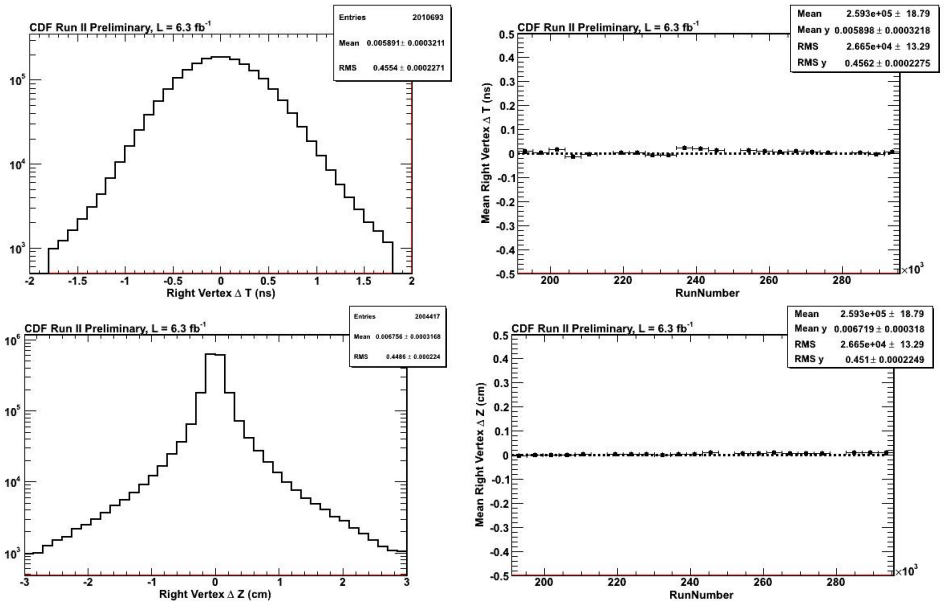

Fig. 3.11. (Top) The ΔT and (Bottom) ΔZ between the electron track and the SpaceTime vertex corrections demonstrating that the track and vertex calibrations allow for a non-bias matching between the electron track and the SpaceTime vertex.

With the vertexing well calibrated, we can move to calibrate the EMTiming system. In the next section we outline the procedure for calibrating the corrected time which takes into account the calibration of the EMTiming system as well as collrelations between the EMTIming system and the COT, as well as event-by-event corrections that occur because of different time-of-flight from the vertex to the CEM tower location.

3.4 EMTiming

In order to calibrate the EMTiming time associated with the well matched electrons one must take special care not to artificially calibrate against any real effects due to the underlying topology of the events selected and instead only calibrate out real systematics in the system. To do this we follow a calibration procedure that

differs slightly from the methods used for tracks and vertices. Previous calibrations ([42]) simply calibrated against the uncorrected EMTIming time, we will show why this is the wrong procedure and outline a more proper procedure that takes into account the best estimate of the time-of-flight of the electron event-by-event.

To calibrate the EMTIming system we calibrate against the mean corrected time as a function of variables that the EMTiming time should not have a dependancy on. This is because the EMTiming system measures the time of arrival, not the time of collision. Thus, we want to make sure we are not biased by time-of-flight systematics. For example, if most of the electrons that hit a tower at high η are from a different average z or t then from low η, then they will be calibrated to different effective times rather than to the mean time of collision in the detector. We find that there are three variables of interest to calibrate in which the corrected time distribution shows significant variation. They are run number, energy, and tower number. These distributions are shown in Figure 3.12 and were chosen because they correspond to the physical location in the detector and exhibited the need for additional calibrations.

Reselecting W$\rightarrow$eν events where we match the electron to the SpaceTime vertex we use the calibrations derived from the 'uncalibrated' t_{corr} distributions obtained from as the parent distributions for the EMTiming calibrations. The calibration procedure is outlined in Table 3.5 and described in more detail below.

EMTiming Calibration Procedure Summary
Reselect W$\rightarrow$eν candidate events
Select variables that have an impact on the corrected time (Run number, Tower, Energy)
Create the mean t_{corr} time as a function of these variables and apply the timing corrections to the EMTiming time

Table 3.5
Table outlining the EMTiming time calibration procedure.

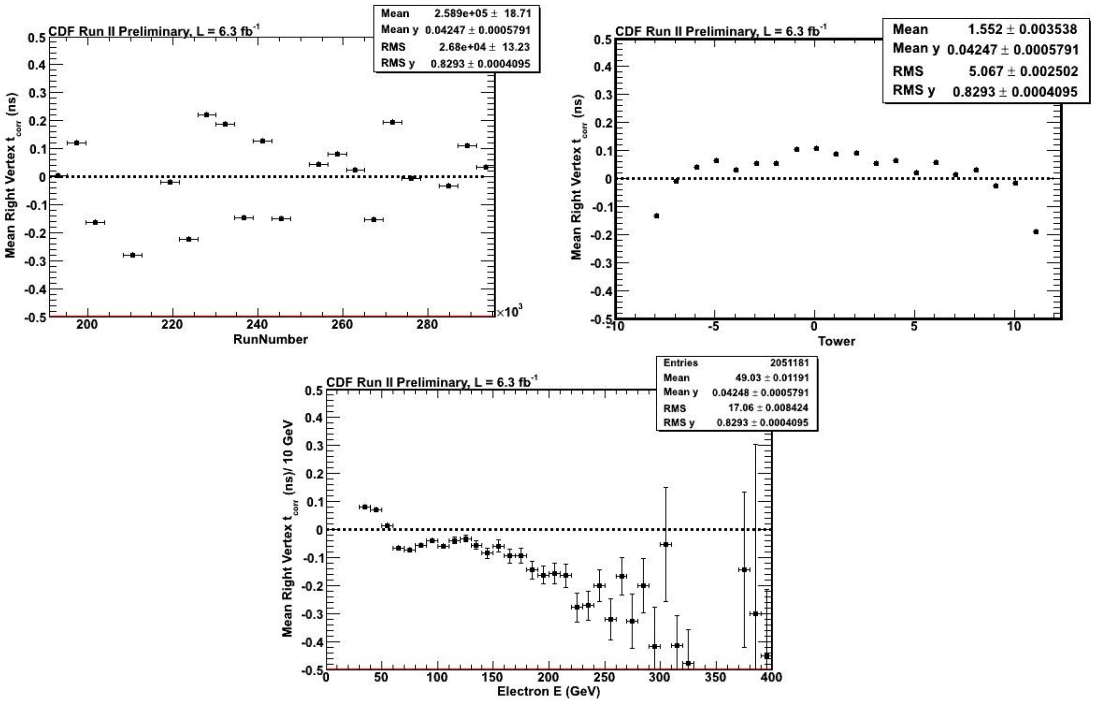

Fig. 3.12. The 'uncorrected' t_{corr} distributions used to generate the run-by-run, tower, and energy calibrations.

1. **Reselect W→eν candidate events:** Reselect the subset of W→eν candidate events where the electron track is well matched to a good SpaceTime Vertex (See Table 3.1). Note this step uses the previous track and vertex calibrations already performed.

2. **Select variables that have an impact on the corrected time:** Use a set of variables that have a strong impact on the mean 'uncorrected' t_{corr}. Namely run number, tower, and energy. These three variables should not have a systematic dependency in the mean t_{corr}.

3. **Create the mean t_{corr} time as a function of these variables and apply the timing corrections to the EMTiming time:** Break the sample into corresponding run sections and zero the average t_{corr} time as a function of run

number, for each tower independently, and energy binned in 5 GeV bins. Apply this set of corrections to the EMTiming time and repeat this set of calibration procedures until the resulting variation in the calibration becomes less then 0.1 ns.

Finally we present the result of the all the timing calibrations, including the EMTiming calibrations described here, performed for the exclusive $\gamma_{delayed}+ \not\!\!E_T$ analysis.

3.5 Summary and Validation Results

Finally, the results for the entire calibration procedure are shown in Figure 3.13 when put together in the corrected time for well matched electrons to a vertex. The resulting t_{corr} distribution has a mean of 0.002 ns and and RMS of 0.69 ns, which is well within the nominal expectations of having a mean of 0.0 ns and an RMS of 0.65 ns. We also see in Figure 3.13 that the corrected time distribution is flat and centered as a function of run number, energy, vertex ΣP_T, η, ϕ, vertex z, and number of vertices in the event. This gives us confidence that we have taken into account all possible sources of calibration bias. We also see that none of these distributions have a systematic variation >0.1 ns thus placing us well within our predefined tolerances for our timing measurement. Finally, we note that the timing distribution is Gaussian out to many sigma. It is possible that the events on the tail are due no non-collision events such as cosmic rays, but this has not been studied in further detail as it has no impact on our conclusions about how well the detector is calibrated.

Additionally we show the results of the EMTiming calibrations on the EMTiming times themselves. As we noted in the previous section, this calibration used the t_{corr} information to generate the calibration tables for the EMTiming system. Figure 3.14 shows the results of these calibrations and it is evident that this calibration did have the desired effect. The EMTiming time for well-matched electrons is Gaussian out to

many sigma and has a mean of 0.05 ns. It is also worth noting that the EMTiming distribution is very flat with little variation over the entire run range as well as having no geometric variation by tower (η), ϕ, or z position (z CES position). This is particularly important since as we saw before calibrations the reported timing did have position dependency which could have potentially introduced an unaccounted for bias.

We note here that a calibration versus energy was also done using Figure 3.12 (t_{corr} vs Energy) as the input distribution for the EMTiming time calibration. The result of this calibration is shown in the last plot in Figure 3.14 and a residual shift between 50 GeV and 75 GeV of $\sim$200 ps can still be seen. The fact that this residual timing shift persists despite the EMTiming variable being flat and centered for all the geometric variables suggest that this timing shift is a real effect and should not be subtracted away without care. The verification of this hypothesis is confirmed when we look at Figure 3.13 and show that the final calibrated t_{corr} variable is flat as a function of energy. Thus we have the justification to the proposition put forward initially that care was needed to be taken when calibrating as to not introduce any artificial biases.

Now that we confirmed our sample is well calibrated and free of timing biases, we turn our attention to the sources of background in the exclusive $\gamma_{delayed}+\not\!\!E_T$ final state. In the next chapter we address non-collision sources of backgrounds and lay out a series of selection requirements to reduce their present in our final state.

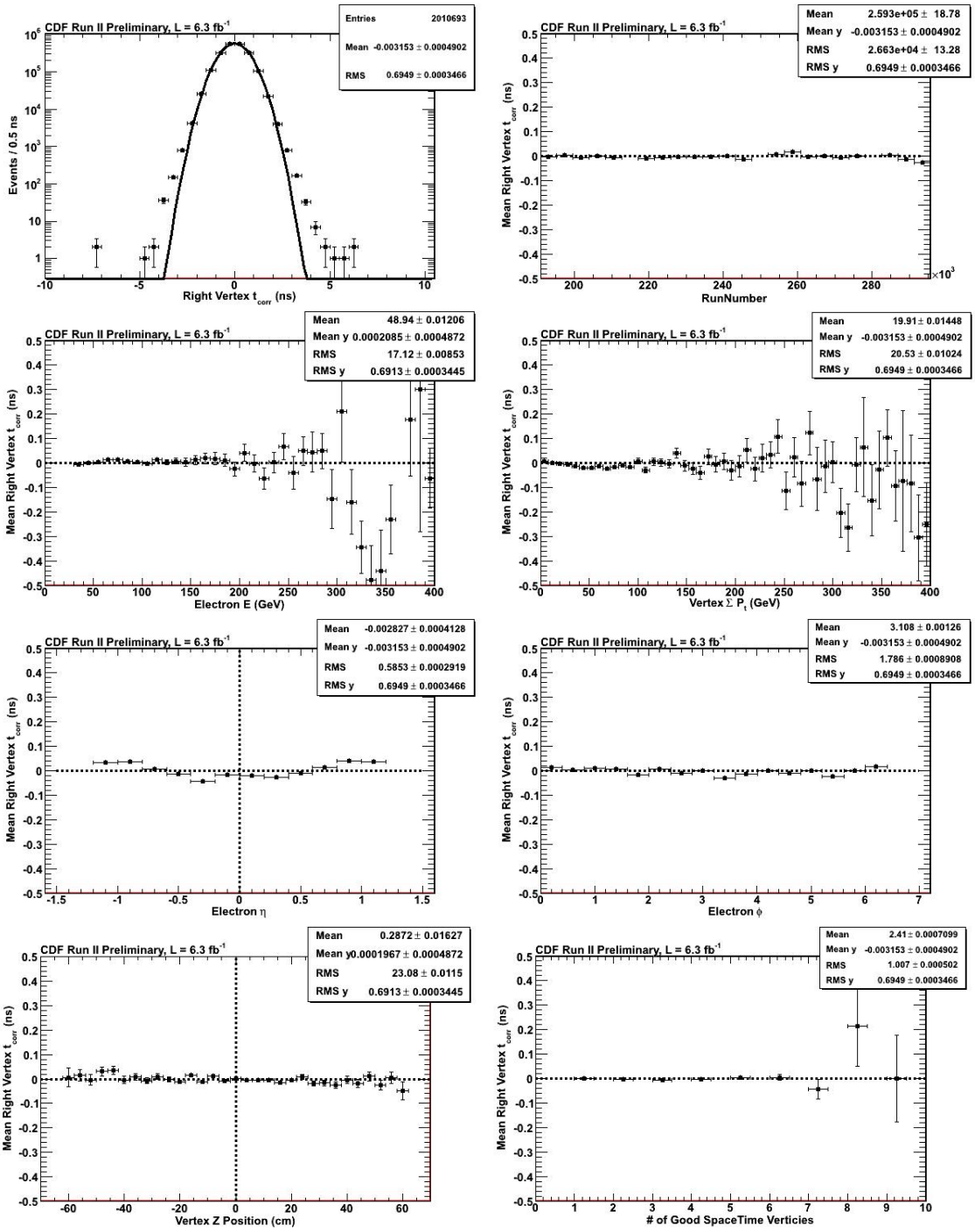

Fig. 3.13. The distribution of t_{corr} after calibrations for the $W \to e\nu$ sample. We note that the distributions have a mean of 0.002 ns and and RMS of 0.69 ns, which is well within the nominal expectations of having a mean of 0.0 ns and an RMS of 0.65 ns. We also see that the corrected time distribution is flat and centered as a function of run number, energy, vertex ΣP_T, η, ϕ, vertex z, and number of vertices in the event.

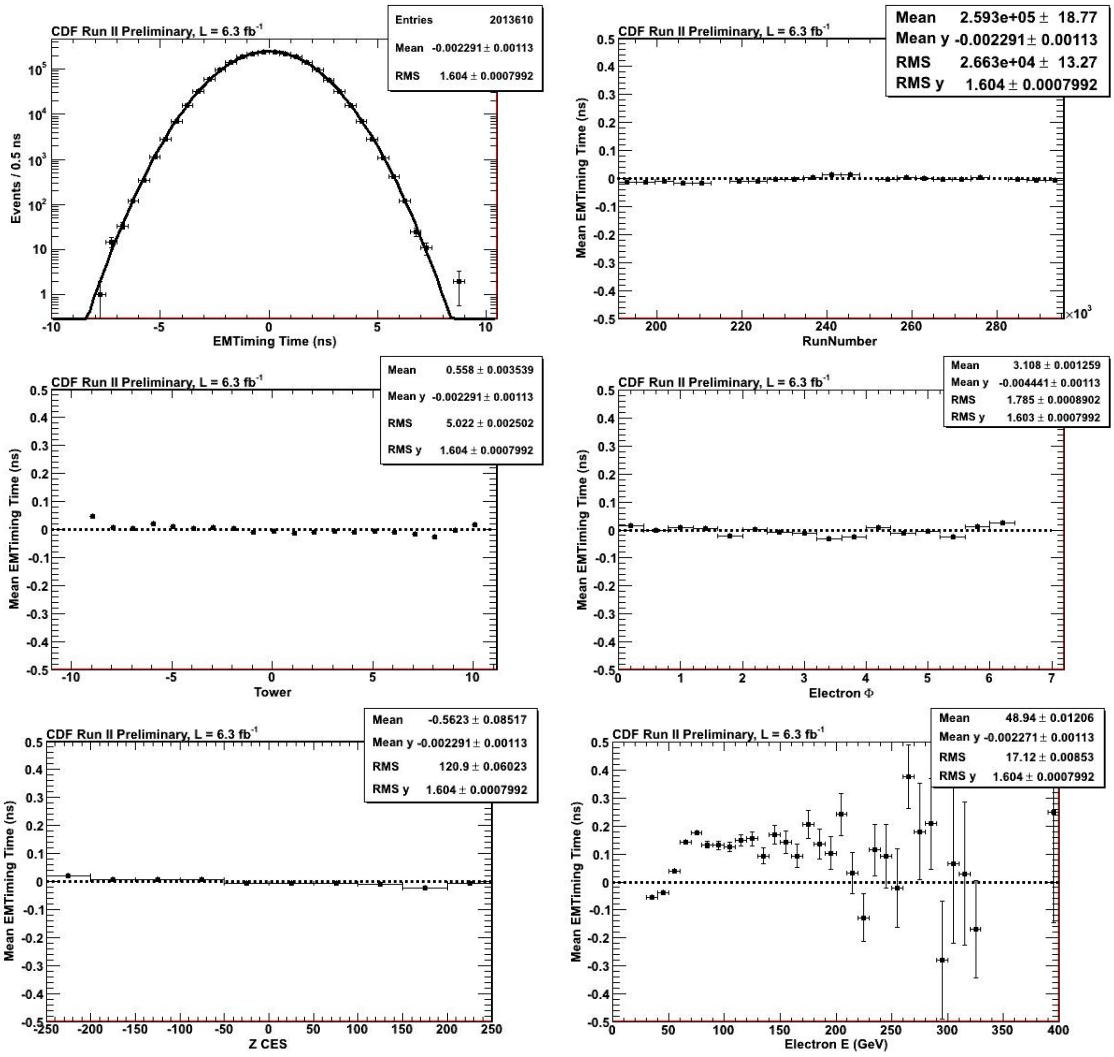

Fig. 3.14. EMTiming variables after calibrations.

4. NON-COLLISION BACKGROUNDS

4.1 Overview

Non-collision based sources can produce objects that look like photons and can fake the exclusive $\gamma_{delayed}+\not\!\!E_T$ final state [45]. The most common sources of these non-collision backgrounds include cosmic ray muons which interact with the detector (discussed in Section 4.2), beam interactions with the beam pipe, commonly referred to as "beam halo" (discussed in Section 4.3), and satellite bunch interactions resulting from unexpected collisions of stray proton antiproton bunches (discussed in Section 4.4). Each of these sources presents a different corrected time distribution and thus affect delayed photon searches differently. In this chapter we will outline the sources of these backgrounds individually and formalize the rejection and estimation definitions used for these backgrounds.

4.2 Cosmic Rays

Cosmic rays are in fact charged particles that originate in outer space and then interact with the earth's atmosphere producing secondary charged particles that then shower down to the earth's surface, as shown schematically in the top of Figure 4.1. If these particles have an energy of ∼GeV they can reach the surface of the earth and interact with our detectors [48]. The bottom of Figure 4.1 shows a cartoon representation of how if a cosmic ray happens to occur in coincidence with a collision in the detector this can lead to both an incorrectly assigned photon to a vertex that had nothing to do with its production as well as leaving an imbalance of energy in the detector which is misidentified as missing energy.

This process can produce a background for analyses using photons if the cosmic ray produces a deposit of energy in the detector that is incorrectly identified as a photon. This mis-identification of a photon can occur if the cosmic ray produces an

electromagnetic cluster via a bremsstrahlung interaction or a catastrophic showering within the EM calorimeter. The unique topology of a cosmic ray event allows us to develop a series of cuts to help veto against mis-identifying an EM cluster from a cosmic ray event versus a real photon coming from a collision.

There are three main selection criteria used in this analysis to veto events which are likely to have originated from cosmic rays. All of these selection criteria ("cuts") take advantage of the fact that a cosmic ray will come from the outside of the detector and propagate inside (the reverse of how a collision created photon will go). The first of these utilizes the muon subdetector located on the outer radius of the CDF detector, the second examines the energy found in the hadronic calorimeter, and the third looks at the fraction of total energy found in the CES in order to reduce the rate at which cosmic rays enter our sample.

The first of these cuts known as a "muon-stub" veto used to reject photon events coming from cosmic rays has been used at CDF and in previous delayed photon searches with great success [42, 45]. This cut is discussed in more detail in Appendix B, but it is sufficient to remark here that this selection utilizes CDF muon detectors. The muon detection system is contained on the outer radius of the CDF detector and thus a cosmic ray may show activity in this outer detector within a close angle to the electromagnetic cluster giving an indication that a particle may have passed from the outside of the detector inwards.

The second of these cuts is what is known as a "sliding" cut on the amount of energy we find in the hadronic calorimeter as a function of E_T. The details of this cut can be found in Appendix B.2, but again we are using the unique topology of a cosmic ray event and the concentric nature of our detector to distinguish real photons from objects that propagate from the outside inwards. Specifically, we expect high energy photons from collisions to end up showering through the electromagnetic calorimeter (located closer to the collision point) and leaving some small fraction of its energy in the hadronic calorimeter (located further out from the collision point).

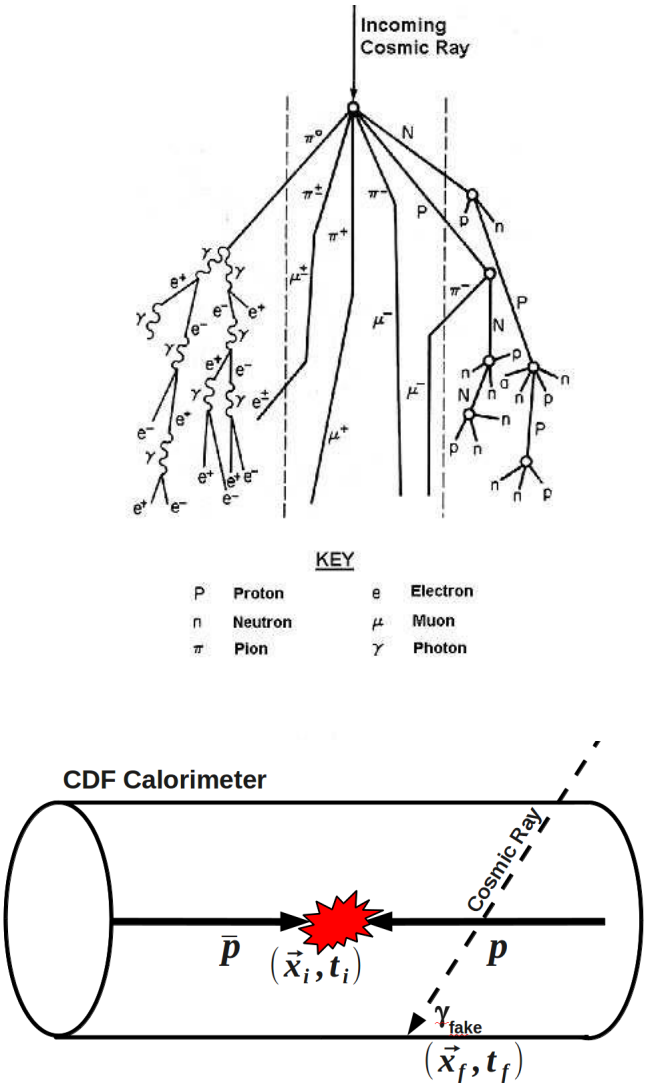

Fig. 4.1. (Top) Cartoon schematic of how a incoming cosmic ray can interact with the atmosphere and create a cascade of particles which, if they originate with enough energy, can reach the surface of the earth and appear in our detector. (Taken from Reference [49] (Bottom) Schematic view of how a cosmic ray can create a fake photon in the detector if it happens to arrive in coincidence with a collision.

However, cosmic ray photons resulting from bremsstrahlung interactions or a catastrophic collision in the EM calorimeter will leave very little energy in the hadronic

calorimeter. As summarized in Table 4.1, we arrive at a selection criterion of the HadronicEnergy $\geq$ -0.30+0.008 $\cdot E_T$. In Appendix B we show that this cut is 95% efficient for electron data with a 66% rejection power for cosmic ray photons.

The third of the cosmic ray veto cuts we use takes advantage of the fact that comic rays photons will deposit a very small fraction of their total energy in the Central Electromagnetic Shower detector (CES) when compared to the total energy in the rest of the calorimeter tower. As detailed in Appendix B.3 we use a cut on the fraction of CES energy over the total energy >0.2 to help distinguish high energy collision photons from photons coming from cosmic rays ($\frac{CES(E)}{TotalE}$ >0.2). Ultimately, as shown in Appendix B, these two new cosmic ray cuts are shown to be 92% efficient for collision electrons and have a 76% rejection of cosmic ray photons. These cuts are shown to help reduce the dominant background of cosmic rays in the exclusive γ+$\not\!\!E_T$ sample of 3/4 when compared to the cosmics rates estimated before using these cuts.

Variable	**Cuts**
N μStub $\Delta\phi < 30^\circ$ *Number of Muon Stubs in $\Delta\phi < 30^\circ$*	< 1
Had E *Hadronic Energy deposited*	$\geq$ -0.30 + 0.008 $\cdot E_T$ Sliding cut as a function of E_T
CES(E)/Total E *Fraction of Energy Deposited in the CES over the total Energy*	≥ 0.2

Table 4.1

Summary of requirements used to veto photon candidates as originating from cosmic rays. Note, the hadronic energy cut (Had E) and the fraction of energy deposited in the CES (CES(E)/Total E) are included in the photon ID variable listed in Table 2.8. We include them here in order to explain why these non-standard cuts are present in the Photon ID used in this analysis.

Having established the basic event selection criteria used to veto against cosmic ray events, we now turn to detailing the method by which we estimate the rate at

which cosmic rays enter our sample. Cosmic ray sources interact with the detector essentially at random in time with respect to when we are taking data. Thus we expect to see the corrected time from cosmic rays to show up flat with respect to the time integration window. This suggests one way to estimate the cosmic ray rate in the signal region (2 ns - 7 ns) by going sampling a timing region where we do not expect to see any collision sources. One such timing region where we do not expect to see any photons coming from collision sources is from 20 ns - 80 ns.

Thus, we are able to estimate the rate of cosmic ray interactions present in our sample, as shown schematically at the top of Figure 4.2, by extrapolating the rate observed from the region 20 ns to 80 ns. As we can see from the bottom of Figure 4.2, when we select photon data from our $\gamma+\not\!\!E_T$ presample defined in Section 2.4.1 and reverse the cosmics veto in Table 4.1 as well as explicitly require that no SpaceTime vertex was reconstructed, the timing distribution does in fact appear flat with respect to time. Furthermore, we see that we can use the rate at which cosmic ray events occur from 20 ns - 80 ns and take a straight line extrapolation to estimate the rate we expect to see in the signal region (2 ns - 7 ns).

4.3 Beam Halo

Beam Halo related backgrounds arise from particles created in interactions between the beam and material near the beam pipe upstream of the CDF detector. These particles then travel parallel to the beam, as shown in Figure 4.3 and thus form a "halo" around the beam, hence the name. This beam halo can traverse the hadronic and/or electromagnetic calorimeters where if they undergo a minimum ionizing interaction they may deposit energy in the detector. While these particles typically leave a small amount of energy in multiple towers, they can deposit significant energy in a single tower and thus mimic a photon candidate in the detector. Since the photon is uncorrelated with the collision this produces an equal and opposite amount of $\not\!\!E_T$ in the detector. These beam halo "photons" typically arrives a few

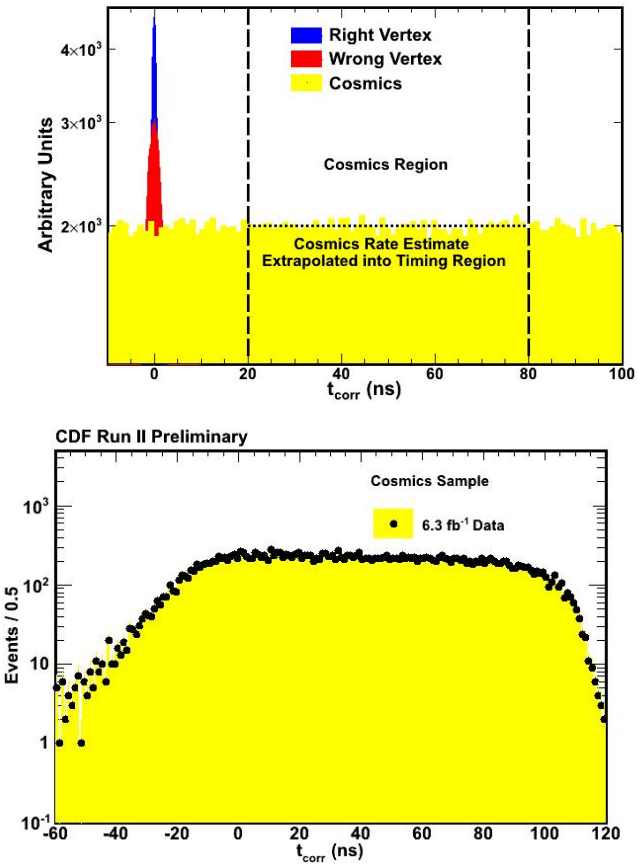

Fig. 4.2. (Top) Schematic of the timing distribution of cosmic ray events present in photon data. The timing distribution is roughly flat over time allowing us to estimate the rate of cosmics in the signal region by measuring it in the region 20 ns $< t_{corr} <$ 80 ns. (Bottom) Timing distribution of cosmic ray events selected from photon data by applying anti-cosmic ray rejection cuts. The timing distribution is roughly flat over time allowing us to estimate the rate of cosmics in the signal region by measuring it in the region 20 ns $< t_{corr} <$ 80 ns.

nanoseconds earlier than prompt photons from collisions owing to the nature of the beam structure which was outlined in Section 2.1; this makes them potentially a large source of γ+$\not\!\!E_T$ events, but very few in the signal region. Similarly, while the rate is lower, these beam halo "photons" also arrive at ∼18 ns intervals following the pri-

mary collision and can be observed with the EMTiming system. Therefore, for these events to appear in the signal region we need events from beam halo interactions to occur early or for resolution issues to push them into the signal region.

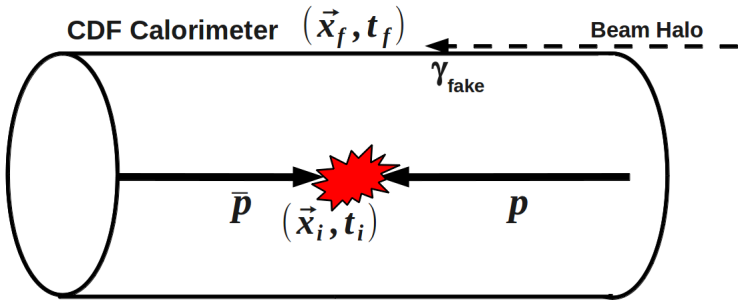

Fig. 4.3. Schematic view of how beam halo can create fake photons in the detector if they happen to arrive in coincidence with a collision.

Like the cosmic ray photons, the unique topology of beam halo events lends itself to developing a set of rejection cuts to veto "photons" coming from beam halo sources. The cuts summarized in Table 4.2 have been well vetted and used in previous delayed photon searches at CDF with great success as shown in references [39,42,45]. It should be noted that these cuts are used on the "logical or", such that if the event fails either one it is discarded as likely coming from a beam halo source.

seedWedge *N Hits in the same wedge as the electron*	> 8
NHadPlug *Number of Plug Hadronic Tower Hits*	≤ 2

Table 4.2
Summary of requirements used to identify and veto photon candidates as originating from beam halo sources.

Figure 4.4 shows the timing distribution coming from the $\gamma + \not\!\!E_T$ presample defined in Section 2.4.1 when we reverse the beam halo cuts defined in Table 4.2 and explicitly require there to be no SpaceTime vertex reconstructed in the event. Immediately it can be seen that the structure of the timing events is exactly what we expect from the beam structure with the majority of events coming slightly before $t_{corr} = 0$ ns and then peaks at ∼18 ns and 36 ns corresponding to the radio frequency bucket length of the beam. The beam halo veto cuts in Table 4.2 have been shown to be nearly 100% efficient for real photons and electrons while vetoing almost all the associated beam halo events [45].

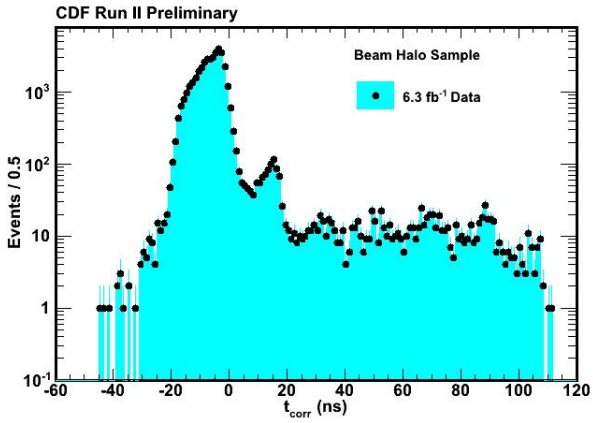

Fig. 4.4. Timing distribution of beam halo events selected from photon data by applying anti-beam halo rejection cuts. Here you can see the structure in the timing distribution created during the coalescing of the proton-antiproton bunches.

The first of the beam halo cuts looks for activity in the same wedge as the "photon" candidate coming from when the minimum ionizing particle was traversing the wedge parallel to the beam. If we find more than 8 hits, each of which have E_T >0.1 GeV (E_T calculated w.r.t. $z = 0$), in adjacent towers in the same wedge as the photon candidate we veto this event as likely having come from a beam halo interaction. This variable is labeled as **seedWedge** in Table 4.2. The second of

these cuts looks at hadronic towers located in the plug portion of the detector in the same wedge as count the number of hits with E_T >0.1 GeV (E_T calculated w.r.t. $z = 0$). If we find more than 2 hits in either the east or west plug then we veto this photon candidate as likely coming from a beam halo source which traversed the entire detector. This variable is labeled as **NHadPlug** in Table 4.2.

4.4 Satellite Bunches

As described in Section 2.1, during the process of forming the proton and antiproton bunches that are used in their respective beams and eventually collided at the center of the detectors, some of these bunches can form outside of their prescribed location in z and t. When these stray bunches are then carried along in the beam we call them "satellite bunches" and they present a unique background to the delayed photon search. As we described in Section 2.1, the Radio Frequency (RF) cavities used in the Main Injector to capture and accelerate the proton and antiproton bunches can create bunches that fall out of the main bunch "bucket" with half RF cavity timing at ∼1% the main bunch intensity [51]. These stray satellite bunches are observed to proceed and lag the main bunches used for collisions [51] as shown in Figure 4.5.

The resulting timing distribution from interactions of these satellite bunches with the main bunches as well as with themselves could potentially produce events with photons that arrive later than we expect. Particularly, we highlight what the t_{corr} distribution would appear as in Figure 4.6 if the satellite bunch interactions produced photons from their collision and we incorrectly assigned a vertex that occurred at $t = 0$ and $z = 0$ (this being the most likely place for a collision to occur). We can see from Figure 4.6 that we would expect to see an excess of events at ±5 ns and ±10 ns coming from main bunch - satellite bunch interactions and satellite bunch - satellite bunch interactions respectively. However, it is not possible to know directly how big of an effect this potentially is in the exclusive $\gamma_{delayed}$+$\not\!\!E_T$ final state.

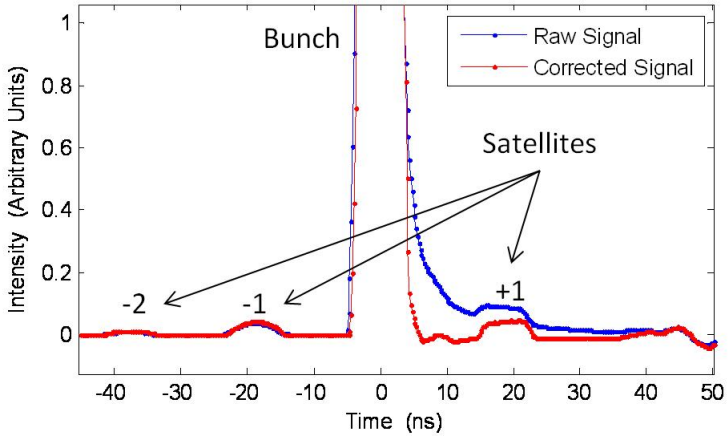

Fig. 4.5. Plot of raw and corrected beam intensity output for the Tevatron proton and satellite bunches taken from [51]. This shows that the satellite bunches both proceed and follow the main bunch by tens of nanoseconds with approximately one percent the intensity of the main bunch.

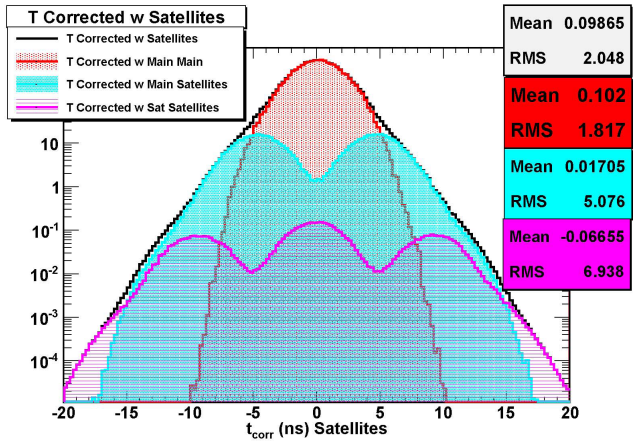

Fig. 4.6. Monte Carlo simulation of where we would expect to see satellite bunch collisions in the t_{corr} distribution.

Therefore, we select for satellite bunch interactions from our data in order to estimate how big of an effect satellite bunches could be in our analysis. We begin by selecting a sample of events that pass our trigger and good run list requirements

as well as have a photon with E_T >30 GeV and $\not\!\!E_T$ >30 GeV in the event. Next we explicitly require that no SpaceTime vertex was reconstructed in the events in order to search a sample where the contribution from main bunch interactions is minimal. Then, in order to ensure that we are not observing other non-collision backgrounds, we veto cosmic ray and beam halo events by using the selections in Tables 4.1 and 4.2. This study was performed on a portion of the total data ($\sim$5 fb^{-1}) used in the final sample, but the results are believed to scale directly with luminosity. Table 4.3 outlines the event selection procedure we follow to estimate satellite bunch interaction.

Event Selection	**Number of Events**
Pass Trigger and Good Run List requriments *(See Table 2.2 and Section 2.4)*	1,023,427
Events with a Photon w/ $E_T^0 > 30$ GeV and $\not\!\!E_T^0 > 30$ GeV *(See Table 2.8 and Section 2.4)*	137,071
No SpaceTime Vertex Reconstructed *See Table 2.10*	74,945
Beam Halo Veto *(See Table 4.2)*	64,898
Cosmic Ray Veto *(See Table 4.1)*	22,268

Table 4.3
Event reduction table for selecting events that potentially contain satellite bunch interactions using only $\sim$5 fb^{-1} of data for this study. Note, since the rate at which sattellite bunches are observed to occur is small and thus no cuts are added in order to veto these events.

Finally, we construct the t_{corr} distribution for the remaining events assuming a inital position and time of $z = 0$, $t = 0$ and plot this in Figure 4.7. As can be seen in Figure 4.7, there is very little activity observed at $\pm$5 and $\pm$10 ns where we would expect to see evidence from satellite bunch interactions. The central peak is believed

to be from main bunch interactions that simply did not reconstruct a SpaceTime Vertex.

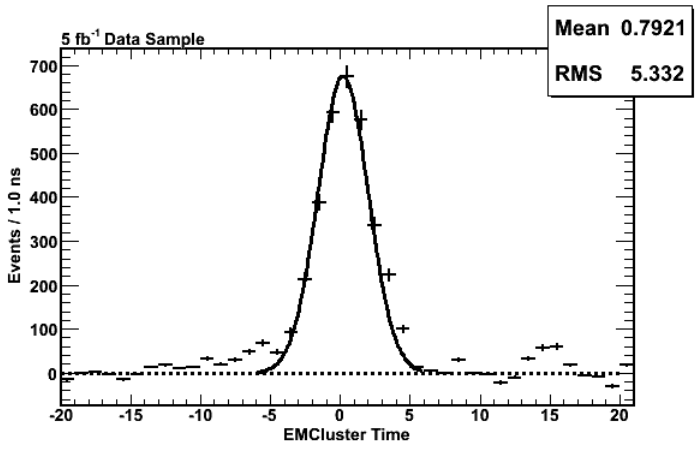

Fig. 4.7. Timing distribution of events selected to look for the presence of satellite bunches in data. We note that we don't see any evidence for satellite bunch interactions being a significant source of backgrounds and thus we do not apply any specific method to reject against them.

Using the scale of the main peak to the event rates observed at five and ten nanoseconds we are able to conclude that the satellite bunch interaction rate is <1% when compared to our collision backgrounds. Moreover, we can see leakage from beam halo in Figure 4.7 at the peak near 18 ns, leading us to believe that beam halo (already established as a small background for the exclusive $\gamma_{delayed}$+$\not\!\!E_T$ final state) is a much larger background then satellite bunches. Using these results as a guide, we do not add any additional cuts to reject against satellite bunch interactions concluding that this is a negligible effect for this analysis.

Having finished a discussion of non-collision based backgrounds for the exclusive $\gamma_{delayed}$+$\not\!\!E_T$ final state we now return to the SM backgrounds and sources of timing biases.

5. STANDARD MODEL BACKGROUNDS AND TIMING BIASES IN THE EXCLUSIVE $\gamma_{DELAYED} + \not\!\!E_T$ FINAL STATE

5.1 Overview

In this chapter we will give an introduction to the Standard Model backgrounds that are present in the exclusive $\gamma_{delayed}+\not\!\!E_T$ final state. We first establish what the backgrounds are and their relative importance to the search performed in this thesis. As we will see, various SM backgrounds timing distribution after the preliminary cuts can give large biased times. In this chapter we study the types of events that give large times and find, in general, three types of events. In addition, we see which types of backgrounds can have large values of the mean time for the wrong vertex and discuss what causes these problems. After describing each problem, we discuss how to remove/mitigate each problem. Once these steps are taken to reduce the amount of bias present in the wrong vertex distribution we then look at the timing distribution of all the known SM backgrounds. We begin this chapter with a brief review of the double Gaussian nature of the corrected time distribution as well as a discussion of how various SM backgrounds may enter our sample.

5.2 Standard Model Backgrounds

In Section 1.4 we defined a common variable used in searching for delayed photons at collider experiments known as the corrected time variable (see Equation 1.7). Furthermore, we showed how the resulting timing distribution for Standard Model processes could be described as the result of a double Gaussian distribution for right and wrong vertex events (see Figure 1.14). The origin of the Gaussian timing distribution can be understood as resulting from the Tevatron beam and timing structure as described in Section 2.4. This description of the corrected timing distribution as a double Gaussian with right and wrong vertex Standard Model background timing

distribution is confirmed when we look at data from $e+\not\!\!E_T$ calibration events in the top of Figure 5.1 (data selection described in Table 3.1). Here we pick the highest ΣP_T vertex as the origin (t_0 and z_0) to calculate the corrected time. Using the matching of the electron track to the vertex we can further divide this distribuiton into the right and wrong vertex Gaussians individually. This is done in order to verify the Gaussian nature of the two distributions. This description clearly models the data very well and thus gives us confidence in the use of a double Gaussian function to describe the corrected time of collision events.

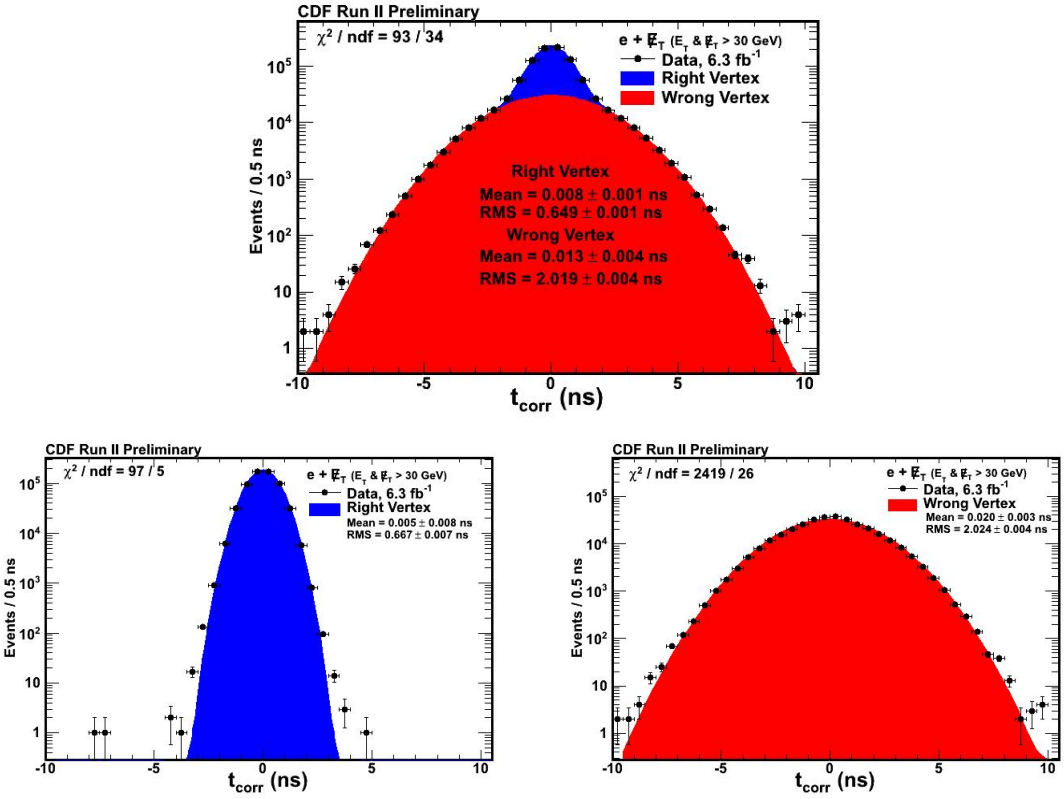

Fig. 5.1. The t_{corr} distribution for a sample of W$\rightarrow e\nu$ data (defined in Section 3.1.1) using the highest ΣP_T vertex (top) as well as the right and wrong vertex Gaussians using the matching of the electron track to the vertex (bottom) verifying the description of the timing distribution as being well described by a double Gaussian distribution. See Table 3.1 for the description of this data sample.

With this basic understanding of the corrected timing variable, we now turn to the various SM processes that may appear as the exclusive γ+$\not\!\!E_T$ final state and thus appear in our final sample. Since the appearance of a single photon plus missing energy with little other activity present in the detector is a very unlikely thing to have coming directly from SM processes, the presence of these backgrounds normally results from a confoundance of various processes taking place in the detector. Broadly speaking what occurs is the various SM processes have a very large production cross-section while the occurrence of the detector or reconstruction failing to properly reconstruct the collisions is a small fraction. This merger of a large number (SM cross-section) times a small number (detector/reconstruction failure) makes a direct estimate of SM backgrounds difficult as elaborated upon below. The summary of the various SM backgrounds present in the exclusive $\gamma_{delayed}$+$\not\!\!E_T$ final state is given in Table 5.1 and we briefly discuss each below.

Standard Model Process
W$\rightarrow$ e$\nu \rightarrow \gamma_{fake} + \not\!\!E_T$
γ+Jet $\rightarrow \gamma$+Jet$_{Lost} \rightarrow \gamma + \not\!\!E_T^{fake}$
Z$\gamma \rightarrow \gamma\nu\nu \rightarrow \gamma + \not\!\!E_T$
W$\rightarrow \mu\nu \rightarrow \gamma_{fake} + \not\!\!E_T$
W$\rightarrow \tau\nu \rightarrow \gamma_{fake} + \not\!\!E_T$
W$\gamma \rightarrow$ lepton$_{lost}$ $\nu\gamma \rightarrow \gamma + \not\!\!E_T$

Table 5.1
Summary of the various Standard Model Backgrounds considered for the exclusive $\gamma_{delayed}$+$\not\!\!E_T$ final state.

1. W$\rightarrow$ e$\nu \rightarrow \gamma_{fake} + \not\!\!E_T$

   The first of the processes considered for the exclusive $\gamma_{delayed}$+$\not\!\!E_T$ final state comes from the SM process where a W boson is produced from the collision and the subsequently decays to an electron (e) and a neutrino (ν). This particular process, having a large cross section at the Tevatron collider [3], makes it one

of the dominant potential sources for backgrounds we expect in this analysis. In order for this process to enter our sample the electron must appear as a photon in the calorimeter (or is commonly referred to as a γ_{fake}). We know from references [46] and [47] that in our data set used in this search (see Table 2.4) we expect to see a W$\rightarrow$ eν cross-section of $\sim$2700 pb with a probability of the electron faking a photon of $\sim$1%. More over, W$\rightarrow e\nu \rightarrow \gamma_{fake}+ \not\!\!E_T$ events often have the wrong vertex selected and do so in ways that further make worse the problems in the exclusive $\gamma_{delayed} + \not\!\!E_T$ final state. Specifically, the ways that electrons fake photons, and the E_T distribution of electrons from W$\rightarrow e\nu \rightarrow \gamma_{fake}+\not\!\!E_T$ events can both bias the mean of the wrong vertex timing distribution as well as significantly change the content of the sample. This is further elaborated on in Section 5.4.1.

2. γ+Jet $\rightarrow \gamma$+Jet$_{Lost} \rightarrow \gamma + \not\!\!E_T^{fake}$

   QCD processes, such as a photon plus a cluster of energy coming from a quark or gluon (γ+Jet), do not have any intrinsic missing transverse energy. However, missing transverse energy can be found in the event via mis-reconstruction or mis-measurement of the energy contained in the reconstructed jet or photon. One such example of how this can occur is when energy from the jet is deposited in an un-instrumented region of the detector or is produced at large η and travels down the beam pipe. While the fraction of QCD events with a mis-measurement of$\not\!\!E_T$ as high as 45 GeV is very small (<5%), the total QCD cross section is very large ($\mathcal{O}$(1000's pb)) [3], thus making this another potentially large background to this analysis. While the rate at which γ+Jet$\rightarrow \gamma+ \not\!\!E_T$ events pass our analysis selection is small, it can be a significant background to exclusive $\gamma_{delayed} + \not\!\!E_T$ because the topology of the events that do pass. In order to be present in our sample it is necessary to have a high E_T photon and large missing energy coming from γ+Jet which also causes the vertex to be

mis-measured and thus bias us towards larger t_{corr}. This process is presented in greater detail in Section 5.4.3.

3. $Z\gamma \rightarrow \gamma\nu\nu \rightarrow \gamma + \not\!\!E_T$

   An irreducible background in the exclusive $\gamma_{delayed}+\not\!\!E_T$ final state comes from the production of a Z boson along with initial state radiation. The Z boson consequently decays to a pair of neutrinos that escape the detector in the form of missing energy and we thus end up with $\gamma+ \not\!\!E_T$ final state. While the decay rate of the Z boson to pairs of neutrinos (which we can't detect and thus show up as $\not\!\!E_T$) is much higher than to charged leptons (which we are able to veto with a high efficiency), the overall Z boson production rate is small and thus makes this background of little concern. Furthermore, the relatively small wrong vertex mean, as will be discussed further in Section 5.5, observed in Monte Carlo further diminishes the importance of this otherwise nondeductible background.

4. Other W Sources

   The last major sources of backgrounds in the exclusive $\gamma_{delayed}+\not\!\!E_T$ final state comprise the other various ways the W boson may decay and how the subsequent lepton may fake a photon or become lost. Two such examples of this decay are $W\rightarrow \mu\nu \rightarrow \gamma_{fake} + \not\!\!E_T$ and $W\rightarrow \tau\nu \rightarrow \gamma_{fake} + \not\!\!E_T$. In these examples the muon and the tau would fake a photon in the calorimeter and thus be misidentified as $\gamma+ \not\!\!E_T$. While the production cross-section of these processes is known to be relatively large ($\sim$1000 pb [46]), the likelihood of these leptons faking a photon is known to be very small ($< 1\%$ [66]) in the CDF detector. Therefore we do not devote any specific cuts to rejecting these processes. The last of the W boson processes we consider comes from the production of a W boson with initial state radiation where the W boson decays to a lepton plus a neutrino and the lepton becomes "lost" in the detector giving us $\gamma+\not\!\!E_T$ final

state. This decay is dealt with in part in Section 5.4.2 in addition we note that the tracking efficiency in the CDF detector is known to be $> 95\%$ [56], thus making this a low rate background in this analysis.

Having finished an overview of the individual SM backgrounds most relevant to the exclusive $\gamma_{delayed} + \not\!\!E_T$ final state, we come back to the corrected time distribution for these backgrounds. We begin by showing how various pathologies and biases present in the exclusive $\gamma_{delayed}+\not\!\!E_T$ final state lead us to reconsider the underlying assumption that the wrong vertex mean will be centered at $t_{corr} = 0.0$ ns, as was the case in the preliminary study performed in 2008.

5.3 Wrong Vertex Mean Shifts and Pathological Event Reconstruction

Figure 5.2 shows the expectation for the background timing distribution as they were understood in 2008 when the preliminary result mentioned in Section 1.5 was performed. Clearly, it appears that this timing distribution is symmetric about t_{corr} = 0 ns and thus seems that it should be possible to predict the number of events in the signal region (2 ns to 7 ns) from counting the number of events in the control region (-7 ns to -2 ns). Any deviation from this would appear as an excess above the prediction and thus provide evidence for new physics. However, as mentioned previously, this simplifying assumption turns out not to hold true in the exclusive $\gamma_{delayed}+\not\!\!E_T$ final state. As will be discussed in the next section, the mean of the wrong vertex can actually vary significantly from $t_{corr} = 0$ ns for a variety of reasons. Despite this fact, the double Gaussian nature of the timing distribution continues to hold true. This fact offers an opportunity to still be able to make a data driven prediction of the number of events in the signal region from SM processes provided one can measure the mean of the wrong vertex.

As mentioned in Section 1.4, one of the dominant SM backgrounds in the exclusive $\gamma_{delayed}+\not\!\!E_T$ final state is the choice of an incorrect vertex. This background is

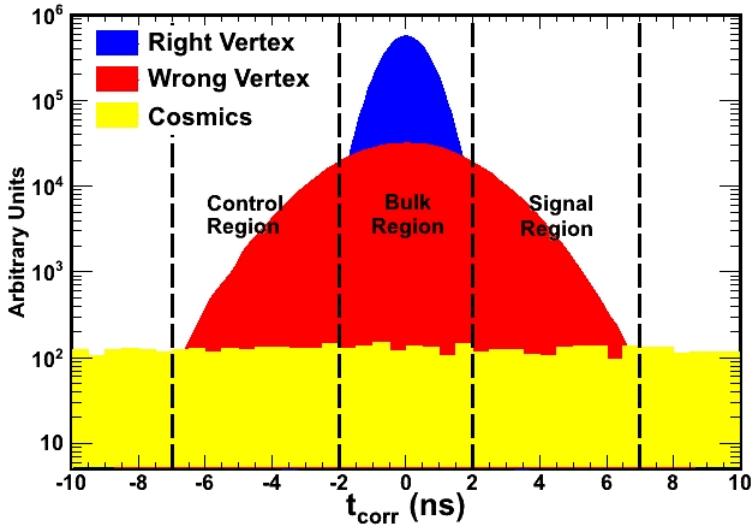

Fig. 5.2. Corrected time distribution showing our previous understanding of what the right vertex, wrong vertex, and cosmic ray timing distributions would be for all Standard Model and non-collision sources. The apparent symmetry of the corrected timing distribution about $t_{corr} = 0$ ns is what previously allowed us to assume that we could predict the number of events from SM source in signal region from the control region. However, we know now that for various reasons outline in Section 5.3 this assumption is incorrect.

a problem irrespective of the production source of the photon candidate and can have a significant impact on the timing distribution. More over, in the exclusive $\gamma_{delayed}$+$\not\!\!E_T$ final state there is explicitly a lack of other final state particles, thus there are fewer tracks present in the event to produce a vertex. This means that for the SM backgrounds the collision which produced the photon is both less likely to have its vertex reconstructed and less likely to be selected as the highest ΣP_T vertex used in the timing measurement and photon identification. The main impacts of selecting a wrong vertex summarized here.

- Incorrect selection of the vertex causes an incorrect $\sin\theta$ to be assigned to the measurement of the photon's E_T. This can cause events to be incorrectly

included in our sample, as described in Section 5.4.1. This same effect can also cause a mis-measured/biased timing distribution. This timing mismeasurement can lead to events migrating into the signal region (2 ns to 7 ns) and thus 'fake' a signal.

- Incorrect selection of the vertex also causes the standard photon identification variables used to reject sources which "fake" a photon in the detector to become less powerful. Specifically, identifications like track isolation currently require that the tracks being considered are within 5 cm of the primary vertex. Since selection of the correct vertex becomes a problem in the exclusive $\gamma_{delayed}$+$\not\!\!E_T$ final state, in becomes necessary to employ new 'fake' photon rejection. This issue and its subsequent remedy will be explored in Section 5.4.2.

- The incorrect selection of a vertex also causes pathological events to enter our sample that should not. Most notably, events which produce a photon but occur at large $|z$ and thus do not have their vertex reconstructed may have an errant vertex near the center of the detector assigned to them. This both causes very pathological events to enter as well as have an incorrect time of flight assigned to them. This process is described in more detail in Section 5.4.3.

By way of example of how the selection of a wrong vertex can exasperate problems in estimating the mean of the wrong vertex, we examine W$\rightarrow e\nu \rightarrow \gamma_{fake}$+$\not\!\!E_T$ events. These events often have the wrong vertex selected and do so in ways that further make worse the problems in the exclusive $\gamma_{delayed}$ + $\not\!\!E_T$ final state. Specifically, the ways that electrons fake photons, and the E_T distribution of electrons from W$\rightarrow e\nu \rightarrow \gamma_{fake}$+ $\not\!\!E_T$ events can both bias the mean of the wrong vertex timing distribution as well as significantly change the content of the sample. These effects are discussed in greater detail in Section 5.4.1.

In addition to the effects on the E_T and t_{corr} distribution, an electron is more likely to 'fake' a photon if its path length from its collision point to the calorimeter face is longer. Said differently, the same effects that contribute to the selection of a wrong vertex also contribute to an electron 'faking' a photon. When these effects are combined they can lead to large wrong vertex mean timing shifts and cause as much as twice the number of events to appear in the signal region as appear in the control region. Therefore, the development of a new $e \rightarrow \gamma_{fake}$ veto algorithm was necessary and is detailed in Section 5.4.2.

Finally, the last of the important reconstruction pathologies that may effect the timing distribution comes from events originating from large $|z|$ location. If there is a collision that occurs at $|z|$ >60 cm which creates a real photon that is then observed in the central calorimeter. this vertex will not be reconstructed by the SpaceTime vertexing algorithm. This is due to the fact that we explicitly require that the SpaceTime verticies used in the exclusive $\gamma + \not\!\!E_T$ analysis come from $|z|$ <60 cm in order to have a timing measurement associated with the vertex. Moreover, if there happens to be a min-bias event near the center of the detector at the same time of the collision at $|z|$ >60 cm a wrong vertex will be assigned to the event. This is most easily seen in γ + jet events where in order to enter the exclusive $\gamma + \not\!\!E_T$ analysis the event would have to have this unique topology. Thus, we develop a simple veto to remove events that appear to have evidence of a collision occurring at large z as is described in Section 5.4.3.

5.4 Rejecting Backgrounds with Large Times

Understanding the causes of the shifts in the wrong vertex mean as well as the dominant pathological event reconstruction issues we now lay out the basic strategy to performing a search in the exclusive $\gamma_{delayed} + \not\!\!E_T$ final state.

1 Minimize Geometric and Kinematic Biases:

Geometric and kinematic biases that come from the selection of an incorrect vertex lead to a migration of events into our sample with a large timing bias. In order to reduce the impact of this migration of events we will redefine our E_T definition. In doing so we will take advantage of the fact that on average most collisions occur at $z = 0$ and thus in defining E_T relative to fixed position reduce the amount of bias in the wrong vertex timing distribution.

2 Veto $e \to \gamma_{fake}$ Sources:

Since the typical tools for $e \to \gamma_{fake}$ are found to be not as powerful in the exclusive $\gamma_{delayed}$+$\not\!\!E_T$ analysis, we have developed a new method where by we can reject 67% of events coming from W$\to e\nu \to \gamma_{fake}$+ $\not\!\!E_T$ with a 95% efficiency for real photons. This is detailed in Section 5.4.2.

3 Veto Events from Large z:

Finally, since the timing bias from wrong vertex events can be especially large if the true collision occurred at $|z|$ >60 cm we reject events that have evidence of a collision occurring at large $|z|$ position. This will help minimize the wrong vertex mean bias as well as reduce the most pathologically mis-reconstructed events. This veto is detailed in Section 5.4.3.

5.4.1 Minimizing the Correlations Between Geometric and Kinematic Biases

As we described in Section 5.3, selection of a wrong vertex event both biases the mean of the wrong vertex timing distribution as well as significantly changes the content of the sample. This change of the content of the sample occurs because the geometry of the events effects the kinematics, and vice versa as illustrated in Figure 5.3. In this section we address the issue of how the geometric effects which cause $E_T^{measured} > E_T^{true}$ when we select the highest ΣP_T vertex to calculate E_T can cause $t_{corr}^{measured} > t_{corr}^{true}$.

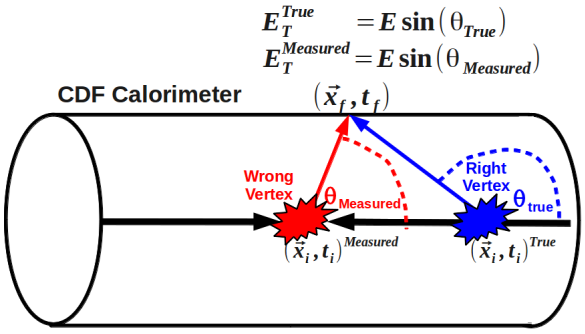

Fig. 5.3. A schematic drawing of W$\rightarrow e\nu \rightarrow \gamma_{fake}+ \not\!\!E_T$ where we have selected a wrong vertex. For this example, the selection of the wrong vertex leads to an $\theta_{measured} > \theta_{true}$ where θ_{true} is the real angle the photon/electron came from. This results in a larger measured value for E_T ($E_T^{Measured} > E_T^{true}$), thus preferentially causing us to select these events. Furthermore, the path length calculated for the wrong vertex is shorter than the true path length of the photon/electron resulting in an apparent longer time of flight and thus $t_{corr}^{measured} > t_{corr}^{true}$ causing an overall shift in the mean.

For photons we define E_T as $E_T = Esin\theta$, where E is measured from the calorimeter, and θ is measured using the CES position in the calorimeter and the presumed vertex position in z. Consider the configuration in Figure 5.3 where the vertexing algorithm does not select the correct collision point either because it is not reconstructed or because a higher ΣP_T vertex from a min-bias interaction happens to exist. In this case we have $\theta_{measured} > \theta_{true}$, so that $|\vec{x}_f - \vec{x}_{measured}| < |\vec{x}_f - \vec{x}_{true}|$, resulting in $t_{corr}^{measured} > t_{corr}^{true}$ (ignoring the contribution from t_i and t_{WV}).

At the same time, since $\theta_{measured} > \theta_{true}$, we find $E_T^{measured} > E_T^{true}$. This implies that events that have a positively shifted $t_{corr}^{measured}$ will also have a larger $E_T^{measured}$. This fact has a remarkable consequence. Namely, this means that events that have E_T^{true} slightly less than 45 GeV and should not be in our sample of events will have an $E_T^{measured} > 45$ GeV and will enter the sample because we chose the wrong vertex. Since these events will also have a timing bias, this means that all the events that

enter the sample (i.e., that pass the cuts but shouldn't' have) will all have larger than expected times.

The converse is also true: a configuration with a mis-measured vertex, where $\theta_{measured} < \theta_{true}$, would lead to a lower measured value of t_{corr} and lower measured value of E_T. Specifcally, events that have E_T^{true} slightly more than 45 GeV and should remain in our sample of events will have an $E_T^{measured} < 45$ GeV and will leave the sample because of the choice of the wrong vertex. These events have a negitive t_{corr} timing bias, however go unobserved since they leave the sample. The bottom line of all this is that misidentification of vertices leads to values of t_{corr} and E_T being shifted in the same positively biased direction.

This migration of E_T values due to the incorrect vertex selection can also significantly affect the composition of the events that ultimately end up in a sample. This is again readily seen by looking at W$\rightarrow e\nu \rightarrow \gamma_{fake}+ \not\!\!E_T$ events in Figure 5.4. A typical analysis requires $E_T^{measured} > E_T^{cut}$ where E_T^{cut} is the value which if the object has less then this E_T we do not consider the event as part of our sample. This causes events that have $E_T^{true} < E_T^{cut} < E_T^{measured}$ to enter the sample and as we discussed before these events also have $t_{corr}^{measured} > t_{corr}^{true}$. That is to say, events that just pass the E_T selection incorrectly due $E_T^{measured} > E_T^{cut}$ will enter the sample and be biased toward larger times. At the same time, the events with $E_T^{true} > E_T^{cut} > E_T^{measured}$ will leave the sample. These events exiting our sample had $t_{corr}^{measured} < t_{corr}^{true}$ bias towards smaller times. The net effect is that a positive timing bias is left as part of the sample we select.

Said differently, events that migrate into the sample have large times and events that leave the sample have smaller times. While this might not be a big effect in principle, the number of events entering and leaving around an E_T cut is frequently asymmetric as demonstrated in Figure 5.4 which shows a sample of events selected based on the Table 2.12 for the exclusive $\gamma+\not\!\!E_T$ presample. Since there are more events with small E_T^{true} than large E_T^{true} , more events events make it past the value

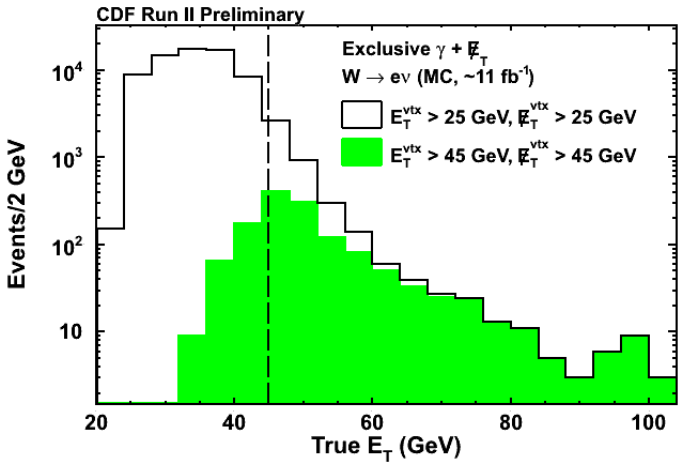

Fig. 5.4. The E_T^{True} distribution for a sample of W$\rightarrow e\nu$ MC events selected with Table 2.12 for the exclusive γ+$\not\!\!E_T$ presample. The unshaded histogram is the true E_T for electrons that fake photons, the solid histogram (shown in green) is the true E_T for electrons that were identified as photons, and passed the $E_{Tmeasured}$ >45 GeV cut. The plot shows more events entering the sample than leaving it.

of E_T^{cut}, resulting in a higher average value of t_{corr} when the wrong vertex is selected. At 45 GeV (where our E_T selection resides) the slope of the E_T^{true} distribution is very steep around this boundary, so the migration effect is very significant.

In order to mitigate this effect, we exploit the fact that at CDF most collisions occur on average at $z = 0$. Thus, if we instead define E_T for the photons reconstructed in our events from $z = 0$ instead of from the highest ΣP_T vertex we will never be exactly right on an event-by-event bases, but be more generally right on average. The effect of this is that fewer events will be "promoted" into our sample by having $E_T^{measured} > E_T^{true}$ (on average) as well as fewer events being "demoted" out of our sample with $E_T^{measured} < E_T^{true}$.

Similarly this means that fewer events with $t_{corr}^{measured} > t_{corr}^{true}$ will be entering our sample on average as well as fewer events with $t_{corr}^{measured} < t_{corr}^{true}$ leaving our sample. The net result is the kinematic bias that was present before as a result

of this definition of E_T is diminished. This can be seen in Figure 5.5 where for a sample of exclusive e+$\not\!\!E_T$ events, defined in Table 2.11, have been selected using the two definitions for E_T and $\not\!\!E_T$. In order to demonstrate that our understanding is complete we compare highest ΣP_T vertex with z=0 for data and MC.

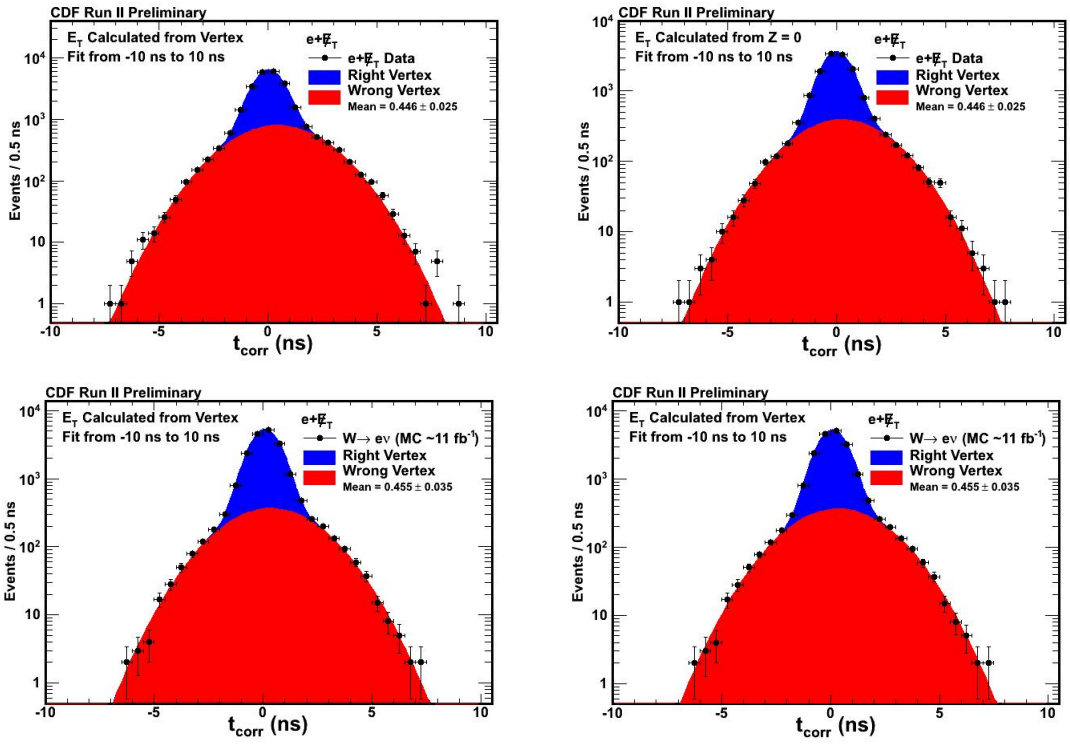

Fig. 5.5. Large t_{corr} timing bias for W$\rightarrow e\nu$ electrons in data and MC when calculated from the Highest ΣP_T vertex and $z = 0$ showing that you can minimize this effect by simply calculating E_T and $\not\!\!E_T$ from $z = 0$.

On the left hand side of Figure 5.5 we see that in both data and Monte Carlo wrong vertex had a mean of ~0.4 ns when we defined E_T relative to the highest ΣP_T vertex. On the right hand side of Figure 5.5 the resulting wrong vertex mean is only ~0.2 ns when we defined E_T and $\not\!\!E_T$ relative to $z = 0$. The remarkable agreement between data and MC gives us great confidence that the understanding of the source of this bias is well modeled and that a large portion of the bias present in the wrong

vertex distribution for SM processes in the exclusive $\gamma_{delayed}$+$\not\!\!E_T$ final state can be reduced by simply redefining the E_T and $\not\!\!E_T$ variables relative to $z = 0$ cm. It is also worth noting at this point that the timing distribution for both data and MC is well described by a double Gaussian distribution.

5.4.2 Rejecting Events from $e \to \gamma_{fake}$ Sources

Since W$\to e\nu \to \gamma_{fake}+ \not\!\!E_T$ process is a considerable background to any search with a $\gamma+ \not\!\!E_T$ final state it us useful to understand why this background gives a large timing bias and what causes this background to occur so we can reject it more effectively. The first point is that, in the exclusive $\gamma_{delayed}$+$\not\!\!E_T$ final state, the lack of other activity in the detector required means the primary vertex is both less likely to be reconstructed and less likely to be the highest ΣP_T vertex in the event. Additionally, as discussed in Section 5.3, the same geometric effects that lead to a positive time bias are also the same issues that contribute electrons to fake photons. Namely an electron with a longer path length from the collision point to the calorimeter is more likely to 'fake' a photon. A longer path length implies $|\vec{x}_f - \vec{x}_{measured}| < |\vec{x}_f - \vec{x}_{true}|$ which also implies $E_T^{measured} > E_T^{true}$ and $t_{corr}^{measured} > t_{corr}^{true}$ and thus also is subject to the same bias arguments just given.

To reduce the fraction of the time an electron fakes a photon we first note that the dominant way that electrons fake photons is when there is a hard bremsstrahlung interaction in the detector material. As an electron travels through the detector material, a hard interaction can cause it to lose a large fraction of its energy to a photon. The electron's trajectory is severely affected by the energy and momentum loss; it may either leave a much lower energy deposition in a calorimeter or be swept away completely by the magnetic field of the solenoid. The bulk of the energy of the photon candidate in the calorimeter is thus due to the brem'd photon.

We find that when we select the location of the largest transfer of energy to a single photon we can get a sense of what is going on [78]. We find that 93% of the

time the electron gives more than 50% of its energy to a single photon. The remaining 7% are most likely tracking failures. Thus, we focus on hard-brem interactions as the primary cause of the $e \rightarrow \gamma_{fake}$ candidates. A simple requirement of fraction of the energy lost to be greater than 50% allows us to map out the locations of the hard bremsstrahlung interaction inside the detector. This is shown on the in Figure 5.6. Note that this figure shows clearly the material inside the detector, an "x-ray" of sorts; showing the bulk of the bremsstrahlung interactions occur where the SVX detector and its support structure reside. The fact that so many of the electrons undergo bremsstrahlung early allows us to understand why the conventional rejection methods fail, namely there is not much detector information available to reconstruct the track associated with the electron.

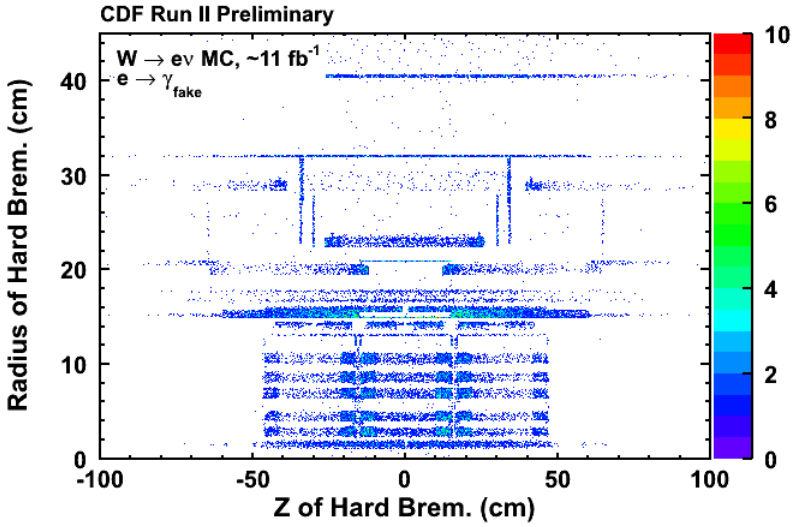

Fig. 5.6. A 2-D histogram showing where inside the detector electrons converted to photons via a hard bremsstrahlung interaction. In these interactions the outgoing photon takes with it $> 50\%$ of the electron's initial energy.

This can be seen even more clearly in Figure 5.7. For a sample of W$\rightarrow e\nu \rightarrow \gamma_{fake}+\not\!\!E_T$ MC events where we require the photon to have come from an interaction

in the detector where $> 50\%$ of the electrons energy was given to a single photon, you can see where this interaction occured. Again, the majority of events are seen to have had a bremsstrahlung interaction near the SVX detector.

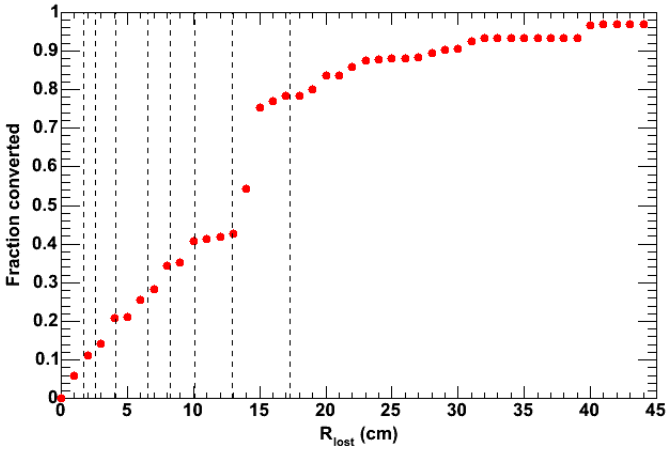

Fig. 5.7. An integral plot of the fraction of events where electrons coming from W$\rightarrow e\nu \rightarrow \gamma_{fake}+\not\!\!E_T$ Monte Carlo bremm'd as a result of interaction with detector material versus the radius. Note, that the majority of events are seen to brem inside the silicon detector and the port cards (denoted with the dashed lines).

A schematic drawing of this process of how these $e \rightarrow \gamma_{fake}$ events from hard bremsstrahlung interactions appear in the detector is shown in Figure 5.8. As an electron travels through the detector material, the hard interaction can cause it to lose a large fraction of its energy to a photon.

We can now see why these photon candidates are not rejected by the N3D track requirement of the standard photon ID cuts given in Table 2.8. The post-brem electron loses its initial momentum and is left with low P_T , so the track is significantly curved away from the final location of the photon candidate in the calorimeter. Since the ϕ position of the low P_T track at the face of the calorimeter is far from the reconstructed ϕ position of the photon candidate, it is unlikely for the track to be "matched" to the photon candidate by the standard photon reconstruction

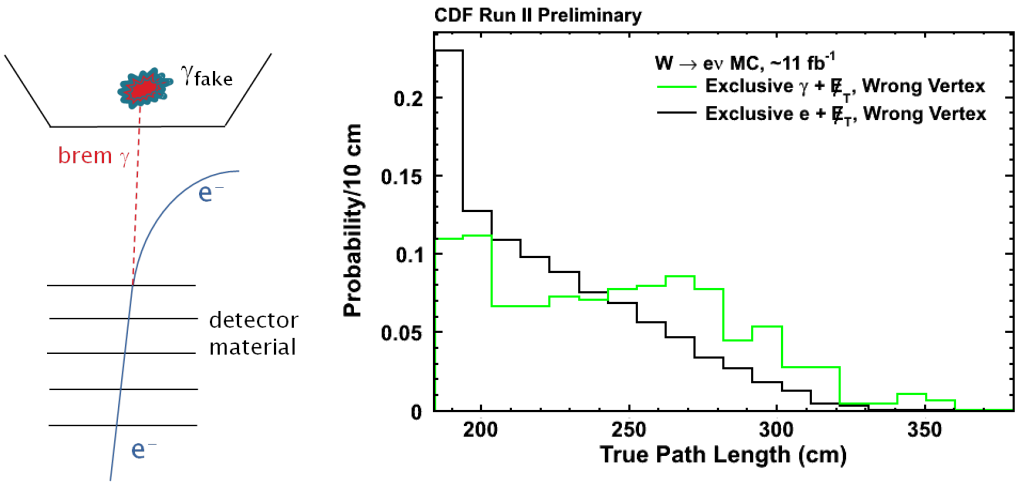

Fig. 5.8. (LHS)A schematic representation of an electron interacting with the detector material and having a hard bremsstrahlung interaction. After the interaction the electron curves off because of its resulting lower energy and thus its trajectory becomes highly curved in the magnetic field. It is important to note that both before and after the bremsstrahlung the trajectory can be reconstructed as a single low P_T track (RHS) The true path length for electrons mis-identified as photons, selected with Table 2.12 for the exclusive γ+$\not\!\!E_T$ presample, showing that these events tend to have larger path lengths than correctly identified electrons.

algorithms [66]. We find that a low P_T brem'd track can end up at least three towers away from the EM cluster [78]. While the standard methods are very effective for rejecting electrons in general, since the charged track is readily identified and rejected, this procedure is not helpful in this particular case.

Since the standard methods leave a large number of fake events in our sample, and the remaining ones have a large time bias, we have developed a new method that takes advantage of the observation that the majority of the $e \rightarrow \gamma_{fake}$ candidates are due to electrons which interact with detector material and brem. This method considers all reconstructed tracks in the event and matches likely candidate tracks to the photon candidates in order to veto these events. We begin by defining the

track quality cuts considered for tracks that can veto a photon candidate in Table 5.2. We note that this track definition is a 'looser' definition then the tracks defined in Table 2.6 for 'good' timing tracks and high P_T isolated tracks. The reason for this is we expect these tracks to only be present early in the detector and thus be of lower quality, therefore we use this looser definition in order to maximize the likelihood of finding this short track.

$\lvert\eta\rvert$	≤ 20
NAxialSeg *Number of COT Axial Segments with hits*	≥ 2
NStereoSeg *Number of COT Stereo Segments with hits*	≥ 2
$\lvert Z\rvert$ *Z Position of the track*	≤ 150

Table 5.2
Track identification variables for use in $e \to \gamma_{fake}$ veto

We next define the matching variable ΔR_{Pull} to determine if the track is matched to the photon candidate as:

$$\Delta R_{Pull} = \sqrt{\Delta\phi^2_{Pull} + \Delta\eta^2_{Pull}}. \tag{5.1}$$

$\Delta\phi^2_{Pull}$ and $\Delta\eta^2_{Pull}$ are defined in order to account for the detector response as:

$$\Delta\phi_{Pull} = \frac{\Delta\phi}{\sigma_\phi} \tag{5.2}$$

where σ_ϕ is measured to be $\sigma_\phi = 8.1 \cdot 10^{-2}$ and

$$\Delta\eta_{Pull} = \frac{\Delta\eta}{\sigma_\eta} \tag{5.3}$$

and $\sigma_\eta = 6.3 \cdot 10^{-3}$ [78]. The top of Figure 5.9 shows the distribution of the closest track to the photon candidate in $\Delta\phi_{Pull}$ and $\Delta\eta_{Pull}$ as being very symmetric for a

sample of W$\rightarrow e\nu \rightarrow \gamma_{fake}+\not\!\!E_T$ events . This allows us to draw a circle ΔR_{Pull} in order to veto events that are likely to have come from $e \rightarrow \gamma_{Fake}$ processes. The bottom of Figure 5.9 shows what the $\Delta\eta_{Pull}$ variable looks like for a sample of W$\rightarrow e\nu \rightarrow \gamma_{fake}+\not\!\!E_T$ (shown in Black) and real photons coming from $Z\gamma \rightarrow \nu\nu\gamma \rightarrow \gamma+\not\!\!E_T$ events (shown in red) where both samples come from the exclusive $\gamma+\not\!\!E_T$ presample defined in Table 2.12.

We have chosed to place a cut at ΔR_{Pull} >5 in order to veto $e \rightarrow \gamma_{fake}$ events, as shown in Figure 5.10, as this cut is 95% efficient for real photons with a rejection power of 73% for $e \rightarrow \gamma_{fake}$. It is important to note, as shown in Figure 5.11, that this cut does not reduce the shifted mean of the wrong vertex distribution for $e \rightarrow \gamma_{fake}$ events. However it does reduce the overall rate at which they appear in our final sample. This reduces the overall importance of this background and makes us less sensitive to the wrong vertex mean shift.

5.4.3 Rejecting Events from Large $Z_{Collision}$ Sources

The final source of timing biases we address here comes from wrong vertex events that occur at large $|z|$ collision position. These events enter the sample in the case when a collision occurs at $|z|$ >60 cm and produces a photon candidate that is then found in the calorimeter. Since verticies at $|z|$ >60 cm will not be selected as the highest ΣP_T vertex in the exclusive $\gamma_{delayed}+\not\!\!E_T$ analysis, if a min-bias collision happens to occur at the center of the detector we may mis-assign the vertex and thus incorrectly calculate the corrected time. Since these events will have a larger true time-of-flight than what is assigned to them they can have signifcantly biased t_{corr}.

This situation is most easily seen in γ + Jet events selected using the cuts from Table 2.12 which defines the exclusive $\gamma_{delayed}+\not\!\!E_T$ presample. In order for these QCD based events to enter the exclusive $\gamma+\not\!\!E_T$ they must have a unique topology. The timing bias from γ + Jet events coming from large z sources is rooted in the fact

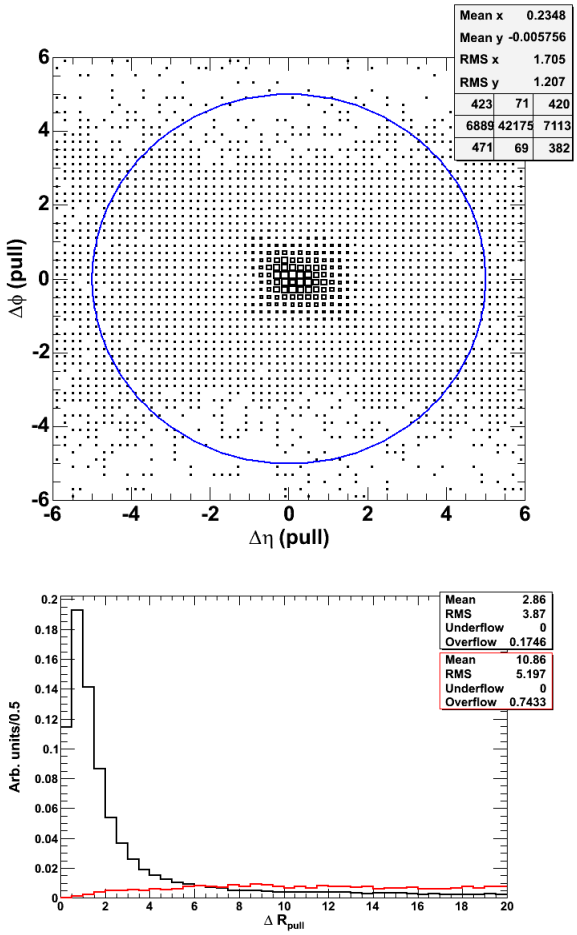

Fig. 5.9. (Top) Dividing $\Delta\eta$ and $\Delta\phi$ which have been normalized to their detector response ("pull") shows that the closest track to the photon is symmetric in $\Delta\eta$-$\Delta\phi$ space and a radius $\Delta R_{pull} = 5$ (shown by the blue line) is the cut value used to reject $e \to \gamma_{fake}$. (Bottom) The ΔR_{pull} for a control sample of MC $Z\gamma \to \nu\nu\gamma \to \gamma + \not{E}_T$ (Red) and W$\to e\nu \to \gamma_{fake} + \not{E}_T$ (Black) showing the rejection power of this cut. Note, both samples are normalized to each other.

that $|\vec{x}_f - \vec{x}_{measured}| < |\vec{x}_f - \vec{x}_{true}|$ and thus we incorrectly assign a time-of-flight that is too small.

Furthermore, in Figure 5.12 we can see that the z collision for γ + Jet events extends far beyond $|z| = 60$ cm. Therefore we veto that have evidence that they may have collision activity out at large $|z|$ position. Specifically, to be more efficient at

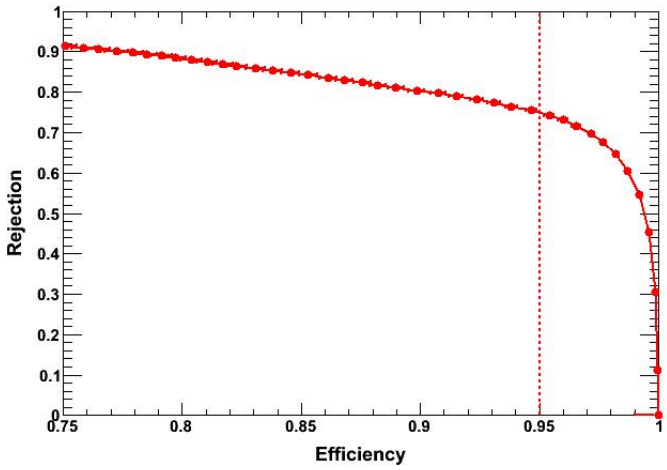

Fig. 5.10. A cut at $\Delta R_{Pull} = 5$ (red dashed line) results in approximately 95% efficiency of MC $Z\gamma \to \nu\nu\gamma \to \gamma + \not{E}_T$ and 73% rejection of $e \to \gamma_{fake}$.

rejecting these vertices, we use CDF's standard vertex algorithm described in greater detail in reference [79]. This algorthim searches for vertices out to $|z| = 150$ cm and thus allows us a handle on events that have evidence of activity at large collision z. If we find a standard vertex with three or more tracks at $|z|$ >60 cm we veto this event as likely having a collision at large z position.

The effect of this veto can be seen in Figure 5.13 where we show the timing distribution of γ + Jet events using the cuts from Table 2.12 which defines the exclusive $\gamma_{delayed}+\not{E}_T$ presample. We then apply the large z vertex veto to the sample and show that the mean of the wrong vertex goes from 0.38 ns to 0.18 ns, greatly reducing the timing bias present in this sample.

More over, we show that the large $|z|$ veto does not effect the timing distribution for a sample of events which originate inside the $|z|$ <60 cm area. To illustrate this we select a sample of Zγ MC using the cuts defined in Table 2.12 for the exclusive $\gamma_{delayed}+\not{E}_T$ presample. In Figure 5.14 we show the t_{corr} distribution for the Zγ events

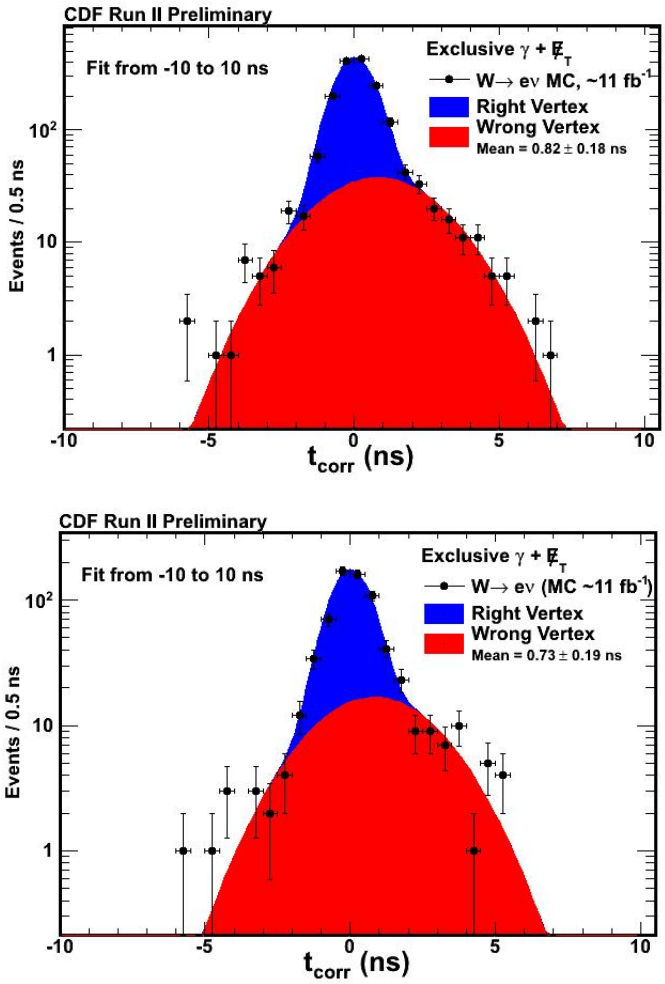

Fig. 5.11. W→ $e\nu$ MC events, selected using the exclusive γ+$\not\!\!E_T$ presample defined in Table 2.12, before (Top) and after (Bottom) the application of the $\Delta R_{Pull} = 5$ cut. The application of this cut does not reduce the wrong vertex timing bias but does reduce the overall rate at which this background appears in our final sample.

before and after the application the large $|z|$ veto showing very little effect to the timing distribution, as expected.

We estimate the efficiency of the large $|z|$ veto by applying it to a set of cosmic ray events selected using Table 2.12 and looking at the rate of cosmics in the region 20 ns - 80 ns before and after the large $|z|$ veto shown in Figure 5.15. From this

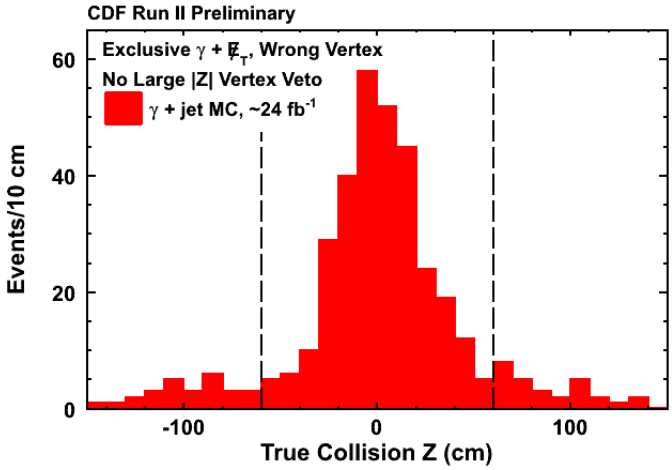

Fig. 5.12. The z distribution of γ+Jet events selected using Table 2.12 which defines the exclusive $\gamma_{delayed}$+$\not\!\!E_T$ presample. This distribution shows the timing bias in these events is caused by events which originate at large $|z|$ >60 cm.

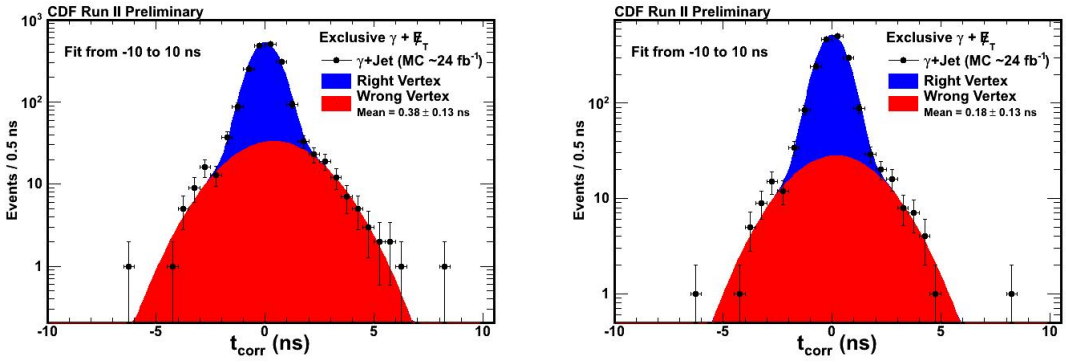

Fig. 5.13. (Left) γ+Jet events selected using Table 2.12 and (Right) the same sample after applying the large z veto showing the wrong vertex mean becomes much less biased.

sample we conservatively estimate that the large $|z|$ veto is >95% efficient for real photons and collisions coming from $|z|$ <60 cm while, as can be easily seen in Figure 5.13, greatly reducing the timing bias coming from large $|z|$ collisions.

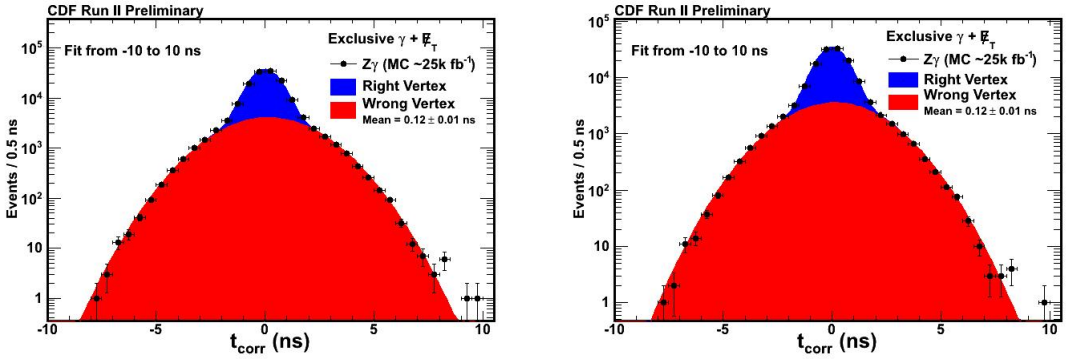

Fig. 5.14. (Left)Zγ events selected using Table 2.12 and (Right) the same sample after applying the large z veto showing very little effect in the timing distribution for events which originate from within $|z|$ <60 cm.

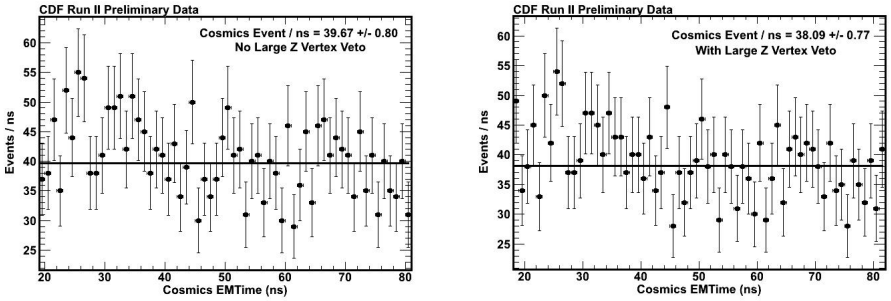

Fig. 5.15. (Left) Cosmic ray events selected using Table 2.12 and looking in the timing region from 20 ns - 80 ns and (Right) the same sample after applying the large z veto the rate of cosmic rays is effectively not effected, as expected, by the large z veto.

Table 5.3 we summarize the set of cuts that will now define the exclusive $\gamma_{delayed}$+ $\not\!\!E_T$ final state. With the final event selection established for the exclusive $\gamma_{delayed}$ + $\not\!\!E_T$ final state we now turn to examine the timing distribution for our MC samples.

Pass Trigger and Photon Good Run List *(See Table 2.2 and Section 2.4)*
Pass Tight Photon requirements w/ $E_T^0 >$ 45 GeV and $\not\!\!E_T^0 >$ 45 GeV *(See Table 2.8 and Section 2.4)*
Pass Beam Halo Rejection *(See Table 4.2)*
Pass Cosmics Rejection *(See Table 4.1)*
Pass Track Veto for Tracks with $P_T >$ 10 GeV *(See Table 2.4)*
Pass Jet Veto for Jets with $E_T^0 >$ 15 GeV *(See Table 2.5)*
Pass Large $\|Z\|$ Vertex Veto *(See Section 5.4.3)*
Pass $e \to \gamma_{fake}$ Veto *(See Table 5.2 and Section 5.4.2)*
Require a Good SpaceTime Vertex *(See Table 2.10)*

Table 5.3
Exclusive $\gamma_{delayed} + \not\!\!E_T$ complete table of event selection requirements.

5.5 Timing Distributions for the Standard Model Backgrounds

Now that we have completed our discussion of the mechanisms for the production of SM events with large times, and methods for rejecting and/or minimizing the bias, we now consider the SM backgrounds as well as our electron control samples after all the cuts. The final set of requirements are shown in Table 5.3. We show below that the timing distribution for all the known SM backgrounds as well as our exclusive e+$\not\!\!E_T$ control sample is well described by a double Gaussian. In Table 5.4 we summarize the resulting corrected time distribution for the six MC samples considered as backgrounds to the exclusive $\gamma_{delayed}$+$\not\!\!E_T$ search. Specifically we list the resulting wrong vertex mean obtained by performing a double Gaussian fit over the timing range -10 ns to 10 ns.

Sample	Wrong Vertex Mean (ns)
W→ eν MC	0.73 ± 0.19 ns
γ+Jet MC	0.18 ± 0.13 ns
Zγ MC	0.12 ± 0.01 ns
W→ $\mu\nu$ MC	0.29 ± 0.26 ns
W→ $\tau\nu$ MC	0.43 ± 0.26 ns
Wγ MC	0.14 ± 0.07 ns
e+$\not\!\!E_T$ Data	0.17 ± 0.05 ns
e+$\not\!\!E_T$ Data (E_T&$\not\!\!E_T > 30$ GeV)	0.04 ± 0.01 ns

Table 5.4

Summary of Monte Carlo backgrounds and e+$\not\!\!E_T$ control sample and their wrong vertex mean. The sample of events is selected after applying the exclusive $\gamma_{delayed}$+$\not\!\!E_T$ event selection requirements defined in Table 5.3 for the MC samples and Table 2.11 for the e+$\not\!\!E_T$ control sample. The fitting procedure for the t_{corr} distribution for the events passing all cut is to use a double Gaussian distribution with the right vertex Gaussian is fixed with a mean =0.0 ns and a RMS =0.65 ns and the wrong vertex Gaussian RMS is fixed =2.0 ns while the mean and normalization are allowed to vary.

In these fits of the MC samples and e+$\not\!\!E_T$ control samples, the right vertex mean and RMS are fixed to be 0.0 ns and 0.65 ns respectively and the normalization is allowed to float. Likewise the wrong vertex RMS is fixed to 2.0 ns while the mean and normalization of the distribution are allowed to float. As can be seen from the Figure 5.16 this double Gaussian assumption models the resulting timing distribution very well.

We can further examine one of the assumptions made in the fits in Figure 5.16; namely the assumption that the wrong vertex distribution is described by a Gaussian with an RMS of 2.0 ± 0.1 ns. Figure 5.17 shows the results of testing this hypothesis for our six MC samples given in Table 5.1 using the event selection requirements listed in Table 5.3 as well as the exclusive e+$\not\!\!E_T$ data selected (described in Section 2.4.1 using Table 2.11). We allow the wrong vertex mean and RMS to vary for each

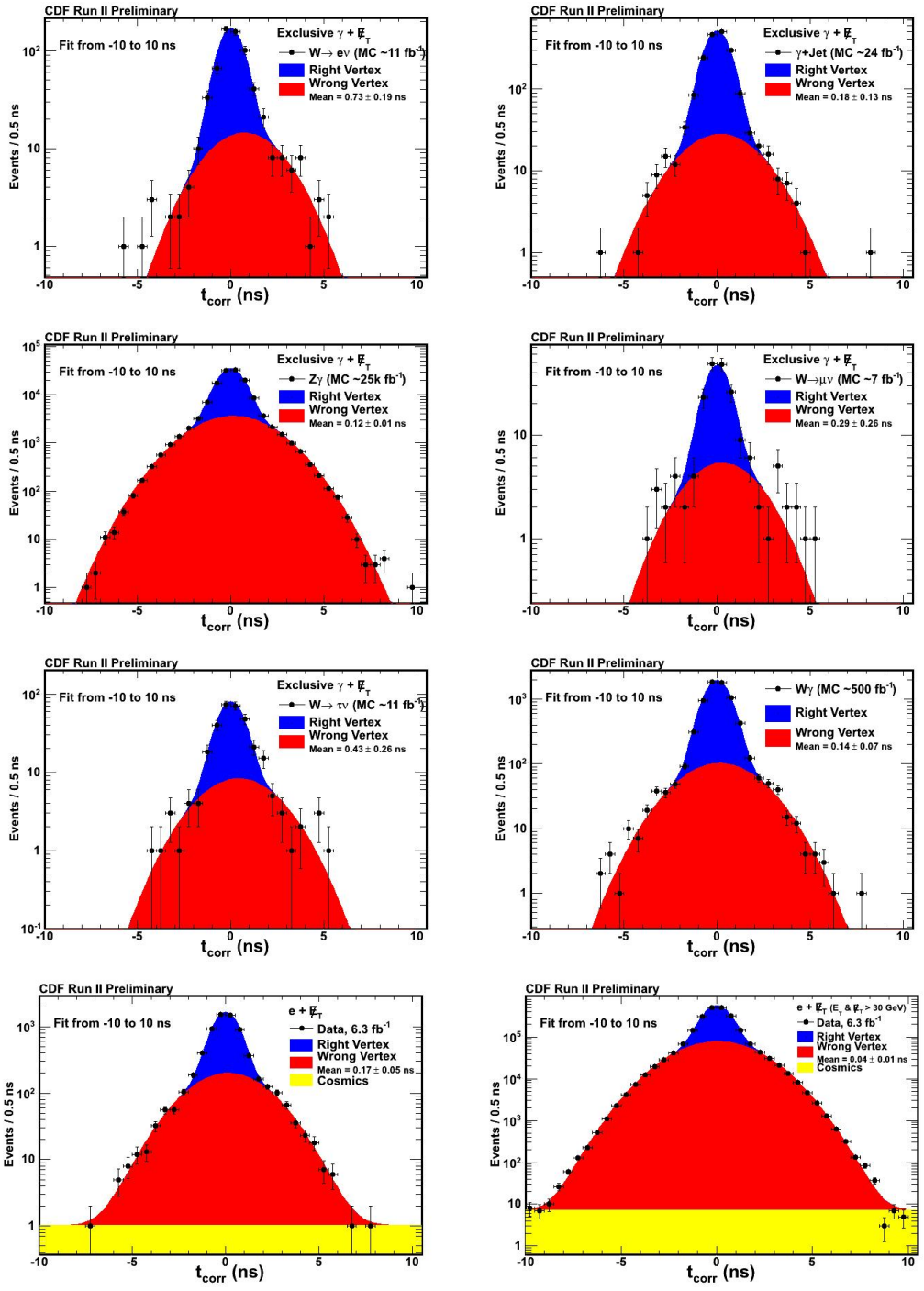

Fig. 5.16. W→ eν, γ+Jet, Zγ, W→ $\mu\nu$, W→ $\tau\nu$, and Wγ Monte Carlo events passing the exclusive $\gamma_{delayed}$+$\not\!\!E_T$ cuts outlined in Table 5.3 and e+$\not\!\!E_T$ control sample passing cuts outlined in Table 2.11. The t_{corr} distribution for the events passing all cuts is fit with a double Gaussian distribution. In this fit the right vertex (blue) Gaussian is fixed with a mean =0.0 ns and a RMS =0.65 ns and the wrong vertex (red) Gaussian RMS is fixed =2.0 ns while the mean and normalization are allowed to vary.

sample during the double Gaussian fit and keep the right vertex mean and RMS fixed to 0.0 and 0.65 ns respectively.

We can clearly see from Table 5.5, which is a summary of the results in Figure 5.17, that the assumption that the wrong vertex distribution is given by a Gaussian with RMS 2.0 ±0.1 ns is an accurate assumption over a large range of wrong vertex means and across a variety of background samples.

Sample	**Wrong Vertex Mean (ns)**	**Wrong Vertex RMS (ns)**
W→ eν MC	0.69 ± 0.22 ns	2.18 ± 0.17 ns
γ+Jet MC	0.18 ± 0.13 ns	2.04 ± 0.16 ns
Zγ MC	0.08 ± 0.05 ns	1.97 ± 0.05 ns
W→ $\mu\nu$ MC	0.30 ± 0.23 ns	2.06 ± 0.18 ns
W→ $\tau\nu$ MC	0.48 ± 0.22 ns	1.97 ± 0.22 ns
Wγ MC	0.14 ± 0.09 ns	2.14 ± 0.08 ns
e+$\not\!\!E_T$ Data	0.16 ± 0.07 ns	2.05 ± 0.07 ns
e+$\not\!\!E_T$ Data (E_T&$\not\!\!E_T$ > 30 GeV)	0.04 ± 0.05 ns	1.98 ± 0.05 ns

Table 5.5

Summary of Figure 5.17 Monte Carlo Backgrounds applying the exclusive $\gamma_{delayed}$+$\not\!\!E_T$ event selection requirements defined in Table 5.3 and the exclusive e+$\not\!\!E_T$ data samples defined in Table 2.11 when we allow their Wrong Vertex Mean and RMS to vary and fit a double Gaussian to their t_{corr} timing distribution.

We next turn to the subject of being able to predict the wrong vertex mean. We use the observation that a double Gaussian description of the corrected timing distribution well matches the observed behavior of the exclusive $\gamma_{delayed}$+$\not\!\!E_T$ final state and allow a data driven estimate of the number of background events in the signal region.

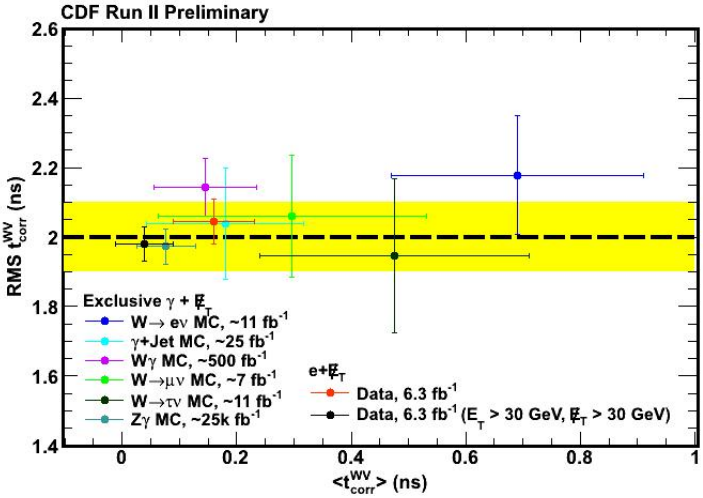

Fig. 5.17. Mean Wrong Vertex RMS (ns) versus Wrong Vertex Mean showing that the assumption that the wrong vertex distribution is well modeled by a Gaussian with an RMS of 2.0 ±0.1 ns for the various MC backgrounds (selected using Table 5.3) and $e+\not\!\!E_T$ data samples (selected using Table 2.11).

6. BACKGROUND ESTIMATION METHODS

Having completed our description of the various SM and non-collision backgrounds, we now turn our attention to predicting the number of events we expect from the backgrounds in the signal region for our final sample. This process of predicting the number of events in the signal region originating from background sources is driven purely from data driven methods and is a multi-step process that we address, each step in turn.

Since the two dominant backgrounds are wrong-vertex events with an unknown mean and cosmic ray events we describe these one at a time. Section 6.1 provides an overview of how we will use the double Gaussian nature of the timing distributions in order to perform a data driven background estimation of the wrong vertex mean. Section 6.2 demonstrates that by knowing the mean of the wrong vertex distribution we are able to predict the number of events expected in the signal region from SM sources. Finally, using a a side-band region in the data, we take into account events coming from cosmic rays and are left with a final predicition for the number of events in the signal region.

However, since it is not possible to directly measure the wrong vertex mean from data, in Section 6.3 we detail a data-driven method to obtain a measurement of the wrong vertex mean. We obtain the wrong vertex mean from a second sample of events that has identical cuts to the signal region, but with one requirement reversed. This allows the sample to be independent but have similar properties that should allow us to measure the mean of the wrong vertex distribution. In particular, we select a sample of events passing all the exclusive $\gamma_{delayed}$+$\not\!\!E_T$ events (found in Table 5.3) but failing to reconstruct a vertex. We call this sample the "no vertex sample" and assuming that the collision position and time for this sample is the average position and time of all collisions (i.e. $z_0 = 0$ and $t_0 = 0$), we can create an "average" time,

or what we call the no vertex corrected time (t^0_{corr}) and hence measure the mean of this timing distribution.

As we will show in Section 6.4, the mean of the no vertex corrected time reproduces the mean of wrong vertex within small uncertainties. This allows us to predict the wrong vertex mean for our exclusive γ+$\not\!\!E_T$ data sample. Since this is a crucial piece of the analysis we will use all our Monte Carlo samples and e+$\not\!\!E_T$ data samples and demonstrate that the mean of the no vertex timing distribution does an excellent job of approximating the wrong vertex mean to a measurable approximation.

Finally, in section 6.5 we will lay out the procedure for measuring the no vertex mean time and using this to predict the mean of the wrong vertex distribution and its uncertainty. This will hence allow us to predict the expected number of events in the signal region from SM sources and thus add the contribution from cosmic rays for a final predicited value.

6.1 Overview of Data Driven Background Method

A fundamental assumption made thus far in this analysis is that the corrected time distribution for a sample of collision events can be described by a double Gaussian. This double Gaussian timing distribution has one component coming from a correctly identified primary vertex resulting in a Gaussian centered at $t_{corr} = 0$ ns with an RMS of 0.65 ns that we call the "right vertex." Furthermore, the mean of this distribution has been calibrated to be 0.0 ns by what we mean to be a right vertex (photon comes from this vertex). The RMS is determined by the resolution of our timing system which is shown to be $\sim$0.65 ns in Ref. [58] and verified in Section 3.5.

The second component of the double Gaussian comes from when we incorrectly identify the primary vertex and results in a Gaussian with an RMS of 2.0 ns whose mean may vary from sample to sample as was shown in Figure 5.16. We refer to this distribution as the "wrong vertex" timing distribution and the RMS of this

distribution comes directly from the given beam parameters (see Ref. [70]) and is shown empirically to be 2.0 ns from our MC background samples and $e+\not\!\!E_T$ data samples as summarized in Table 5.5.

While the mean of the wrong vertex may vary sample to sample, we can still take advantage of the Gaussian nature of the timing distribution in the exclusive $\gamma_{delayed}+\not\!\!E_T$ final state in order to predict the number of events in the signal region. This prediction can be done if one knows 6 parameters, namely the mean and RMS of the two Gaussians (the right and wrong vertex) as well as their normalizations. As we have seen in Section 5.5, we already know three out of six of these parameters and all that is left is to determine the wrong vertex mean and the relative normalization in order to have all the pieces.

To see this more rigorously, we can describe the number of events in any region, illustrated in Figure 1.14, as having two components. Namely, the number of events coming from the right vertex Gaussian (N_{RV}) and the number of events coming from the wrong vertex Gaussian (N_{WV}). For clarity we take the number of events in the control region (ignoring the cosmics background for the moment), -7 ns to -2 ns, ($N_{Control}$) as an example and write:

$$N_{Control} = \beta_{RV}^{[-7,-2]ns} \cdot N_{RV} + \beta_{WV}^{[-7,-2]ns} \cdot N_{WV} \tag{6.1}$$

where $\beta_{RV}^{[-7,-2]ns}$ and $\beta_{WV}^{[-7,-2]ns}$ can be thought of the fraction of right vertex and wrong vertex events in this region. Because the distributions are well described by Gaussians, $\beta_{RV}^{[-7,-2]ns}$ and $\beta_{WV}^{[-7,-2]ns}$ are given by the error function (Erf) of the right vertex and wrong vertex Gaussians and are hence a function of the mean and RMS of those Gaussians. Thus for $\beta_{RV}^{[-7,-2]ns}$, since we know the mean and RMS of the right vertex Gaussian distribution we can write:

$$\beta_{RV}^{[-7,-2]ns} = Erf(\frac{\sigma_{[0,-2]ns}^{RV}}{2}) - Erf(\frac{\sigma_{[0,-7]ns}^{RV}}{2}) \tag{6.2}$$

The error function gives the probability of a measurement, assuming a normally distributed errors with standard deviation σ, having a distance less then some value from the mean of the distribution [80]. In Equation 6.2 we are evaluating this error function for the right vertex at two points (-2 ns and -7 ns) assuming the mean of the distribution is at $t_{corr} = 0$. Specifically this implies:

$$\begin{aligned} \sigma^{RV}_{[\mu,x]ns} &= \frac{x-\mu}{\sigma^{RV}\sqrt{2}} \\ \sigma^{RV}_{[0,-2]ns} &= \frac{2}{0.65\sqrt{2}} \end{aligned} \tag{6.3}$$

where σ^{RV} is the RMS of the right vertex (0.65 ns). Note, that the factor of $\frac{1}{2}$ in the evaluating of the error functions in Equation 6.2 comes from the fact we are only evaluating one side of the Gaussian. Analogously we evaluate the second error function $Erf(\frac{\sigma^{RV}_{[0,-7]ns}}{2})$ in the same way thus giving us the fraction of events we expect from the right vertex in the control region.

Next we evaluate $\beta^{[-7,-2]ns}_{WV}$ which is the fraction of events from the wrong vertex Gaussian in the control region.

$$\begin{gathered} \beta^{[-7,-2]ns}_{WV} = Erf(\frac{\sigma^{WV}_{[\mu,-2]ns}}{2}) - Erf(\frac{\sigma^{WV}_{[\mu,-7]ns}}{2}) \\ \text{with} \end{gathered} \tag{6.4}$$

$$\begin{aligned} \sigma^{WV}_{[\mu,x]ns} &= \frac{x-\mu}{\sigma^{WV}\sqrt{2}} \\ \sigma^{WV}_{[\mu,-2]ns} &= \frac{2-\mu}{2.0\sqrt{2}} \\ \sigma^{WV}_{[\mu,-7]ns} &= \frac{7-\mu}{2.0\sqrt{2}} \end{aligned} \tag{6.5}$$

where in Equation 6.5 we explicitly leave the mean of the wrong vertex as a variable allowing us to evaluate this for a range of different wrong vertex means. Thus, we have reduced equation 6.1 to having only two unknowns, namely N_{RV} and N_{WV}. We now note that we can write a very similar equation for the number of events in the bulk region (-2 ns to 2 ns):

$$N_{Bulk} = \beta_{RV}^{[-2,2]ns} \cdot N_{RV} + \beta_{WV}^{[-2,2]ns} \cdot N_{WV} \tag{6.6}$$

where $\beta_{RV}^{[-2,2]ns}$ and $\beta_{WV}^{[-2,2]ns}$ are the fraction of right vertex and wrong vertex in the bulk region. Again, we write the error functions of the right vertex and wrong vertex Gaussians in this region as:

$$\begin{aligned} \beta_{RV}^{[-2,2]ns} &= Erf(\tfrac{\sigma_{[0,-2]ns}^{RV}}{2}) - Erf(\tfrac{\sigma_{[2,0]ns}^{RV}}{2}) \\ \beta_{WV}^{[-2,2]ns} &= Erf(\tfrac{\sigma_{[\mu,-2]ns}^{WV}}{2}) - Erf(\tfrac{\sigma_{[2,\mu]ns}^{WV}}{2}). \end{aligned} \tag{6.7}$$

The evaluation of the error functions in equation 6.7 follows exactly as before. Thus we are left with equations 6.1 and 6.6 having two equations and two unknowns leaving μ as a free varialbe. Therefore, since we can measure the number of events in data in the bulk and control regions, we can exactly solve for the number of events in any timing region in terms of the number of events from the right vertex and wrong vertex Gaussians. Moreover, we can solve this for a range of wrong vertex means as well as allowing the wrong vertex RMS to vary within known systematics. Looking at the ratio of the $\frac{N_{SR}}{N_{CR}}$ has the advantage of the normalization of the Gaussians dropping out of the prediction (in the limit that the contribution from β_{RV} is small) thus making the only important variable the mean of the wrong vertex distribution.

$$Ratio = \frac{N_{Signal}}{N_{Control}} = \frac{\beta_{RV}^{[2,7]ns} \cdot N_{RV} + \beta_{WV}^{[2,7]ns} \cdot N_{WV}}{\beta_{RV}^{[-7,-2]ns} \cdot N_{RV} + \beta_{WV}^{[-7,-2]ns} \cdot N_{WV}} \tag{6.8}$$

where N_{RV} and N_{WV} are now solved in terms of N_{Bulk}, $N_{Control}$, $\beta_{RV}^{[-2,2]ns}$, $\beta_{WV}^{[-2,2]ns}$, $\beta_{RV}^{[-7,-2]ns}$, $\beta_{WV}^{[-7,-2]ns}$ and is thus only a function of the wrong vertex mean. Thus, to a good degree of approximation, we can estimate the ratio as a function of the wrong vertex mean, $Ratio(\mu^{WrongVertex}) = F(\mu^{WrongVertex})$. Said differently, given a number of events in the control region and the mean of the wrong vertex we can predict the number of events in the signal region coming from wrong vertex sources.

In Figure 6.1 we show what this prediction curve for the ratio of number of events in the signal region (N_{SR}) to the number of events in the control region (N_{CR}) looks like with this double Gaussian assumption for various wrong vertex means where we ignore the contribution from the right vertex sample. This assumption is typically true for wrong vertex fractions of $\sim$10% or greater. The yellow band represents a systematic uncertainty in the RMS of the wrong vertex of $\pm$0.1 n,s which is the dominant systematic uncertainty. It should be noted here that we are only trying to predict the number of background events from SM contributions in the signal region. At no point have we used any information about the number of events in the signal region nor anything about the shape of the timing distribution in the signal region except that SM sources will be Gaussian.

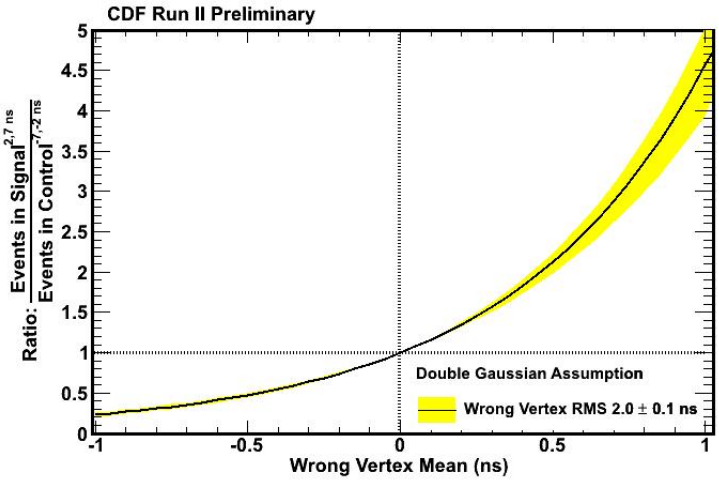

Fig. 6.1. Using the assumption that the timing distribution is described by a double Gaussian the number of events in the signal region can be predicted by using the wrong vertex mean. Note: The yellow band represents a systematic uncertainty on the RMS of the wrong vertex Gaussian which we take the conservative overestimate of $\pm$10 percent. Additionally we also assume that the right vertex events are a negligible contribution.

As can be seen in Figure 6.1, the ratio of $\frac{N_{SR}}{N_{CR}}$ for a wrong vertex mean = 0.0 ns is exactly 1.0 as was previously assumed. In the next section we go through the procedure of predicting the number of events in the signal region for a known wrong vertex mean for our various MC backgrounds as well as e+$\not\!\!E_T$ data samples.

6.2 Predicting Event Rates for Biased-timing Samples

Having established that our wrong vertex distribution is well modeled by a Gaussian with a RMS = 2.0±0.1 ns for our background samples in Section 5.5, we now test the hypothesis put forward in Equation 6.8. Specifically how well the prediction between wrong vertex mean and the ratio of events in the signal and control regions holds in our various background samples. Figure 6.2 shows the results of the counting experiment for the various MC and e+$\not\!\!E_T$ data samples. In this case we count the number of events in the signal and control region in order to compute the ratio and the error is just the statistical error on the sample. We then plot this versus the fitted wrong vertex mean when we fit the various samples using the double Gaussian assumption where the mean and RMS of the right vertex are fixed to 0.0 ns and 0.65 ns respectively and the RMS of the wrong vertex is fixed to 2.0 ns. The fit is performed between -10 ns and 10 ns and the wrong vertex mean is allowed to vary until the best fit is found. The results of these fits are summarized in Table 6.1.

From Figure 6.2 we can see that the relationship between the observed number of events in the control and signal region to the wrong vertex mean is very well modeled by our double Gaussian assumption. This remarkable result means that for a sample of events in the exclusive $\gamma_{delayed}$+$\not\!\!E_T$ final state, that once we are able to determine the wrong vertex mean and we observe the number of events in the control region we can uniquely determine the number of events expected in the signal region. The task of finding an independent way of determining the wrong vertex mean and thus measuring the bias present in the sample is the subject material of the next section.

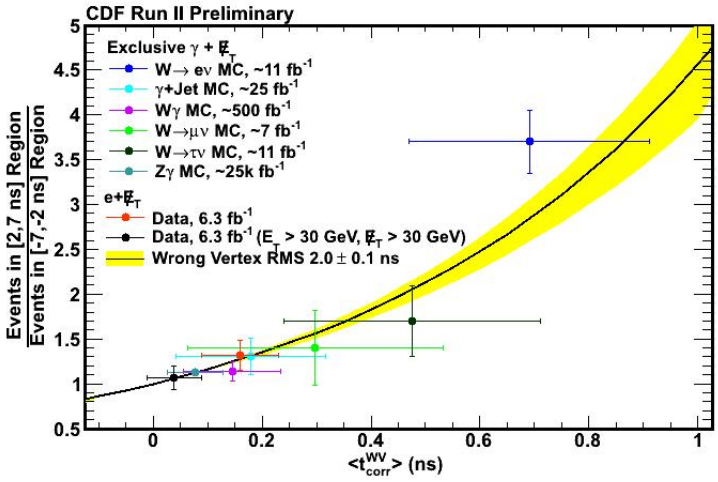

Fig. 6.2. Ratio of the number of events observed in the signal region (2 ns to 7 ns) to the number of event observed in the control region (-7 ns to -2 ns) versus the observed wrong vertex mean. This shows that the double Gaussian assumption where the right vertex distribution is fixed and the wrong vertex mean is allowed to vary (solid black line) does model the expected number of events in the signal region for the various MC backgrounds in addition to e + $\not\!\!E_T$ data samples.

6.3 Measuring the Bias for the Sample

The first thing that is important to note, as we now turn our attention to establishing a way to measure the wrong vertex mean independently, is that naively we may attempt to establish the mean of the wrong vertex by simply fitting from -7 ns to +2 ns and then extrapolating this fit into the signal region. While this should work in the limit of having infinite statistics, this method does not work in data for three major reasons:

1) Events from cosmics rays overwhelm the region from -7 ns to -2 ns and thus may distort the wrong vertex distribution in this area.

Sample	Observed Wrong Vertex Mean (ns)	Predicted Ratio	Observed Ratio
W→ eν MC	0.73 ± 0.19 ns	2.92 ± 1.01	3.70 ± 0.36
γ+Jet MC	0.18 ± 0.13 ns	1.30 ± 0.26	1.30 ± 0.20
Wγ MC	0.14 ± 0.07 ns	1.22 ± 0.14	1.14 ± 0.11
Zγ MC	0.12 ± 0.01 ns	1.20 ± 0.01	1.12 ± 0.02
W→ $\mu\nu$ MC	0.29 ± 0.26 ns	1.50 ± 0.70	1.40 ± 0.41
W→ $\tau\nu$ MC	0.43 ± 0.26 ns	1.90 ± 0.90	1.70 ± 0.40
e+$\not\!\!E_T$ Data	0.16 ± 0.05 ns	1.26 ± 0.16	1.32 ± 0.17
e+$\not\!\!E_T$ Data *(E_T > 30 GeV and $\not\!\!E_T$ > 30 GeV)*	0.04 ± 0.05 ns	1.03 ± 0.07	1.06 ± 0.13

Table 6.1

Summary of Monte Carlo backgrounds and e+$\not\!\!E_T$ data wrong vertex mean, the predicted and observed ratio of the number of events in the signal region (2 ns to 7 ns) to the number of events in the control region (-2 ns to -7 ns) after applying the exclusive $\gamma_{delayed}$+$\not\!\!E_T$ event selection defined in Table 5.3. The observed wrong vertex mean here is measured using a double Gaussian fit to the data and assuming a right vertex mean = 0.0 ns and RMS = 0.65 ns as well as a wrong vertex RMS=2.0.

2) In the region from -2 ns to 2 ns events from the right vertex dominate thus making it difficult to measure the mean of the wrong vertex in this region.

3) All of these problems are compounded as the wrong vertex mean becomes larger.

With these problems in mind, we consider an orthogonal set of events that allow us to measure the wrong vertex mean for the exclusive $\gamma_{delayed}$+$\not\!\!E_T$ final state. For such a sample we look to the events that pass all of our exclusive $\gamma_{delayed}$+$\not\!\!E_T$ requirements (outlined in Table 5.3) but do not have a reconstructed SpaceTime vertex. As illustrated in Figure 6.3, we refer to this sample as the "no vertex" sample. As will be explained further, while we expect this sample to be dominated by cosmic ray backgrounds, the events from a collision but had no reconstructed vertex should have the same underlying physics and topology and thus the same timing bias as the

wrong vertex distribution. Recall that our wrong vertex events may or may not have had their true vertex reconstructed. We note that in our MC backgrounds samples where we selected the wrong vertex, the right vertex was only available to be selected a small fraction (∼50%) of the time.

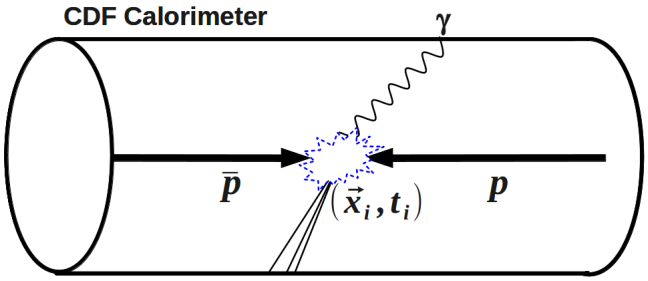

Fig. 6.3. The hypothesis is that the average timing distribution of the wrong vertex distribution has only to do with underlying physics and topology of the events and is not intrinsically related to the timing measurement and reconstruction of the right vertex. If no good SpaceTime vertex is reconstructed, but the event passes all the other exclusive $\gamma_{delayed}+\not\!\!E_T$ event selection requirements we can still construct a pseudo-corrected time (t^0_{corr}) where we assume the initial time and position was $t_0 = 0$ ns and $z_0 = 0$ cm respectively and we can infer the true wrong vertex timing mean.

If no good SpaceTime vertex is reconstructed, but the event passes all the other exclusive $\gamma_{delayed}+\not\!\!E_T$ event selection requirements we can still construct a pseudo-corrected time (t^0_{corr}) where we assume the initial time and position was $t_0 = 0$ ns and $z_0 = 0$ cm respectively. This is a reasonable assumption on average since this is where the overwhelming majority of collisions occur. The hypothesis is that the mean of the "no vertex" sample will be essentially the same as the mean of the wrong vertex distribution.

The justification behind the hypothesis that the mean of the no vertex distribution will be close to the mean of the wrong vertex distribution comes from understanding the three parts of the corrected time distribution itself. The first part of

can be thought of as the geometric time of flight difference relative to the center of the detector ($TOF_{(z=0)}$). As we showed in section 5.3 this is a process dependent factor and has to do with the relative topology of the physics process and a small source of the timing bias in a sample. The second part of the corrected time is the time of flight difference relative to the chosen vertex (TOF_{Vtx}). Since this is the same for all processes selected this time of flight introduces the majority of the bias to the sample and depends on the intrinsic beam parameters.

Lastly, you have the variation of the time of the true collision and the variation of the time of collision for any unrelated collision which creates a vertex. Again, this will be true for all processes and only has to do with the spread of the vertex in time (known to be ∼1.28 ns from beam parameters as shown in Section 2.4) and only causes a difference in the RMS of the wrong vertex distribution of $\sqrt{{t^{RMS}_{ArrivalTime}}^2 + {t^{RMS}_{EMTiming}}^2 + {t^{RMS}_{InitalTime}}^2} = \sqrt{(1.6)^2 + (0.65)^2 + (1.28)^2} \sim$ 2.0 ns versus a RMS of the "no vertex" distribuition of $\sqrt{{t^{RMS}_{EMTiming}}^2 + {t^{RMS}_{InitalTime}}^2} = \sqrt{(0.65)^2 + (1.28)^2} \sim 1.6$ ns.

A representation of these assumptions can be seen on the LHS of Figure 6.4. An important fact to note is that the variation in the collision distribution has an RMS of ∼28 cm as shown in Section 2.4 whereas the distance from the beam line to the CES is ∼184 cm. Thus, even though the geometric time of flight difference relative to the center of the detector ($TOF_{(z=0)}$) is a sample dependent number, its relative importance to the timing bias is small compared to the time of flight difference relative to the chosen vertex (TOF_{Vtx}).

The RHS of Figure 6.4 is for a series of pseudo-experiments where we calculate the corrected time of the wrong vertex t^{WV}_{corr} and the corrected time for the no vertex (t^{0}_{corr}) distributions. Here we generate verticies according to the z and t parameters of the Tevatron beam in Table 2.1 and assume symmetric production about the CES z position. We can see that the assumption that TOF_{Vtx} is the same for the no

vertex and wrong vertex distributions results in their means being very close to one another.

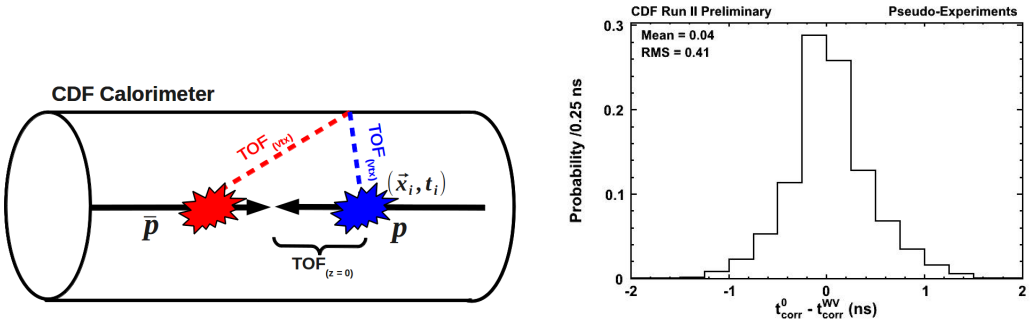

Fig. 6.4. (LHS) An illustration showing the various components of the Time of Flight components of the t_{corr} coming from the difference relative to the center of the detector ($TOF_{(z=0)}$) and the time of flight difference relative to the chosen vertex (TOF_{Vtx}) (RHS) The results of pseudo-experiments where verticies are generated according to the z and t parameters of the Tevatron and the mean of the corrected time calculated from a wrong vertex is subtracted from the mean of the corrected time assuming $z = 0$ and $t = 0$ just as we would in the no vertex case demonstrating that the expected mean of the two distributions should be very similar.

In order to test the hypothesis that the mean of the no vertex distribution (t^0_{corr}) can predict the mean of the wrong vertex (t^{WV}_{corr}) we first test the underlying assumption of the RMS of the no vertex distribution ∼1.6 ns. We use the six MC samples given in Table 5.1 and the event selection requirements listed in Table 5.3 as well as $e+\not\!\!E_T$ data selected using Table 2.11. However, we now require these samples to explicitly fail the good SpaceTime vertex selection in order to construct the no vertex timing distribution. We examine the no vertex timing distribution t^0_{corr} for each sample and fit a Gaussian from -5 ns to 3 ns allowing the mean and RMS to vary and find the best fit parameter. We pick the range for the Gaussian fit to start at -5 ns in order to avoid any potential contamination from beam halo events which we expect to begin to be present at t^0_{corr} <-5 ns, as described in Section 4.3. We only

fit out to $t^0_{corr} = 3$ ns in order to avoid any potential contamination from signal like events that we expect to see above 3 ns, as described in Section 1.4. The summary of the results of these fits is given in Table 6.2 and can be see graphically in Figure 6.5. We note that the data points all fall within the yellow band (± 10% the nominal RMS) for a wide range of no vertex RMS's.

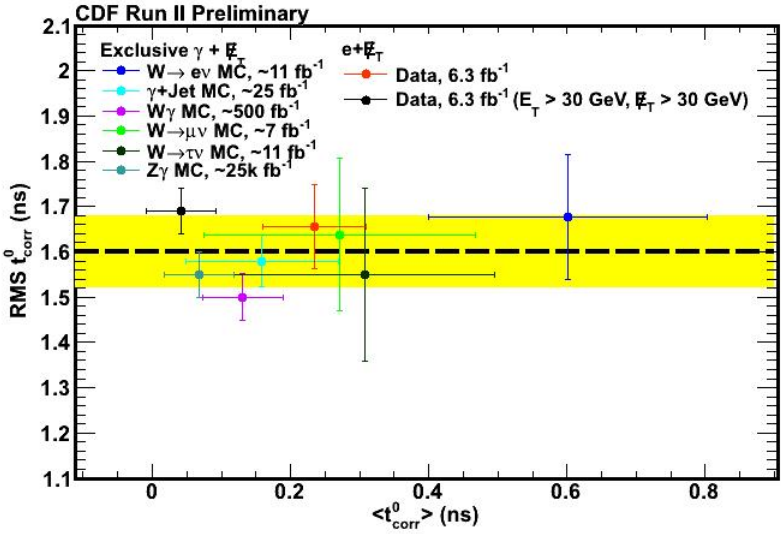

Fig. 6.5. Mean no vertex corrected time (t^0_{corr}) RMS versus mean demonstrating that the assumption that the no vertex corrected time distribution is well modeled by a Gaussian with an RMS of 1.6 ±0.08 ns for the various MC backgrounds in addition to e + $\not\!\!E_T$ data samples. The no vertex mean and RMS is found by fitting the no vertex corrected time (t^0_{corr}) distribution with a single Gaussian from -5 ns to 3 ns where the Gaussian RMS and mean are allowed to vary to find the best fit.

6.4 Summary of Results for the Control and Monte Carlo Samples

For all the MC and data samples examined the assumption that the RMS of no vertex timing distribution, t^0_{corr}, is accurately described by a Gaussian with RMS of 1.6 ±0.08 ns. Figure 6.6 shows the results of the a Gaussian fit from -5 ns< t^0_{corr} <3 ns

Sample	No Vertex Mean (ns)	No Vertex RMS (ns)
W→ eν MC	0.61 ± 0.20 ns	1.68 ± 0.14 ns
γ+Jet MC	0.16 ± 0.11 ns	1.58 ± 0.06 ns
Zγ MC	0.07 ± 0.05 ns	1.55 ± 0.05 ns
W→ $\mu\nu$ MC	0.27 ± 0.20 ns	1.64 ± 0.17 ns
W→ $\tau\nu$ MC	0.31 ± 0.19 ns	1.56 ± 0.19 ns
Wγ MC	0.13 ± 0.06 ns	1.50 ± 0.05 ns
e+$\not\!\!E_T$ Data	0.23 ± 0.08 ns	1.66 ± 0.09 ns
e+$\not\!\!E_T$ Data (E_T&$\not\!\!E_T > 30$ GeV	0.04 ± 0.05 ns	1.69 ± 0.05 ns

Table 6.2

Summary of Figure 6.5 Monte Carlo backgrounds applying the exclusive $\gamma_{delayed}$+$\not\!\!E_T$ event selection requirements defined in Table 5.3 and the exclusive e+$\not\!\!E_T$ data samples defined in Table 2.11 but failing the good SpaceTime vertex requirement. The no vertex mean and RMS is found by fitting the no vertex corrected time (t^0_{corr}) distribution with a single Gaussian from -5 ns to 3 ns where the Gaussian RMS and mean are allowed to vary to find the best fit.

with the RMS fixed at 1.6 ns and the mean allowed to vary and find the best fit for the six MC background samples and the exclusive e+$\not\!\!E_T$ data samples.

Having established the assumption that the no vertex timing distribution is accurately described by a Gaussian with an RMS of 1.6 ns for our MC backgrounds and e+ $\not\!\!E_T$ data, we now look to the comparison of the mean of the wrong vertex distribution versus the mean of the no vertex distribution. In Figure 6.7 we compare the two measured timing means as all of the points lie on the line at 45 degrees (where the two measured timing means equal one another). The mean of the wrong vertex (as measured from the double Gaussian fit of the t_{corr} distribution assuming the right vertex is given by a Gaussian with a mean =0.0 ns and an RMS =0.65 ns and the wrong vertex distribution given by a Gaussian with a RMS = 2.0 ns, described in Section 6.2) and the mean of the no vertex distribution (as measured from

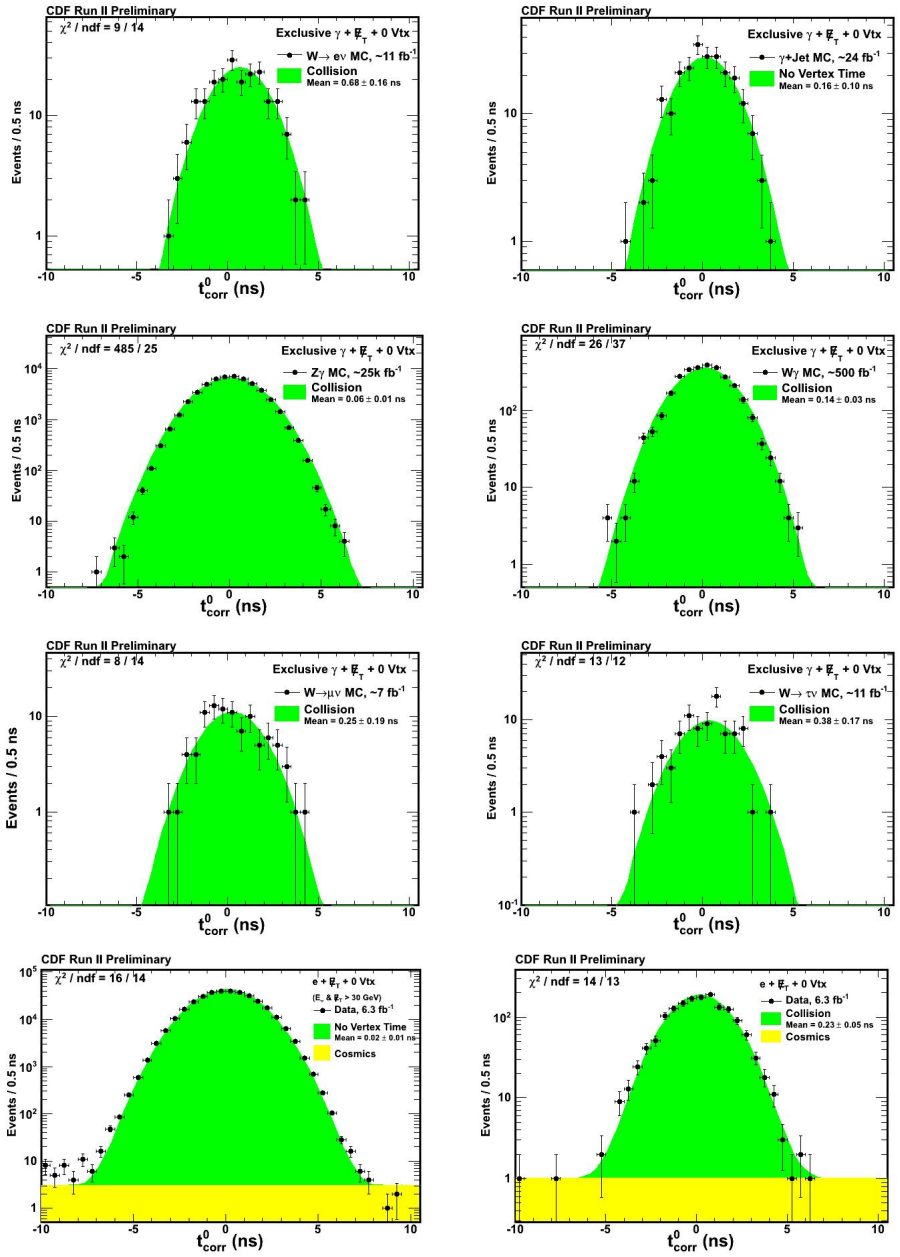

Fig. 6.6. No vertex distribution t^0_{corr} for the six MC samples outlined in Table 5.1 as well as e+$\not\!\!E_T$ data samples showing the results of the Gaussian fit from -5 ns to 3 ns with a fixed RMS = 1.6 ns in order to estimate the wrong vertex mean.

the Gaussian fit of the t^0_{corr} distribution with RMS = 1.6 ns fit between -5 ns and 3 ns) are are thus shown to be nearly equivalent values for our six MC background samples as the two exclusive $e+\not\!\!E_T$ data samples. The results of these fits is shown in Figure 6.7 are summarized in Table 6.3.

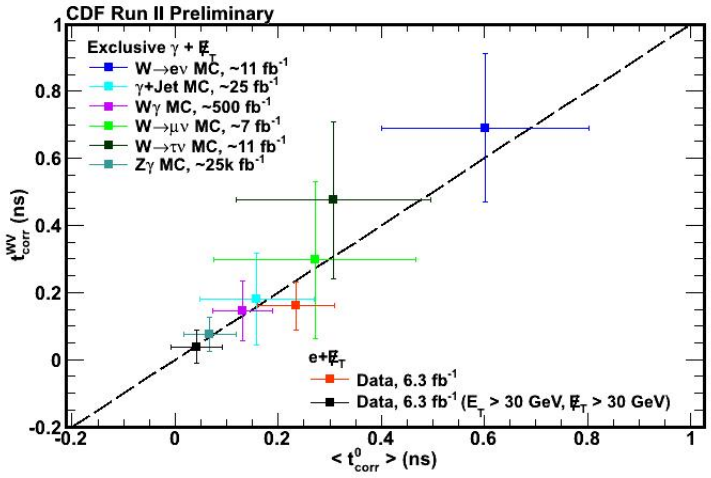

Fig. 6.7. Wrong vertex mean versus no vertex mean demonstrating that for the various MC backgrounds and to e $+\not\!\!E_T$ data samples the no vertex mean is an accurate proxy for the wrong vertex mean. This fact allows us to predict the wrong vertex mean for a given sample by measuring a sample of events that pass all the other selection requirements but fail to reconstruct a vertex.

We note that the two measurements are not always identical, so for this reason we conservatively overestimate any systematic difference between the wrong vertex mean and the no vertex mean to be a 100 picoseconds. This is in addition to the systematic uncertainty in the RMS of the wrong vertex of 0.1 ns already taken into account. Thus we find that:

$$N_{signal} = R(\mu^{WV} = \mu^{NV}) \cdot N_{control} \tag{6.9}$$

Sample	Wrong Vertex Mean (ns)	No Vertex Mean (ns)
W→ eν MC	0.73 ± 0.19 ns	0.68 ± 0.16
γ+Jet MC	0.18 ± 0.13 ns	0.16 ± 0.10
Wγ MC	0.14 ± 0.07 ns	0.14 ± 0.03
Zγ MC	0.12 ± 0.01 ns	0.06 ± 0.01
W→ $\mu\nu$ MC	0.29 ± 0.26 ns	0.25 ± 0.19
W→ $\tau\nu$ MC	0.43 ± 0.26 ns	0.38 ± 0.17
e+$\not\!\!E_T$ Data	0.16 ± 0.05 ns	0.23 ± 0.05
e+$\not\!\!E_T$ Data *(E_T > 30 GeV and $\not\!\!E_T$ > 30 GeV)*	0.04 ± 0.05 ns	0.02 ± 0.01

Table 6.3

Summary of Monte Carlo backgrounds selected using the exclusive $\gamma_{delayed}$ + $\not\!\!E_T$ selection defined in Table 5.3 and the e+ $\not\!\!E_T$ data selected using the sample defined in Table 2.11. Here we obtain the wrong vertex mean by fitting the corrected time (t_{corr}) distribution with a double Gaussian function from -10 ns to 10 ns where the right vertex Gaussian mean = 0.0 ns and RMS = 0.65 ns and the wrong vertex Gaussian RMS = 2.0 ns and the mean is allowed to vary to find the best fit. The no vertex mean is found by fitting the no vertex corrected time (t^0_{corr}) distribution with a single Gaussian from -5 ns to 3 ns where the Gaussian RMS = 1.6 ns and the mean is allowed to vary to find the best fit.

and take the systematics on R due to the uncertainty between the relation $\mu^{WV} = \mu^{NV}$.

To test how well this relation predicts the number of events in the signal region with our 8 control samples we show the results in Figure 6.8. By comparing the results in Figure 6.2 to Figure 6.8, as shown in Table 6.4, we see that the no vertex mean does an excellent job modeling the expected ratio from the timing bias. Thus, we have a method that uses an independent sample (the no vertex sample), that allows us to measure the WV mean. That, taken in conjunction with the number of events in the control region, gives us a data-driven estimate of the number of events in the signal region for SM backgrounds. The uncertainty, as we will see is dominated

by the statistical uncertainty of the number of events from collision in the no vertex sample.

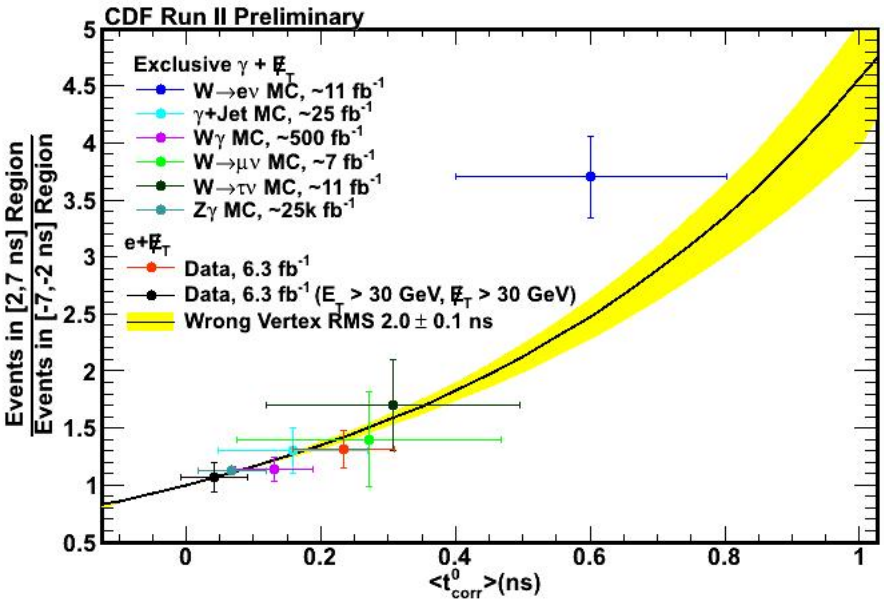

Fig. 6.8. Ratio of the number of events observed in the signal region (2 ns to 7 ns) to the number of event observed in the control region (-7 ns to -2 ns) versus the observed no vertex mean. This shows that using the double Gaussian assumption and taking the mean of the no vertex distribution for the wrong vertex mean to model the expected number of events in the signal region for the various MC backgrounds in addition to e $+\not\!\!E_T$ data samples.

In the next section we formalize the background estimation procedure in the exclusive $\gamma_{delayed}+\not\!\!E_T$ final state utilizing the fact that we can predict the wrong vertex mean from the no vertex sample and now take into account the contributions from cosmic ray background sources.

Sample	Observed No Vertex Mean (ns)	Predicted Ratio	Observed Ratio
W→ eν MC	0.68 ± 0.16 ns	2.74 ± 0.76	3.70 ± 0.36
γ+Jet MC	0.16 ± 0.10 ns	1.27 ± 0.20	1.30 ± 0.20
Wγ MC	0.14 ± 0.03 ns	1.23 ± 0.05	1.14 ± 0.11
Zγ MC	0.06 ± 0.01 ns	1.09 ± 0.02	1.12 ± 0.02
W→ $\mu\nu$ MC	0.25 ± 0.19 ns	1.46 ± 0.48	1.40 ± 0.41
W→ $\tau\nu$ MC	0.38 ± 0.17 ns	1.77 ± 0.51	1.70 ± 0.40
e+$\not\!\!E_T$ Data	0.23 ± 0.05 ns	1.39 ± 0.31	1.32 ± 0.17
e+$\not\!\!E_T$ Data *(E_T > 30 GeV and $\not\!\!E_T$ > 30 GeV)*	0.02 ± 0.01 ns	1.03 ± 0.07	1.06 ± 0.13

Table 6.4

Summary of Monte Carlo backgrounds and e+ $\not\!\!E_T$ data no vertex mean and the predicted ratio using that measured mean as well as the observed ratio of the number of events in the signal region (2 ns to 7 ns) to the number of events in the control region (-2 ns to -7 ns) after applying the exclusive $\gamma_{delayed}$+$\not\!\!E_T$ event selection defined in Table 5.3.

6.5 The Background Estimation Procedure

To briefly recap, in Sections 6.1 and 6.3 we demonstrated how using the double Gaussian assumption on the corrected time distribution it is possible to predict the number of events expected in the signal region (2 ns to 7 ns) from Standard Model sources if we know the mean of the wrong vertex distribution. In Sections 6.2 and 6.4 we showed how we can predict the wrong vertex mean by using an orthogonal sample to the exclusive $\gamma_{delayed}$+$\not\!\!E_T$ final state. Namely, by measuring the mean corrected time (assuming $z_0 = 0$ and $t_0 = 0$) for events that pass all our event selection requirements but fail to reconstruct a vertex (t^0_{corr}) which we call the "no vertex" sample.

In this section we will lay out the procedure by which we will use the information from the cosmics region 20 ns to 80 ns, the mean of the no vertex distribution, and finally the number of events observed in the control region (-7 ns to -2 ns) to predict

the number of events expected in the signal region (2 ns to 7 ns) from Standard Model sources.

We begin the procedure as follows:

1) Select events for the exclusive $\gamma_{delayed}$+$\not\!\!E_T$ final state.

All events are selected using the criteria outlined in Table 5.3. We sort events into events that have a good SpaceTime vertex and events with no good SpaceTime vertex. From this bifrication we construct two corrected time distributions. For the events having a good SpaceTime vertex we construct the typical t_{corr} variable defined in Equation 1.7. Events that do not have a good SpaceTime vertex become the "no vertex" sample and we construct a corrected time assuming $z_0 = 0$ and $t_0 = 0$ (t^0_{corr}).

2) Estimate the cosmic ray event rate.

Since events from cosmic rays represent a significant contribution for both the good vertex and no vertex sample, we must estimate their contamination to the regions under consideration. Thus, for both t_{corr} and t^0_{corr} timing distribution, we look at the events in the timing region from 20 ns to 80 ns and fit a straight line in this region. This fitted rate gives us an estimate of the rate of cosmics per nanosecond present in both the no vertex and good vertex samples (which is expected to be different for the two samples). By taking the rate of predicted cosmics per nanosecond and multiplying by five nanoseconds you get a prediction for the number of cosmic ray events expected in the signal and control regions in the case of the good vertex sample. Meanwhile, using the cosmics per nanosecond rate measured in the no vertex sample you simply multiply by eight nanoseconds to obtain a prediction of the number of cosmic ray events for the fit region of -5 ns to 3 ns.

3) Measure the mean of the "no vertex" timing distribution.

Using the t^0_{corr} distribution, fit a Gaussian with a RMS = 1.6 ns from -5 ns to 3 ns and measure the mean of this distribution and the error of the fit. This fit takes into account the measured cosmics rate for this sample since the function being fit is a Gaussian plus a straight line where the value of the straight line is fixed from the cosmics region.

4) Predict the number of events in the Signal Region.

Finally, using the mean of the no vertex distribution, the measured cosmics rate, and the number of events observed in the bulk and control regions we can uniquely calculate the number of events expected from Standard Model sources using the mathematics described in section 6.1. With this prediction we can estimate the number of events from both cosmics and wrong vertex in the region from 2 ns to 7 ns as well as the error on this estimation. Ultimately, the difference between the predicted number of events in the signal region and the observed number will indicate if we have evidence for new physics in the exclusive $\gamma_{delayed} + \not{E}_T$ final state.

With the data driven background procedure now layed out, we now turn to the results of the search in the exclusive $\gamma_{delayed} + \not{E}_T$ final state and the quantification of the associated errors with our prediction.

7. SEARCHING FOR NEW PHYSICS IN THE EXCLUSIVE $\gamma_{DELAYED} + \not{E}_T$ FINAL STATE

In this chapter we will present the results of the search in the exclusive $\gamma_{delayed} + \not{E}_T$ final state. Section 7.1 presents the results of the event selection outlined in Table 5.3 when applied to the 6.3 fb^{-1} data sample. We next use the data driven background estimation, described in Section 6.5, to estimate the number of events expected in the signal region (2 ns to 7 ns) from Standard Model and non-collision sources. In Section 7.2 we detail the results of the search and conclude that we find no significant excess above background predicition.

7.1 Event Selection and Background Predictions

Table 7.1 shows the results of the exclusive $\gamma_{delayed}+\not{E}_T$ event selection described in Table 5.3. We have 5,421 events passing all our event selection requirements and having a SpaceTime vertex which we will use to construct the t_{corr} timing distribution and look for evidence of $\gamma_{delayed} + \not{E}_T$. We also have 4,942 events which pass all the event selection requirements but have no SpaceTime vertex reconstructed ("no vertex sample") which we will use to measure the wrong vertex mean from the no vertex corrected time, t^0_{corr}.

As described in the background estimation procedure (Section 6.5), we now estimate the cosmic ray event rate from the t_{corr} distribution. In Figure 7.1, we take the sample of events that have a SpaceTime vertex and look in the timing region between 20 ns to 80 ns. We fit a straightline in this region and use this to estimate the number of events from cosmic rays per nanosecond to be 32 $\pm$ 0.1 events. This rate is then used to predict the number of cosmic ray events we expect in the control, bulk, and signal timing regions.

Event Selection	Number of Events
Pass Online/Offline Trigger selection with an identified photon w/ $E_T \geq 45$ GeV and $\not\!\!E_T \geq 45$ GeV	38,291
Pass Beam Halo Veto	36,764
Pass Cosmics Veto	24,462
Pass Track Veto for Tracks with $P_t > 10$ GeV	16,831
Pass Jet Cluster Veto for Jets with $E_T^0 > 15$ GeV	12,708
Pass Large $\|Z\|$ Vertex Veto	11,702
Pass $e \rightarrow \gamma_{fake}$ Veto	10,363
Events with Good SpaceTime Vertex / No Reconstructed Vertex ***"Good Vertex Sample" / "No Vertex Sample"***	5,421 / 4,942

Table 7.1

Event reduction table for the exclusive $\gamma_{delayed}$+$\not\!\!E_T$ search. The last selection requirement is broken into two samples: 1) Events that do have a reconstructed vertex and 2) Events that do not have a reconstructed vertex ("no vertex sample"). The sample of events that do have a reconstructed vertex are the events in which we perform our search for $\gamma_{delayed} + \not\!\!E_T$ while the "no vertex sample is used to estimate the mean of the wrong vertex as described in Section 6.3.

Next we use the "no vertex" sample to estimate the mean of the wrong vertex distribution. Figure 7.2 shows the corrected timing distribution for the no vertex sample (t^0_{corr}). We then perform a straight line fit from 20 ns $< t^0_{corr} <$ 80 ns to estimate the cosmics rate in the no vertex sample and find a rate of 54 $\pm$6 events. Using this we perform a Gaussian fit from -5 ns$< t^0_{corr} <$3 ns with a fixed RMS = 1.6 ns to estimate the mean of the collision to be 0.12 $\pm$0.17 ns. The bottom of Figure 7.2 shows the $\pm 1\sigma$ variation of the no vertex mean does describe the data well and thus gives us good confidence that this is a good measure of the mean of the t^0_{corr} distribution.

Finally, we estimate the mean of the wrong vertex distribution t^{WV}_{corr} to be the same as the mean of the no vertex distribution t^0_{corr} and conservatively overestimate

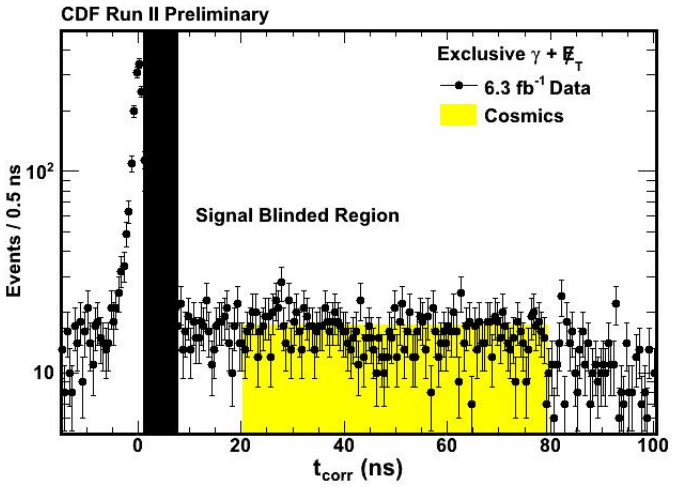

Fig. 7.1. Plot showing the estimate of the cosmic ray rate from the timing region 20 ns to 80 ns and extrapolated back to the signal region.

a 100 picosecond systematic on the error of this predicition. We take this systematic in order to account for any variation between the no vertex and wrong vertex timing seen in our MC backgrounds or e+$\not\!\!E_T$ data samples in Section 6.4. The summary of the basic background estimation values is given in Table 7.2.

Quantity	Measured Value	Error
No Vertex Mean	0.12 (ns)	± 0.17 (ns)
Cosmics per Nanosecond	32 (Events)	± 0.2 (Events)
Wrong Vertex Mean	0.12 (ns)	± 0.20 (ns)

Table 7.2
Summary of the data driven background measurements used for the exclusive $\gamma_{delayed} + \not\!\!E_T$ sample prediction.

In the next section we finalize the data driven background predicition and compare this to the observed number of events as well as show the final t_{corr} timing distribution.

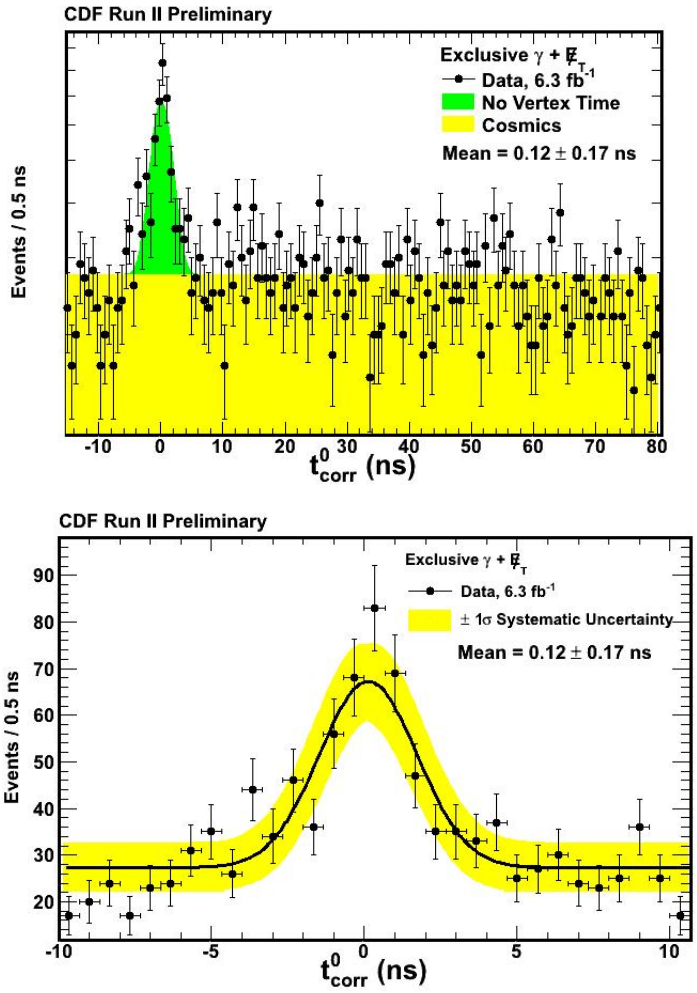

Fig. 7.2. (Top) Plot of the no vertex corrected time (t^0_{corr}) with the fit performed from -5 ns to 3 ns and the RMS fixed to 1.6 ns while the mean of the Gaussian is allowed to vary in order to determine the best fit mean of the of the Gaussian peak. (Bottom) Taking the $\pm 1\sigma$ systematic variation of the mean from the no vertex corrected time showing that the fit of 0.12 $\pm$0.17 ns well describes the distribution.

7.2 Results

Using the estimation methods described in Sections 6.1 and 6.2, we now take the predicted wrong vertex mean of 0.12 $\pm$0.20 ns and the number of events in the bulk

(-2 ns to 2 ns) and control (-7 ns to -2 ns) timing regions to predict the number of events in the signal region. The breakdown of the number of observed events in the cosmics, bulk, and control region is given in Table 7.3.

Timing Region	**Number of Events Observed** (Events)
Cosmics Region *20 ns to 80 ns*	1919
Control Region *-7 ns to -2 ns*	241
Bulk Region *-2 ns to 2 ns*	1463

Table 7.3
Breakdown of the number of observed events in the Cosmics, Control, and Bulk regions for the exclusive $\gamma_{delayed}$+$\not{E}_T$ sample.

Using Equation 6.8 we can compute the ratio of the number of events in the signal region to the number of events in the control region. From the mean of 0.12 ±0.20 ns we find predicted ratio of 1.20 ±0.44. We predict the number of events from cosmic rays in the control region (-7 ns to -2 ns) to be 5 ns $\cdot$ 32 events/ns = 160 ± 1 events. Taking the number of observed events in the control region minus the number of cosmics events we find $N_{Control} = N^{Obs}_{Control} - N^{Cosmics}_{Control}$ = 241 - 160 = 81 ± 1 events (right vertex essentially contributing <1 event in the control and signal timing region). To estimate the number of WV events in the signal region we take $N^{WV}_{Signal} = R \cdot N_{Control}$ = 1.2 $\cdot$ 81 = 96 ±35 events.

Combining the backgrounds, we find that $N^{Expected}_{Signal} = N^{WV}_{Signal} + N^{Cosmics}_{Signal}$ = 96 + 160 = 257 ±35 events. This implies the number of events we expect to come from all background sources in the signal region to be 257 ±35 events. These results are summarized in Table 7.4. It is important to note that here we have assumed that the contribution from right vertex is essentially negligible.

The largest background in this final state comes from cosmics rays at almost a 2:1 ratio in the signal region. Meanwhile, our largest systematic uncertainty comes from the error on the wrong vertex mean which is dominated by the statistics of the events in the no vertex sample.

Quantity *(Events)*	**Prediction** *(Events)*
Number of Events from Cosmic Rays expected in the Signal Region	160 ± 1
Number of Events from Wrong Vertex expected in the Signal Region	96 ± 35
Total Number of Events Predicted in the Signal Region	257 ± 35
Total Number of Events Observed in the Signal Region	322

Table 7.4
Summary of the data driven background prediction and observation for the exclusive $\gamma_{delayed} + \not\!\!E_T$ sample.

With our prediction made of 257 ±35 events expected in the signal region we now compare this to the observed 322 events from the exclusive $\gamma_{delayed} + \not\!\!E_T$ data sample. We show the double Gaussian fit to the data using the predicted wrong vertex mean in the top of Figure 7.3 and the $\pm 1\sigma$ variation of the wrong vertex mean at the bottom of Figure 7.3. Here the normalizations are obtained from the number of events in the control and bulk regions by fitting from -7 ns to +2 ns.

A modest excess remaing of observed minus predicted ($N_{Observed} - N_{Predicted}$) of 65 events in the signal region. While we note that the majority of the bins are above the expectations, we calculate the significance of this excess based purely on the results of the counting experiment. We calculate this significance using the following equation and taking into account the statistical uncertainty expected from the number of observed events in the data as part of the overall uncertainty:

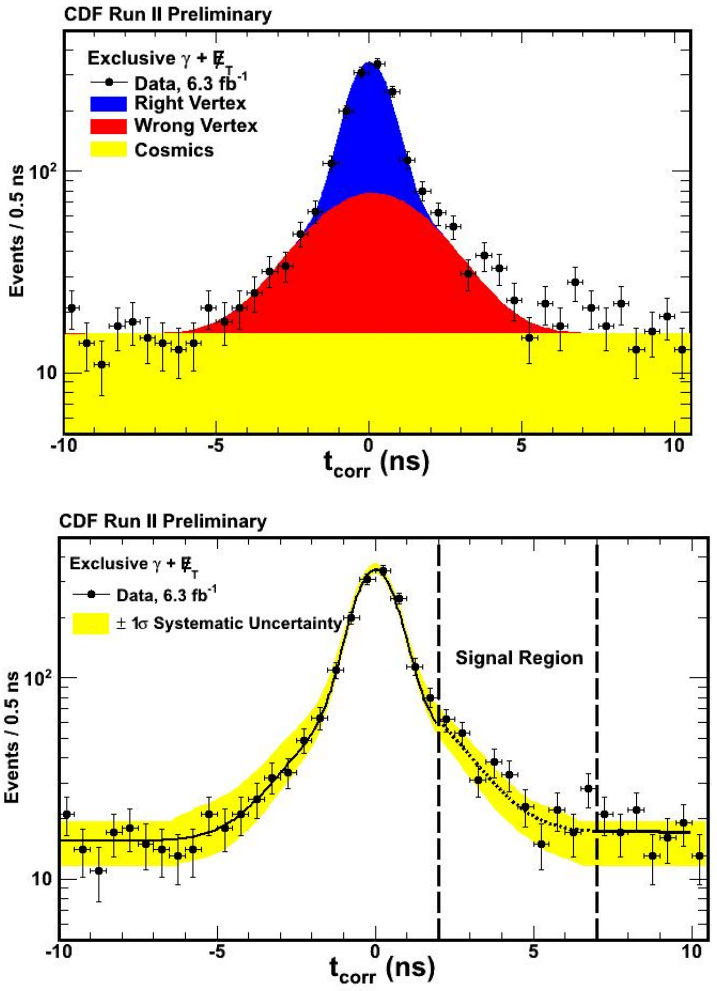

Fig. 7.3. (Top) The t_{corr} distribution of the 6.3 fb^{-1} data showing the fit of the right, wrong vertex, and cosmics prediction. (Bottom) Taking the $\pm 1\sigma$ systematic variation of the mean of the wrong vertex showing that the fit of 0.12 $\pm$0.20 ns well describes the background distribution.

$$
\begin{aligned}
N_\sigma &= \frac{N_{Observed} - N_{Predicted}}{\sqrt{\sigma^2_{N_{Pred}} + \sigma^2_{N_{Obs}}}} \\
N_\sigma &= \frac{322 - 257}{\sqrt{35^2 + 322}} \\
N_\sigma &= 1.65
\end{aligned}
\tag{7.1}
$$

An $N_\sigma = 1.65$ gives a one sided p-value (the estimatied probability that this excess is inconsistent with a null hypothesis) of $\sim 5\%$. Since the standard for discovery in particle physics is considered 5σ (and for evidence is typically 3σ) we clearly can cannot claim any evidence for new physics in our signal region, thus leading to the conclusion that we see no evidence for new physics in the exclusive $\gamma_{delayed} + \not{E}_T$ final state. Figure 7.4 shows the data minus background subtraction where the yellow and green bands represent the $\pm 1\sigma$ and 2σ uncertainties in the systematics and the error bars on the data points represent the statistical uncertainties. It is important to note here that a simplifying assumption of the errors being symmetric in the signal region and the control region was made. This is a safe overestimate of the uncertainties in the control region and does not significantly change the quoted $N_\sigma = 1.65$ of the remaining excess in the signal region.

With this in mind, in the next chapter we will explore how we understand the previous excess seen in 2008, describe how future versions of this analysis may gain sensitivity, and outline how to quanitfy our sensitivity to new physics models.

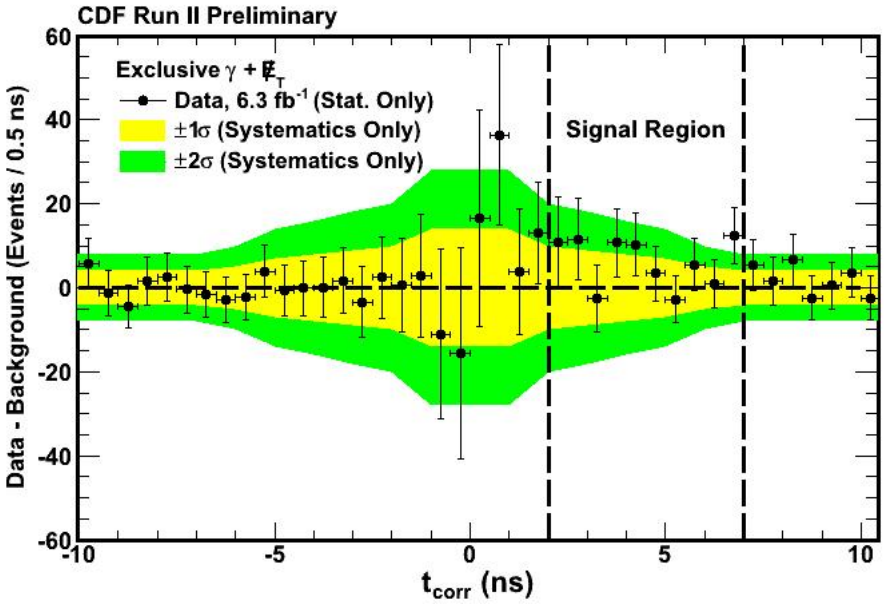

Fig. 7.4. The data minus background plot for the t_{corr} distribution where the yellow and green represent the $\pm 1\sigma$ and 2σ variation of the systematic and the error bars representing statistical error on the data. The events in the signal region correspond to a 1.65 σ excess taking into account all the statistical and systematic uncertainties.

8. CONCLUSIONS

8.1 Summary of the Search

This dissertation has presented a search for new physics in the exclusive $\gamma_{delayed}+\not\!\!E_T$ final state which was constructed to follow up on an intriguing excess that was observed in the same final state in early 2008. The candidate events were selected based on the corrected arrival time of the photon at the calorimeter as measured with the EMTiming system. The data sample analyzed represent data taken from December 2004 to June 2010 and corresponds to an integrated luminosity of 6.3 $\pm$0.4 fb^{-1}.

Using a data driven background prediction method we predict 257 $\pm$35 events expected in the timing region from 2 ns to 7 ns (signal region) and observe 322 events resulting in a modest excess remaining of observed minus predicted ($N_{Observed} - N_{Predicted}$) of 65 events. A quantitative estimate of the sensitivity to models amenable to GMSB SUSY scenarios where the $\tilde{\chi}_1^0$ has long enough lifetime to produce a delayed photon and assume that only $\tilde{\chi}_1^0$ pairs are produced in the final state will be done in the next generation of this analysis using the full Tevatron dataset of $\sim$10 fb$^{-1)}$.

8.2 Interpretation of the Data

We can calculate the significance of this excess as $N_\sigma = 1.65$ which gives a one sided p-value (the estimatied probability that this excess is inconsistent with a null hypothesis) of $\sim 5\%$, thus leading to the conclusion that we see no evidence for new physics in the exclusive $\gamma_{delayed} + \not\!\!E_T$ final state.

Since this search was performed in a quasi-model independent approach we do not set a direct cross-section limits on any one particular model. However, we do note that we anticipate that this search is sensitive to GMSB phenomenological models where $h^0 \rightarrow \tilde{\chi}_1^0\tilde{\chi}_1^0$ in Light Neutralino and Gravitino (LNG) models. In the LGN

models sparticle production is dominated by (h^0) events decaying to $\tilde{\chi}_1^0$ pairs, which is significantly different from those of the more conventional SPS-8 models which produce $\tilde{\chi}_1^0$ pairs at the end of long decay chains.

With this interpretation we make note that the modest excess of $N_\sigma = 1.65$ is present without any optimization for sensitivity to GMSB models. Instead this search was constructed to follow-up on the previous search performed in 2008 (see Section 1.5) and thus many of the analysis identification and selection variables were kept to be identical to the previous search. This was done to aid in the interpretation of the previous search which showed an excess of $\sim N_\sigma = 4$ using the previous background estimation technique which assumed a symmetric timing distribution as well as not including the rejection of many important sources of biased SM event production mechanisms. We arrive at the conclusion that the bulk of the previously seen excess was largely due to an incorrect background estimation assumption as well as various effects sculpting the timing distribution. Further detail on interpreting the previous result in light of the new result is given in Appendix C.

In the next section we address future prospects that can lead to a more sensitive search as well as a further exploration of the intriguing excess that remains in the exclusive $\gamma_{delayed}+\not{E}_T$ final state.

8.3 Future Prospects

A few areas that remain to be explored that could result in improving upon the analysis laid forth in this thesis include:

I) Reducing the systematic error on the wrong vertex mean

The largest systematic uncertainty on the number of background events in the signal region comes from the measurement of the wrong vertex mean using the no vertex sample. The Gaussian fit results in an uncertainty of ± 0.17 ns on the mean which in turn causes a $\pm$ 35 event uncertainty in our prediction.

We quickly describe a second method that has been explored [81] in order to reduce this uncertainty. This method utilizes a binned maximum likelihood fit of the data in the no vertex sample as well as in the control and bulk regions. The likelihood fit is performed over events with a vertex in the bins spanning $V \equiv t_{corr} \in$ [-7 ns, 2 ns] $\cup$ [20 ns, 80 ns], and event for events without a vertex in the bins spanning $N \equiv t^0_{corr} \in$ [-3 ns, 5 ns] $\cup$ [20 ns, 80 ns]. The likelihood function is defined as a product of Poisson probabilities over the bins of $V \cup N$ and Gaussian constraints assigned for each systematic uncertainty:

$$L = \{ \prod_{i \in V \cup U} \frac{\mu_i^{n_i} e^{-\mu_i}}{n_i!} \} \prod_c e^{\frac{-s_c^2}{2}} \tag{8.1}$$

where μ_i is the total expectation in the i-th bin, ni is the number of data events in the i-th bin, and S_c is a floating parameter associated with the systematic uncertainty c. In practice, it is the negative log likelihood that is minimized using the minuit program [82], which is equivalent to maximizing the likelihood.

This method of esitmating the wrong vertex mean is shown to reduce the overall uncertainty and thus improve our sensitivity to new physics. This method is explained in further detail in references [81] and [83]. We anticipate that this technique will reduce the uncertainty on the number of SM background events in the signal region by $\sim$30%. However, we cannot speculate on how it will affect the prediction of the mean value of the SM background prediction.

II) Reducing the cosmics ray background

The largest background in the exclusive $\gamma_{delayed} + \not{E}_T$ analysis remains events coming from cosmic ray events. We estimate a cosmic ray event rate of $\sim$32 events per nanosecond. This rate remains even after new optimized cuts on the photon candidates themselves, as were outlined in Section 4.2. One additional option that takes advantage of the fact that there is no true collision for cosmic ray backgrounds all vertices must be produced by unrelated min-bias collision.

Thus one way to reduce this background is to increase the ΣP_T required on reconstructed SpaceTime vertices. This would decrease the incidence of a cosmic ray occuring in coincidence with a reconstructed vertex and thus lower the overall cosmic ray rate. Additionally, this would increase the overall number of events which are classified as not reconstructing a vertex, giving more statistics to the no-vertex sample and thus reduce the uncertainty of the measurement of the wrong vertex mean.

An important caveat comes along with increasing the ΣP_T required on the SpaceTime vertex, namely the effect this could potentially have on a hypothetical signal. Thus a study would need to be performed on various signal models to determine what trade-off, if any, between sensitivity and rejection power can be made.

III) Optimizing event level cuts

As mentioned before, many of the event level selection requirements were kept the same in order to allow a comparison with the previously performed analysis. A study of optimizing the E_T and $\not\!\!E_T$ kinematic requirements as well as the optimizing E_T and P_T veto parameters may allow this search to extend its potential sensitivity to new phyiscs. We should note that the trigger we use in this analysis (see Section 2.4.1) allows us to move the E_T and $\not\!\!E_T$ thresholds down to 30 GeV. The previous reason for choosing an E_T cut of 45 GeV was to reduce the $W \to e\nu \to \gamma_{fake} + \not\!\!E_T$, but now that additional cuts already reduce this background we can consider lowering this cut. Additionally, moving away from the inflection point of the E_T spectrum (as discussed in Section 5.4.1) will help remove the bias from the $W \to e\nu$ background.

In conclusion, we have presented a search for new physics in exclusive$\gamma_{delayed} + \not\!\!E_T$ final state. We have used twice the data, multiple analysis improvements, and a better understanding of the backgrounds to follow up on a interesting hint in the

data. We have found that the majority of that excess was from previously unknown backgrounds, but a modest excess remains. With a clear view of potential new physics models, the rest of the Fermilab Tevatron data and potential improvements and optimization to a future analysis will either uncover a discovery or show that this was just one of the many statistical fluctuations that occur in collider experiments. Only time will tell.

REFERENCES

[1] S.Weinberg, *The Quantum Theory of Fields* (Cambridge Univ. Pr., Cambridge, UK, 1995-2000), Vol. 1-3.

[2] W.N. Cottingham and D.A. Greenwood *An Introduction to the Standard Model of Particle Physics* Second Edition (Cambridge Univ. Pr., Cambridge, UK 2007)

[3] W.M. Yao, *et al.*, [Particle Data Group], Journal of Physics G **33**, 1 (2006), and partial update for 2011.

[4] H.D. Politzer, *Asymptotic Freedom: An approach to strong interactions*, Phys. Rept., 14 (1974), pp. 129-180.

[5] D.J. Gross and F. Wilczek, *Asymptotically free gauge theories*, Phys Red., D8 (1973), pp. 3633-3652.

[6] S. Weinberg, *A model of leptons*, Phys. Rev. Lett., 19 (1967), pp. 1264-1266.

[7] A. Salam and J.C. Ward, *Electromagnetic and weak interactions*, Phys. Lett., 13 (1964).

[8] S.L. Glashow, *Partial Symmetries of weak interactions*, Nucl. Phys., 22 (1961).

[9] P. W. Higgs, Phys. Rev. Lett. **13**, 508 (1964), F. Englert and R. Brout, Phys. Rev. Lett. **13**, 321 (1964).

[10] International Masters Classes "Hands on Particle Physics", https://kjende.web.cern.ch/kjende/en/wpath/higgs.htm (accessed 2012).

[11] F. Halzen and A.D. Martin, *Quarks and Leptons: An Introductory Course in Modern Particle Physics*, John Wiley and Sons, 1984.

[12] Y. Fukunda et. al. (Super-Kamiokande Collaboration), Phys. Rev. Lett **81** (1998) pp. 1562-1587.

[13] G.W. Bennett, et. al., *Measurement of the Negative Muon Anomalous Magnetic Moment to 0.7 ppm* Phys. Rev. Lett. **92**, 161802 (2004)

[14] D. N. Spergel et al. (WMAP Collaboration), Astrophys. J. Suppl. **170**, 377 (2007); aarXiv:astro-ph/0603449

[15] G. Bertone, D. Hooper, and J. silk, Phys. Rept. **405**, 279 (2005); arXiv:hep-ph/0404175.

[16] M. Kaku, Introduction to Superstring and M-Theory, *Springer-Verlag* (2nd edition).

[17] S. Weinberg, Phys. Rev. D **13** 974 (1976), Phys. Rev. D **19**, 1277 (1979); E. Glidener, Phys. Rev. D **14** 1667 (1976); L. Susskind, Phys. Rev. D **20**, 2691 (1979).

[18] B. W. Lee, C. Quigg and H. B. Thacker, Phys. Rev. D 16, 1519 (1977).

[19] K. Nakamura et al. (Particle Data Group), J.Phys. G 37, 075021 (2010).

[20] Stephen P. Martin. A Supersymmetry Primer. 1997, hep-ph/9709356.

[21] H. P. Nilles, Phys. Rept. 110, 1 (1984).

[22] H. E. Haber and G. L. Kane, Phys. Rept. 117, 75 (1985).

[23] S. Dawson. The MSSM and Why it Works. 1997, hep-ph/9712464.

[24] S. Dawson, Nucl. Phys. B 261, 297 (1985).

[25] H. K. Dreiner, An introduction to explicit R-parity violation, hep-ph/9707435.

[26] P. Fileviez Perez and S. Spinner, Spontaneous R-Parity Breaking in SUSY Models, arXiv:0904.2213.

[27] L. Hall, J. Lykken and S. Weinberg, Phys. Rev. D 27, 2359 (1983).

[28] L. Alvarez-Gaume, J. Polchinski, and M. Wise, Minimal Low-Energy Supergravity, Nucl. Phys. B221 (1983) 495.

[29] A. Chamseddine, R. Arnowitt, and P. Nath, Locally Supersymmetric Grand Unication, Phys. Rev. Lett. 49 (1982) 970.

[30] G.F. Giudice and R. Rattazzi. CERN-TH-97-380, hep-ph/9801271 (1998).

[31] M. Dine and A. Nelson, Dynamical supersymmetry breaking at low-energies, Phys. Rev. D48 (1993) 1277, hep-ph/9303230.

[32] M. Dine, A. Nelson, and Y. Shirman, Low-energy dynamical supersymmetry breaking simplfied, Phys. Rev. D51 (1995) 1362, hep-ph/9408384.

[33] N. Vittorio and J. Silk, Astrophys. Journal, Part 2-Letters to the Editor 285, L39-L43 (1984).

[34] P. Bode, J. Ostriker and N. Turok, Astrophys. J. 556, 93 (2001).

[35] J. L. Feng and T. Moroi, Phys. Rev. D 58, 035001 (1998).

[36] B. C. Allanach et al., in Proc. of the APS/DPF/DPB Summer Study on the Future of Particle Physics (Snowmass 2001) ed. N. Graf, Eur. Phys. J. C 25 (2002) 113.

[37] D. A. Toback and P. Wagner, Phys. Rev. D 70 (2004) 114032.

[38] LEP SUSY Working Group, ALEPH, DELPHI, L3, and OPAL Collaborations, LEPSUSYWG/04-09.1 (http://lepsusy.web.cern.ch); A. Heister et al. [ALEPH Collaboration], "Search for gauge mediated SUSY breaking topologies in e+e^- collisions at center-of-mass energies up to 209 GeV," Eur. Phys. J. C 25 (2002) 339 [arXiv:hep-ex/0203024]; M. Gataullin, S. Rosier, L. Xia and H. Yang, "Searches for gauge-mediated SUSY breaking topologies with the L3 detector

at LEP," AIP Conf. Proc. 903, 217 (2007) [arXiv:hep-ex/0611010]; G. Pasztor, "Search for gauginos and gauge mediated SUSY breaking scenarios at LEP," PoS 46 HEP2005, 346 (2006) [arXiv:hep-ex/0512054]; J. Abdallah et al. [DELPHI Collaboration], "Search for one large extra dimension with the DELPHI detector at LEP," Eur. Phys. J. C 60 (2009) 17 [arXiv:0901.4486 [hep-ex]].

[39] B. Abbott et al. [D0 Collaboration], "Experimental search for chargino and neutralino production via gauge mediated supersymmetry breaking models," Phys. Rev. Lett. 80 (1998) 442, [arXiv:hep-ex/9708005]; F. Abe et al. [CDF Collaboration], "Searches for new physics in diphoton events in $p\bar{p}$ collisions at $\sqrt{s} = 1.8$ TeV," Phys. Rev. Lett. 81 (1998) 1791, [arXiv:hep-ex/9801019]; F. Abe et al. [CDF Collaboration], "Searches for new physics in diphoton events in $p\bar{p}$ collisions at $\sqrt{s} = 1.8$ TeV," Phys. Rev. D 59 (1999) 092002, [arXiv:hepex/9806034]; V. M. Abazov et al. [D0 Collaboration], "Search for supersymmetry with gauge-mediated breaking in diphoton events at D0," Phys. Rev. Lett. 94 (2005) 041801, [arXiv:hep-ex/0408146]; T. Aaltonen et al. [CDF Collaboration], "Search for Supersymmetry with Gauge-Mediated Breaking in Diphoton Events with Missing Transverse Energy at CDF II," Phys. Rev. Lett. 104 (2010) 011801, [arXiv:0910.3606 [hep-ex]]; V. M. Abazov et al. [D0 Collaboration], "Search for dark photons from supersymmetric hidden valleys," Phys. Rev. Lett. 103 (2009) 081902, [arxiv:hep-ex/0905.1478v2].

[40] V. M. Abazov et al. [D0 Collaboration], "Search for Diphoton Events with Large Missing Transverse Energy in 6.3 fb^{-1} of $p\bar{p}$ collisions at $\sqrt{s} = 1.96$ TeV," Phys. Rev. Lett. 105 (2010) 221802, [arXiv:hep-ex/1008.2133]

[41] G. Aad et al. [ATLAS Collaboration], "Search for Diphoton Events with Large Missing Transverse Energy in 7 TeV Proton-Proton Collisions with the ATLAS Detector," arXiv:1012.4272 [hep-ex]; S. Chatrchyan et al. [CMS Collaboration], "Search for Supersymmetry in pp Collisions at $\sqrt{s} = 7$ TeV in Events with Two Photons and Missing Transverse Energy," [arXiv:hep-ex/1103.0953] submitted to Phys. Rev. Lett.

[42] T. Aaltonen et al. [CDF Collaboration], "Search for Heavy, Long-Lived Neutralinos that Decay to Photons at CDF II Using Photon Timing," Phys. Rev. D 78 (2008) 032015, [arXiv:0804.1043 [hep-ex]]; A. Abulencia et al. [CDF Collaboration], "Search for heavy, long-lived particles that decay to photons at CDF II," Phys. Rev. Lett. 99 (2007) 121801, [arXiv:0704.0760 [hep-ex]].

[43] J. D. Mason and D. Toback, "Prospects of Searches for Gauge Mediated Supersymmetry with $h^0 \to \tilde{\chi}_1^0\tilde{\chi}_1^0$ production in the Time-Delayed Photon + MET Final State at the Tevatron" Phys. Lett. B 702, 377 (2011) [arXiv:1105.2194 [hep-ph]].

[44] S. Dimopoulos, M. Dine, S. Raby, S. D. Thomas, Phys. Rev. Lett. 76, 3494-3497 (1996).

[45] For a description of beam halo and cosmic ray backgrounds see R. Tesarek, CDF Report No. CDF-NOTE-5873 (2002) and P. Onyisi, CDF Report No. CDF-NOTE-6009 (2003), M. Goncharov et al., CDF Report No. CDF-NOTE-8409 (2006), all unpublished.

[46] D. Stentz Measurement of the Cross Section for W Boson Production in Association with Jets, CDF NOTE 10294 (2010), unpublished

[47] R. Culbertson, A. Pronko, Shin-Shan Eiko Yu CDF NOTE 8220 (2006), unpublished

[48] T. K. Gaisser, Cosmic Rays and Particle Physics, Cambridge University Press, 1990

[49] Bartol Research Institute, "Cosmic Rays and Earth", http://http://neutronm.bartol.udel.edu/catch/cr2.html (accessed 2012).

[50] N. Mokhov, J.Annala, R. Carrigan, et. al "Tevatron beam halo collimation system: design, operational experience and new methods" JINST 6 T08005 (2011).

[51] R. Thurman-Keup, C. Bhat, W. Blokland, et. al "Longitudinal bunch monitoring at the Fermilab Tevatron and Main Injector synchrotrons" JINST 6 T10004 (2011).

[52] T. Appelquist, H. C. Cheng and B. A. Dobrescu, "Bounds on Universal Extra Dimensions" Phys. Rev. D 64 (2001) 035002, [arXiv:hep-ph/0012100v2]; H. C. Cheng, J. L. Feng, K. T. Matchev, "Kaluza-Klein dark matter" Phys. Rev. Lett. 89 (2002) 211301, [arXiv:hep-ph/0207125v2]; G. Servant and T. M. P. Tait, "Is the lightest Kaluza-Klein particle a viable dark matter candidate?," Nucl. Phys. B 650 (2003) 391, [arXiv:hep-ph/0206071].

[53] T. Aaltonen et al. "Search for large extra dimensions in final states containing on photon or jet and large missing transverse energy produced in $p\bar{p}$ collisions at $\sqrt{s} = 1.96$ TeV" Phys. Rev. Lett. 101:181602, 2008.

[54] Tevatron Accelerator Division, "Operations Rookie Books," http://wwwbdnew.fnal.gov/operations/rookie books/rbooks.html.

[55] Fermilab Beams Division, Run II Handbook (1998), http://wwwbd.fnal.gov/runII/index.html.

[56] CDF Run IIb Technical Documents, http://www-cdf.fnal.gov/run2b.html (accessed 2012).

[57] C. S. Hill et al. (CDF Collaboration), Nucl. Instrum. Meth. A 530, 1 (2004); A. Sill et al. (CDF Collaboration), Nucl. Instrum. Meth. A 447, 1 (2000).

[58] M. Goncharov, et al. "The Timing System for the CDF Electromagnetic Calorimeters" Nucl.Instrum.Meth. A563, 543 (2006).

[59] R. Blair et al: (CDF Collaboration), Fermilab Report No. FERMILAB-PUB-96-390-E.

[60] G. Gomez-Ceballos et al., Nucl. Instrum. Meth. A 518, 522 (2004).

[61] P. Onyisi, CDF Report No. CDF-NOTE-6381 (2003), unpublished.

[62] M. Goncharov, V. Krutelyov, D. Toback, and P. Wagner, "Space-Time Vertex Reconstruction Using COT Tracks", CDF Note 8015, unpublished.

[63] K. Bloom, Started with CDF Run 2 Offline", CDF Note 5294 Unpublished.

[64] http://www-cdf.fnal.gov/internal/physics/photon/docs/goodrun_v36_pho_00.txt.

[65] A. Bhatti et al., Nucl. Instrum. Meth. A 566, 375 (2006); arXiv:hep-ex/0510047.

[66] D. Toback, Ph.D. thesis, University of Chicago, FERMILAB-THESIS-1997-36 (1997); J. Berryhill, Ph.D. thesis, University of Chicago, FERMILAB-THESIS-2000-02 (2000); Y. Liu, Ph.D. thesis, Universite de Gen'eve, FERMILAB-THESIS-2004-37 (2004).

[67] Sunil Somalwar Sourabh Dube, John Zhou. Medium E_T Electron Identification Efficiency and Scale-Factors. CDF Note 8321, unpublished.

[68] T. Muller et al., CDF Report No. CDF-NOTE-6047 (2003), unpublished; J. F. Arguin, B. Heinemann and A. Yagil, CDF Report No. CDF-NOTE-6238 (2003), unpublished.

[69] M. Martens and P. Bagley, "Luminosity Distribution During Collider Run II" http://wwwap.fnal.gov/∼martens/luminosity/beam size.html.

[70] J.Asaadi, R. Moore, D. Toback. "Tevatron Timing and z Collision Distributions for use in the Delayed Photon Analysis", CDF NOTE 9812 (2009), unpublished.

[71] G. Ascoli et al. (CDF Collaboration), Nucl. Instrum. Meth. A 268, 33 (1988).

[72] S. D'Auria et al., CDF Report No. CDF-NOTE-7055 (2004), unpublished.

[73] T. Sjostrand et al., Comput. Phys. Commun. 135, 238 (2001). We use version 6.216.

[74] R. Brun et al. GEANT 3 Manual, CERN Program Library Long Writeup. 1994, W5013.

[75] D. Toback and P. Wagner "Simulation of the Calorimeter Timing System for the CDF Detector", CDF-NOTE-5866 (2001), unpublished.

[76] S. Klimenko, J. Konigsberg, A. Madorsky, A. Nomerotski, A. Safonov, D. Tsybychev, S. Wang "CLC Calibrations", CDF-NOTE-5548 (2001), unpublished. Gervasio Gomez, Matthew Jones, Jaison Lee, Youngdo Oh, Ivan Vila "Online Calibrations of the CDF-II Time-of-Flight Detector", CDF-NOTE-6050 (2002), unpublished. Ben Cooper, Dustin McGivern, Rob Snihur "Coordination of CDF Offline Calibrations", CDF-NOTE-6817 (2003), unpublished. Stefano Giagu "COT dE/dx Calibrations for 0d/0h datasets" CDF-NOTE-8144 (2006).

[77] T. Nelson, R. Snider, D. Stuart, "Forward Electron Tracking with the Phoenix-Mods Package," CDF Note 6278 (2003), unpublished.

[78] Jonathan Asaadi, Adam Aurisano, Daniel Goldin, Jason Nett, David Toback, "Rejecting $e \to \gamma_{fake}$ Candidates With Loose Track Matching" CDF-NOTE-10773 (2012).

[79] Carsten Rott, Daniela Bortoletto, "Primary Vertex Algorithm Comparison for High P_T Physics", CDF Note 6472 (2003), unpublished.

[80] Lozier, Daniel M.; Boisvert, Ronald F. et al., NIST Handbook of Mathematical Functions, Cambridge University Press, ISBN 978-0521192255, MR2723248

[81] Jonathan Asaadi, Adam Aurisano, Daniel Goldin, Jason Nett, David Toback, "The Search For New Physics in the $\gamma_{delayed} + \not\!\!E_T$ Signature in p-$\bar{p}$ Collisions at $\sqrt{s} = 1.96$ TeV" CDF-NOTE-10789 (2012) (To be submitted to PRL).

[82] F. James and M. Roos, Comput. Phys. Commun. 10, 343 (1975).

[83] Jonathan Asaadi, Adam Aurisano, Daniel Goldin, Jason Nett, David Toback, "Backgrounds and Estimation Methods for the Search for New Physics in the Exclusive $\gamma_{delayed} + \not\!\!E_T$ Final State" CDF-NOTE-9924 (2012).

[84] T. Affolder et al. (CDF Collaboration), Phys. Rev. D 64, 032001 (2001), T. Abe et al. (CDF Collaboration), Phys. Rev. Lett. 68, 1104 (1992).

APPENDIX A

DEFINITIONS OF THE VARIABLES USED IN OBJECT IDENTIFICATION

In this appendix we provide a more complete description of the various particle ID objects reconstructed at CDF and used in the exclusive $\gamma_{delayed} + \not\!\!E_T$ analysis. Since these are discussed in detail elsewhere ([56, 62, 66, 67]) and have been used for years at CDF, we only summarize them here. We begin by outlining the most generic object, a deposition of energy found in the calorimeter, known as a "cluster", which is used both for creating jets, photons, and electrons. Next we define the varialbes used for charged particles as they pass through the various tracking subsystems known as tracks. Then we describe the algorithm by which we cluster together tracks to identify the origin of the collision point in space and time, known as a SpaceTime vertex. From here we distinguish between the jet objects photons and electrons using the additional object identification and track information. Then finally we describe the measurement of the energy imbalance in the detector known as missing energy ($\not\!\!E_T$).

A.1 Jets

The term "jets" typically refers to the hadronization of a high energy quark or gluon that is produced in the collision. Since at CDF jets are identified as clusters

of energy in the calorimeter, pions from the hadronic decays of taus and the energy deposits from electrons and photons are also reconstructed as "jets".

Jets are first identified by looking for energetic "seed" towers which are a deposition energy in a physical tower. Additional towers within a radius in $\eta - \phi$ space defined as $R = \sqrt{(\Delta\eta)^2 + (\Delta\phi)^2}$ are then added to the jet and a new jet center is calculated using a weighted average of every tower in the jet. This process is then repeated until the jet no longer changes and overlapping jets are merged if two jets overlap by >50%. Below we define the variables used in the CDF jet algorithm referred to in Section 2.4

- R**: Standard Jet Search-Cone radius**

  Jets are identified as clusters of energy in the calorimeter within a search-cone in η-ϕ space of radius 0.4.

- E_T^0**: Jet Transverse Energy**

  The jet E_T^0 is defined as E x $sin\theta$ where E is the energy of all the calorimeter towers in the cone and θ is calculated from $z = 0$ cm to the z position of the centroid of the jet in the calorimeter.

- **Seed Tower**

  Any single tower in the calorimeter with E_T >1 GeV may be used as the "seed" tower for calculating the centroid of a jet.

- η: **Pseudorapidity**

Spatial coordinate describing the angle of a jet/particle relative to the beam line. This quantity was defined in Equation 2.2.

The goal of the process of searching for towers with a radius in $\eta - \phi$ space and creating "jets" is to determine the energy of the particle that produced the jet. While not widely used in this analysis, we define the standard corrections applied to the "jet" cluster for completness. These include:

- **Relative Energy Correction**

  This correction takes into account calorimeter response and gaps in the intrumentation of the detector. A systematic uncertantiy is taken from the differnce of two jet events which occur back to back (known as dijet balancing) [84].

- **Correcting for pile-up**

  Energy from collisions where there were multiple interactions in the same event cause the jet E_T to be over measured. Thus a correction using the average value of the E_T as a function of the number of verticies is applied to parametrize this correction [65].

- **Absolute Energy Scale**

  The response of the calorimeter does not exactly reflect the energy of the original particles in the jet object. This comes from our ability to simulate the calorimeter response to a single particle which introduces a 3% uncertainty and the differences in how we model hadronization which accounts for a 1% uncertainty.

- **Out-of-Cone Energy**

  Jets often deposit some fraction of their energy outside the radius of the cone in $\eta - \phi$ space and thus need their energy corrected for this fact. While this effect is corrected on average, a systematic uncertainty is taken to be the difference between simulation and data which is $\sim$5% [84].

A.2 Tracks

As a charged particle traverses through the SVX and COT systems energy is deposited in these subsystems in the form of hits. Since these systems are in a magnetic field tracks are reconstructed using helical pattern recognition algorithms on those hits. Hits are combined to reduce problems from 'fake' hits as well as achieve better resolution on the position and time of the hit. First small groupings of hits ("stubs") are formed from the individual hits in the 12 layers in each superlayer in the COT and then the stubs are linked together using a fit to a five degree helix to form tracks. The helix is defined by its curvature $C = q/2R$, where R is the radius of the helix $x - y$ projection and q is the charge of the particle. When the SVX tracking information is available this improves the overall track resolution and allows a more robust 3D pattern recognition in COT and SVX to be linked together to extract the best fit value possible.

Below are the various definitions for the track related parameters used in section 2.4.

- P_T: **Beam Constrained Track Momentum**

  This is a tracks transverse momentum which is corrected for the spatial location of the beam to include the track resolution.

- $COTStereoSeg(5)$: **Number of COT Stereo Segments with 5 or more Hits**

  The superlayers of the Central Outer Tracker are radial subdivisions of the COT wires. There are four axial superlayers and four stereo superlayers, of which we require a stereo superlayer to have five or more hits in the wires associated with the track. Requiring this helps insure enough hits in the tracker to have an accurate timing measurement.

- $COTAxialSeg(5)$: **Number of COT Axial Segments with 5 or more Hits**

  We require an axial superlayer to have five or more hits in the wires associated with the track. Requiring this helps insure enough hits in the tracker to have an accurate timing measurement.

- Z: **Z Position**

  This variable defines where along the direction of the beam the track originates from. We require these tracks to have come from a $|z|$ <70 cm to help insure the tracks origin comes from the best instrumented part of the detector and help insure a quality track used in the timing measurement.

- d_0: **Corrected Impact Parameter**

This is a measurement of the tracks impact parameter (distance of closest approach) corrected for the spatial location of the beam position. Requiring this variable insures that you are calibrating tracks that come from the beam line as opposed to secondary decays or tracks created from the interactions with detector material.

- T_0 σ: **Track Time Uncertainty**

  This is the error associated with the track time measurement based on the spread of hits in the COT.

A.3 Verticies

The SpaceTime vertex reconstruction algorithm uses COT tracks and has been developed to measure the time and position at which the collision occurs. While existing vertexing algorithms [69] have been shown to reconstruct the vertex position (z_0) with a high degree of accuracy, it is important to be able to separate one vertex from another vertex that lies close in space but happens at a different initial time (t_0). For this purpose a custom SpaceTime vertexing algorithm begins by considering only tracks that have a well measured time. This is a trade-off of efficiency for finding a vertex with the quality of the reconstructed collision time which is used in the photon timing variables of particular importance in this thesis. Since this algorithm has been in use for many years it this algorithm is described in more detail in Ref [62].

In brief, the SpaceTime vertex algorithm starts by taking the highest p_T track becomes a "seed" of a "cluster" of tracks that lower P_T tracks are assigned to if they lie three times the RMS of the cluster defined as 0.6 ns for t_0 and 1.0 cm for z_0. From the remaining set of tracks, the next highest P_T track is then picked as the next seed and tracks are assigned to it, and so forth until no tracks are left. An iterative procedure does a fit of the parameters of the vertex to determine the best value of the mean and RMS of z and t_0, and then varies the parameters of all clusters simultaneously at each iteration step n, such that it maximizes the probability that all tracks belong to a set of clusters with parameters, equivalent to a likelihood fit. If during this process two clusters are within both 3 cm in z and 1.8 ns in t the two clusters are merged. All these procedures are iterated until the variation becomes less then one percent.

Below is a summary of the variables we use to identify a "good" SpaceTime vertex for use in our analysis. These variables are created for each vertex found, and we select the primary vertex based on these variables as described in Section 2.4.

- ΣP_T: **Vertex Sum Transverse Momentum**

  This variable is the sum of all tracks P_T associated with the SpaceTime vertex.

- N_{track}: **Number of Tracks**

  Number of tracks associated with the SpaceTime Vertex.

- Z: **Z Vertex Position**

  The mean Z position of all the tracks associated with SpaceTime Vertex.

A.4 Photons

Photons at CDF are identified as an energy deposits in up to three calorimeter towers in η and one tower in ϕ where the seed tower exceeds 3 GeV. Additionally we require a matching cluster of energy in the CES in the same seed tower that is used to determine the position of the photon. In order for a photon candidate to be considered in the analysis, we require that it be deposited in the well instrumented ("fiducial") region of the detector where the calorimeter is likely to have made a good measurement. This region is defined as near the center of each tower, within 21 cm of the tower center in $r-\phi$ ($|X_{CES}|$ <21 cm) and in z is 9< $|Z_{CES}|$ <230 cm. The CDF detector has been used to accurately identify and measure high energy photons for over 25 years using well established identification requirements [66]. For this analysis we only consider photons found in the central part of the detector ($|\eta|$ <1.0). This is due to the fact that the central region is not only better instrumented, with the full set of tracking chambers, but the EMTiming system has been fully calibrated and validated in this region.

Below is the definition of the various variables used to identify photons at CDF discussed in section 2.4.

- **E_T^0: Photon Transverse Energy**

  The photon (or electron) E_T^0 is defined as E x $sin\theta$ where E is the energy of the electromagnetic cluster and θ is calculated from $z = 0$ cm to the z position in the central electromagnetic shower (CES).

- **Fiducial**

  The fiducial region is defined in terms of the Central Electromagnetic Shower Maximum detector and is set in order to avoid inactive regions of the detector.

- $\frac{HadronicEnergy}{ElectromagneticEnergy}$: **Hadronic Leakage**

  Photons (Electrons) leave most of their energy in the electromagnetic portion of the calorimeter. The ratio of energy deposited in the hadronic part of calorimeter towers in the cluster to that in the electromagnetic part helps separate photons (electrons) from jet backgrounds.

- **Energy Isolation**

$$Isolation = \frac{E_T^{cone} - E_T^{cluster}}{E_T^{cluster}} \tag{A.1}$$

  The photon (electron) isolation in the calorimeter is defined by Equation A.1 where $E_{T\,cone}$ is the sum of the transverse energy in both the electromagnetic and hadronic calorimeters in the towers adjacent within a radius of $R = \sqrt{\Delta\phi^2 + \Delta\eta^2} = 0.4$ and $E_{T\,cluster}$ is the transverse electromagnetic energy.

- **Track Isolation**

  We require photons to be isolated from tracks that appear in the tracking chamber. The ΣP_T of all tracks within a cone of $R = \sqrt{\Delta\phi^2 + \Delta\eta^2} = 0.4$ around the photon tower is required to be less than 2 GeV/c, but becomes less restrictive as the photon E_T becomes larger in order to retain overall efficiency.

- **N3D Track Rejection**

  In order to distinguish between electrons and photons, whose showers look almost identical in the calorimeter, we reject any photon candidate if a track of certain quality (N3D) with P_t >1 GeV/c points to the electromagnetic cluster in the calorimeter. To further clarify, a N3D track is any track that contains readout coming from both the silicon and COT tracking system with P_t >0.3 GeV/c.

- **2^{nd} CES Cluster Energy**

  In order to reject photons that are due to $\pi^0 \rightarrow \gamma\gamma$ decay, we reject the photon candidate if there is a second photon that can be identified in the Central Electron Strips (CES) detector. The CES of the photon candidate tower is searched for a second cluster with energy greater than 2.4 GeV/c and becomes less restrictive as the E_T becomes larger.

- **PMT Aysmmetry**

  This particular requirement is not a standard photon requirement, but has been used in previous photon analysis [**?**, 39, 42]. In the Central Electromagnetic Calorimeter (CEM) an energy deposit is identified from the output of the two photo-multiplier tubes (PMTs) that collect the light from the scintillator in the CEM. A high voltage breakdown in the PMT unrelated to an energy deposit in the CEM and can create a false electron candidate if this happens to correspond with an unrelated collision track. Since photons (electrons) that come from the collision will deposit nearly the same amount of energy in each PMT, these

instrumental effects can be separated by considering the asymmetry of the two energy measurement of the PMT from the two PMTs from a tower as shown in Equation A.2.

$$PMTAysmmetry = \frac{|E_{PMT1} - E_{PMT2}|}{E_{PMT1} + E_{PMT2}} \tag{A.2}$$

- **EMTiming System Readout**

  Requiring that the EMTiming system has a reasonable readout associated with the arrival of the photon (electron) is necessary since we will use this information for calibrations.

A.5 Electrons

At CDF we identify an electron candidate by using Information about electron shower position and profile is determined by looking at the point of the largest showering in the CES and fitting the shape position of CES clusters. Unlike the case of a photon where we explicitly require there to be no track associated, if a calorimeter cluster can be matched to a track we call this an electron candidate. The calorimeter clusters may combine up to two CEM towers adjacent in η. This is done because electrons deposit their energy in a small region of the calorimeter and tend to deposit almost all their energy in EM calorimeter. Correspondingly, the hadronic towers should carry less then 0.125 GeV of the EM tower energy.

The similarity between the electron clusters and the photon cluster allow us to use the electron sample as a testing place for much of our photon analysis. This is possible if we simply ignore the information gained from the electron track and thus essentially treat the electron candidate as a photon. However, we can recover information about the origin of the electron, unlike a photon which has no track, and thus help refine various initial time and position assumptions.

Below is a list of variables used to identify electrons at CDF and referred to in Section 2.4.

P_T: Beam Constrained Track Momentum

The highest P_t track which extrapolates to the electromagnetic cluster is considered to be associated with the cluster. This track is adjusted then corrected for the the spatial location of the beam to improve the track resolution.

ΔX and ΔZ CES Track Shower Matching

By extrapolating the electron track to the cluster in the CES ΔX is the seperation in the $r - \phi$ plane and ΔZ is the corresponding seperation the the z view. These variables are defined as:

$$\Delta X = X_{track} - X_{CES} \tag{A.3}$$

$$\Delta Z = Z_{track} - Z_{CES} \tag{A.4}$$

E/P

The ratio of the energy to the momentum of the highest P_t track pointing to the electromagnetic cluster.

L_{shr}: **L-Share**

L-Share (Laterial Sharing) is a measure of the transverese profile of the electromagnetic shower shape and the comparison of the lateral sharing of energy in the calorimeter towers of the electron cluster. L_{shr} is defined as:

$$L_{shr} = 0.14 \sum_i \frac{E_i^{adj} - E_i^{prob}}{\sqrt{0.14^2 E + (\Delta E_i^{prob})^2}} \tag{A.5}$$

where E_i^{adj} is the energy in the tower adjacent to the tower of the electron, E_i^{prob} is the expected energy in an adjacent tower calculated from text beam data, and $0.14^2 E$ is the error associated with the energy measurement.

A.6 Missing Transverse Energy

In $p\bar{p}$ interactions at the Tevatron collider the collision occurs with approximately no momentum in the plane transverse to the collision. Therefore, by conservation of momentum, the vector sum of the transverse momenta of the inital state particles should be approximately zero. Particles that do not interact with the calorimeter, such as neutrinos, can be inferred from the transverse energy imbalance of the detected particles in the collision. The measured missing transverse energy, $\not\!\!E_T$, is defined as the negative of the vector sum of the transverse energy measured in all

calorimeter towers with $|\eta|$ <3.6. To improve the resolution, and to reduce the number of events with large fake missing energy, $\not\!\!E_{T\,fake}$, the $\not\!\!E_T$ is corrected to account for the detector response for reconstructed jets with $E_T > 15$ GeV.

It is also important to note that there are collision and non-collision sources of missing energy. SM neutrinos leave the detector and can produce a significant amount of real $\not\!\!E_T$. Meanwhile, non-collision source cannot be expected to conserve transverse energy necessarily and thus become a source of $\not\!\!E_T$ in our events. In some sense this $\not\!\!E_T$ is fake since it is not produced in the collision, but it may be considered as real in the sense that it is not due to a mismeasurement of the energy deposited. Additionally, mismeasurements of deposits of energy in jets, photons, electrons, muons, etc, can give the appearance of $\not\!\!E_T$ in the detector. These are commonly referred to as "fake" missing energy. Since large fake $\not\!\!E_T$ from energy fluctuation are rare we consider this to be negligible in this analysis.

APPENDIX B

ADDITIONAL MATERIAL FOR COSMIC RAY REJECTION

In this appendix we provide additional supporting material to help further explain the selection criteria used to reduce the number of events coming from cosmic ray sources in the exclusive $\gamma_{delayed}$+$\not\!\!E_T$ final state. Recall that cosmic rays are, in general, charged particles that originate in outer space and then interact with the earth's atmosphere producing secondary particles that then shower down to the Earth's surface. If a cosmic ray happens to deposit energy in the detector, in particular the EM calorimeter, it can mimic a photon candidate signature (i.e., an energy deposit in the EM calorimeter only and no track pointing to it in from the tracking chamber). If this deposit occurs in coincidence with a collision in the detector this can lead to both an incorrectly assigned photon to a vertex that had nothing to do with its production as well as leaving an imbalance of energy in the detector which is misidentified as missing energy. This mis-identification of a photon can occur if the cosmic ray produces an electromagnetic cluster via a bremsstrahlung interaction or a catastrophic showering within the EM calorimeter. While only a small fraction of cosmic ray collision fake the photon signature, the sheer number of them make them a significant background in our search. However, there are a number of features which allow us to separate photons from cosmic ray sources from physics sources. What makes this task particularly difficult is that we are trying to identify photons

from a heavy neutral particle which is also slightly different from a photon produced directly in the collision, and travels directly from the calorimeter face. The distinct topology of a cosmic ray event allows us to develop a series of cuts to help veto against mis-identifying an EM cluster from a cosmic ray event.

B.1 Muon Stub Cosmic Ray Rejection

Since the bulk of the particles that will traverse down to the detector are muons, we focus on these as the dominant source of cosmics rays. Using the 'outside-in' topology of the majority cosmic ray events, we look to the muon detector which is on the outside radius of the CDF detector for activity which corresponds to the electromagnetic shower we see in the calorimeter. The muon system is a series of 4 layer single wire proportional drift chamber. The muon chambers are filled with a 50-50 mix of Agron-Ethane gas and atmospheric pressure and have a drift time of $\sim 1\mu s$. The system provides a resolution of ~ 0.6 mm in $r-\phi$ direction and about 10 cm in the z direction with nearly 100% hit efficiency [71]. A schematic of the muon systems of the CDF detector is shown in Figure B.1.

When a muon passes through this system it creates a series of "hits" that are then identified as a "muon-stub". For collision based-muons, if there is a track pointing to a muon-stub this is identified as a collision muon. For cosmic rays you will often have a muon-stub which lies within a close angle to the cluster found in the electromagnetic calorimeter and no track present. Therefore, if there is a muon stub

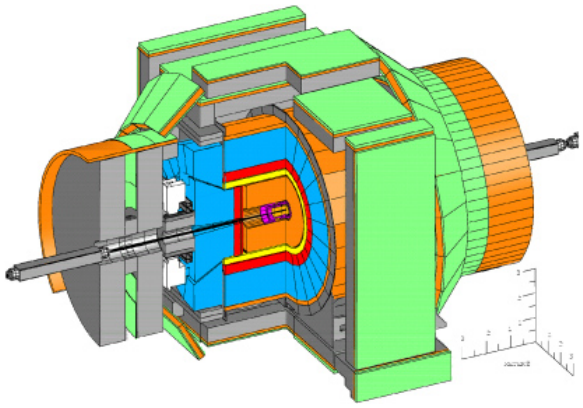

Fig. B.1. Schematic view of the CDF detector where the muon detection system is highlighted in green. These muon detectors allow us to distinguish cosmic rays which originate outside the detector and pass through the muon detectors and may be incorrectly identified as a photon.

within a $|\Delta\phi|$ <30 degrees we veto that event as likely having come from a cosmic ray. The muon-stub veto used to reject photon events coming from cosmic rays has been used at CDF and in previous delayed photon searches with great success [42,45].

In addition to this cut we develop two more cosmic rejection cuts that also take advantage of the unique topology of a cosmic ray event originating from outside the detector and propagating inwards. These cuts are added to the photon identification as was discussed in Section 2.4.

B.2 Hadronic Energy Fraction Selection Criteria for Cosmics Rays

The first of these is a "sliding" cut on the amount of energy we find in the hadronic calorimeter as a function of E_T. Specifically, we expect high energy photons to end up showering through the electromagnetic calorimeter and leaving some small fraction of

their energy in the hadronic calorimeter. However, cosmic ray photons resulting from bremsstrahlung interactions or a catastrophic collision in the EM calorimeter will leave very little energy in the hadronic calorimeter. The hadronic energy distribution can be seen in Figure B.2 where we compare cosmic ray photons selected using the exclusive γ+$\not\!\!E_T$ presample defined in Table 2.12 to electrons selected using the exclusive e+$\not\!\!E_T$ sample defined in Table 2.11. The cosmic ray photons are identified by reversing the muon-stub veto and looking in the timing window from 20 ns to 80 ns as was outlined in Section 4.2. Specifically, you can see a great deal more hadronic energy is deposited by high energy electrons then cosmic ray photons.

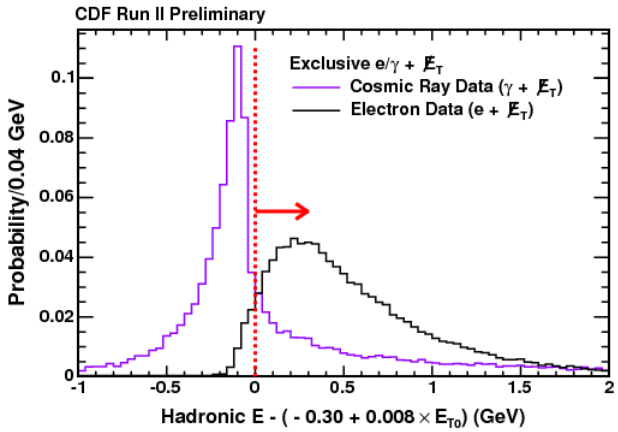

Fig. B.2. Hadronic energy distribution for electrons coming from collisions (black line) as well as the hadronic energy distribution coming from cosmic ray photons (pink line) identified using by reversing the muon-stub veto. We note that high energy objects coming from the collision deposit more energy in the hadronic calorimeter then minimum ionizing events like cosmic rays.

B.3 Central Electromagnetic Shower Energy Fraction Selection Criteria for Cosmics Rays

An additional requirement to help reject cosmic ray backgrounds takes advantage of the fact that comic rays photons will deposit very small fraction of their total energy in the Central Electromagnetic Shower detector (CES) when compared to the total energy in the all the calorimeters. Cosmic rays deposit such a low fraction of their energy in the CES because of the way the bremsstrahlung interactions or a catastrophic collision in the EM calorimeter develop their showers. Namely, cosmic rays will shower in a direction pointed away from the CES while collision based showers develop into the CES. Therefore, we expect cosmic ray showers to have a small fraction of their total measured energy to be present in the CES. Thus we use the fraction of CES energy over the total energy to help distinguish from high energy collision photons and photons coming from cosmic rays ($\frac{CES(E)}{TotalE}$). How the fraction of energy in the CES over the total energy for identified cosmic rays versus electrons coming from a collision is shown in Figure B.3 and suggests a cut of ~ 0.2.

As shown in Figure B.4, when we make a cut $\frac{CES(E)}{TotalE} > 0.2$ in addition to the Hadronic Energy sliding cut we have an overall 92% efficiency for a 76% rejection of cosmic ray photons. These cuts are shown to help reduce the dominant background of cosmic rays in the exclusive $\gamma_{delayed}+ \not\!\!E_T$ sample of 3/4 when compared to the cosmics rates estimated before using these cuts.

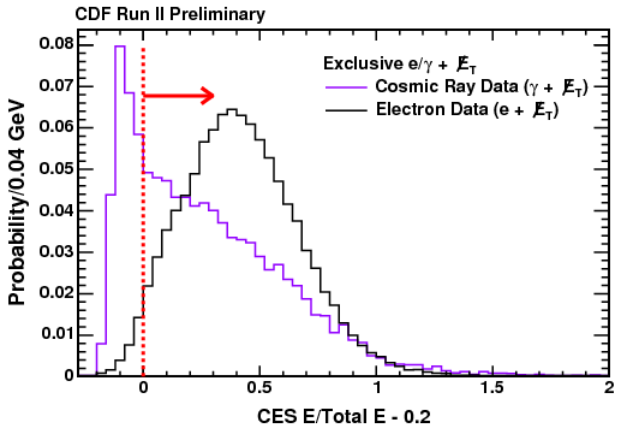

Fig. B.3. CES energy/total energy for electrons coming from collision events (black line) and cosmic ray photons identified (pink line) by reversing the muon-stub veto. We note that high energy objects coming from the collision deposit a larger fraction of their energy in the CES detector then cosmic ray photons do.

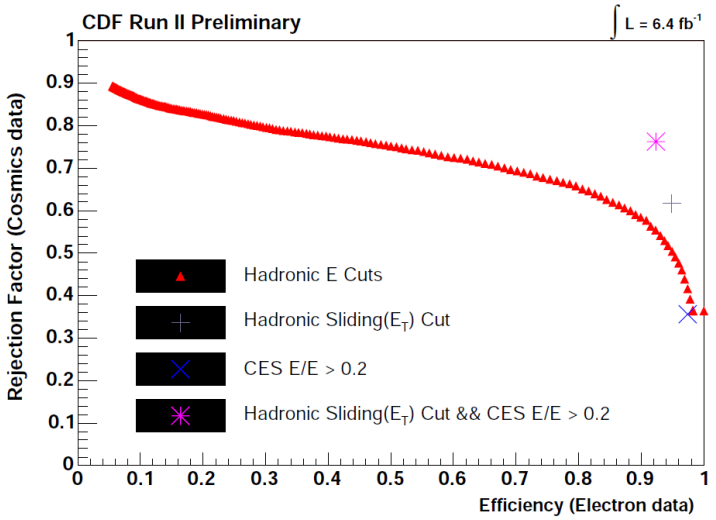

Fig. B.4. Rejection versus efficiency curve for the combination of the hadronic energy cut and the CES energy fraction taken together resulting in a 92% efficency for a 76% rejection of cosmic ray photons.

APPENDIX C

COMPARISON OF THE NEW RESULTS WITH THE PRELIMINARY 2008 RESULTS

The first question that arises following the results presented in Section 7.2 might be, "what happened to the excess shown in the preliminary 2008 result?". As discussed in Section 1.5 an "excess" number of events above background expectations of 67 events with a preliminary signifcance of $N_\sigma \sim 4$ was reported only using $\sim$4.8 fb^{-1} of data. However, as we have learned, much of this excess was due to a poor background estimation technique, as well as due sources of biased SM backgrounds.

With the addition of numerous background rejection methods (see Section 5.4) and a new data driven background estimation procedure (see Section 6.5) to predict the mean of the wrong vertex we end up finding an excess of 65 events. However, unlike before, we have an uncertainty on the mean of the wrong vertex leading to this excess having a much smaller significance of $N_\sigma \sim$1.6.

Figure C.1 shows how the excess of events for both the 2008 result (4.77 fb^{-1}) and the updated result (6.3 fb^{-1}) can "look" much more compelling when we make the incorrect assumption that the wrong vertex mean should be 0.0 ns. The 2008 result in Figure C.1 was generated using the exclusive γ+$\not\!\!E_T$ presample defined in Table 2.12 and the updated 2012 result was selected using the cuts defined in Table 5.3 with the updated background rejection methods implemented.

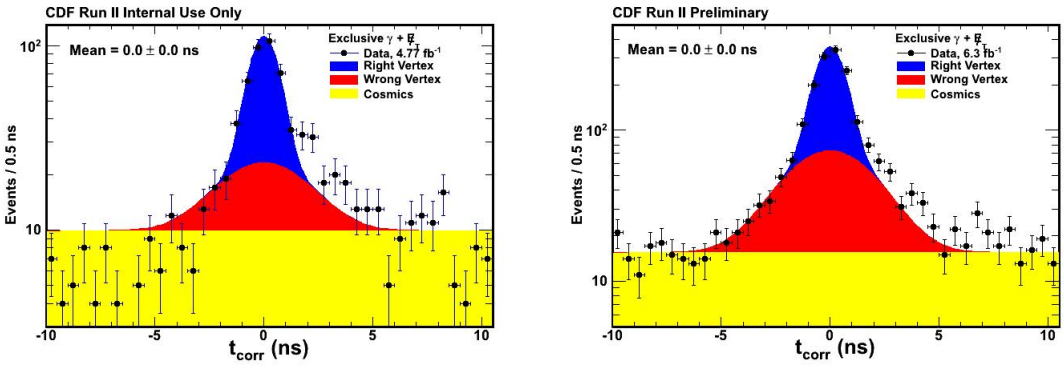

Fig. C.1. Side by side look at the t_{corr} distribution for the Exclusive $\gamma_{delayed}$+$\not\!\!E_T$ final state comparing the 2008 result (LHS) with the updated 6.3 fb^{-1} result (RHS) where we assume a wrong vertex mean = 0.0 ns for both samples. Thus, illustrating how this assumption can lead to the errant conclusion of an excess number of events in the signal region (2 ns to 7 sns).

In addition to having a much more robust background prediction which takes into account the uncertainty in our prediction, we have also introduced three new analysis level vetos which remove events that have a large timing bias. These cuts are one reason that the excess number of events found in the signal region does not simply scale with the luminosity.

Figure C.2 shows the timing distribution for events that fail the large z veto introduced in Section 5.4.3. This veto rejects events that have evidence of activity coming from a vertex that occurs at $|z|$ >60 cm. The mean of the wrong vertex distribution found to be shifted to 1.4 ns. This shift in the t_{corr}, if left in our final sample, would introduce a large timing bias.

Figure C.3 shows the timing distribution for events that fail the $e \rightarrow \gamma_{fake}$ veto (ΔR_{Pull}) outlined in Section 5.4.2. These events are likely coming from electrons

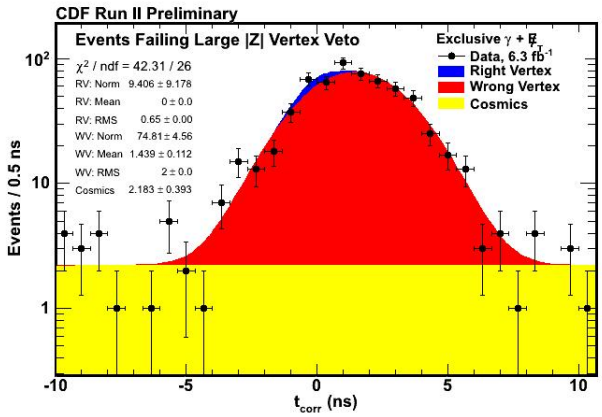

Fig. C.2. Exclusive γ+$\not\!\!E_T$ events which fail the Large z vertex veto. These events have a clear bias to large t_{corr} times and thus contributed to the excess seen in the preliminary study done in 2008.

which underwent a bremsstrahlung interaction and thus register a fake photon in the detector. We use the same background estimation procedure outlined in Section 6.5 to determine the mean of the wrong vertex from the no vertex corrected time (t^0_{corr}) demonstrating another example of how well this method predict the timing distribution. In the previous result from 2008, these events would have still been present in our final sample with a wrong vertex mean of ∼0.41 ns thus "enhancing" the appearent timing bias.

Finally, it should be noted that the new calibration procedure, which calibrates on corrected time rather than on t^0_{corr}, also has an effect "reducing" the previously observed excess. This can be seen in Table C.1 where we remove both the large z veto and the $e \to \gamma_{fake}$ veto as well as go back to the previous definition of E_T and $\not\!\!E_T$ where these quantities were defined relative to the highest ΣP_T vertex. We note

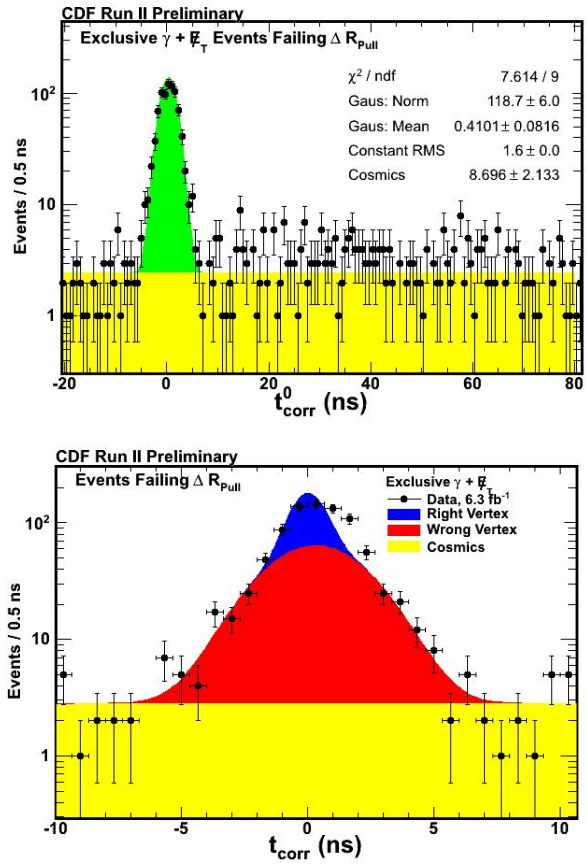

Fig. C.3. Exclusive $\gamma_{delayed} + \not\!\!E_T$ events which fail the ΔR_{Pull} veto. These events, likely coming from W$\rightarrow e\nu \rightarrow \gamma_{fake} + \not\!\!E_T$ (see Section 5.4.2, have a clear bias to large t_{corr} times and thus contributed to the excess seen in the preliminary study done in 2008. (Top) "No Vertex" corrected time (t^0_{corr}) for events that fail the $e \rightarrow \gamma_{fake}$ veto with a mean of 0.41 $\pm$ 0.08 ns and (Bottom) The t_{corr} distribution using the no vertex mean time.

here that by using the E_T and $\not\!\!E_T$ definitions relative to the highest ΣP_T vertex does not allow us to estimate the mean of the wrong vertex using the "no vertex" sample.

When we revert to the "old" definitions, i.e. remove new calibrations, defining E_T relative to the highest ΣP_T vertex, removing large $|z|$ veto, remove new $e \rightarrow \gamma_{fake}$

Original Set of Cuts and *Old* Calibrations		
Number of Events in the Signal Region	Number of Events in the Control Region	"Excess" (Signal - Control)
506	335	171
Original Set of Cuts and *New* Calibrations		
Number of Events in the Signal Region	Number of Events in the Control Region	"Excess" (Signal - Control)
447	318	129

Table C.1

Summary of the effect of the calibrations on the number of events observed in the control and signal region. Note: These numbers reflect removing both the large z veto and the $e \rightarrow \gamma_{fake}$ veto as well as go back to the previous definition of E_T and $\not\!\!E_T$ where these quantities were defined relative to the highest ΣP_T vertex. Having used the E_T and $\not\!\!E_T$ definitions relative to the highest ΣP_T vertex does not allow us to estimate the mean of the wrong vertex using the "no vertex" sample.

veto; we observe 506 events in the signal region (2 ns to 7 ns) and 335 events in the control region (-7 ns to -2 ns). Using the old assumption of a wrong vertex mean = 0.0 ns this would suggest an "excess" of events of 171 events. We now reapply the new calibrations but continue to keep the "old" variable definitions (i.e. define E_T relative to the highest ΣP_T vertex, removing large $|z|$ veto, remove new $e \rightarrow \gamma_{fake}$ veto) and observe that there are 447 events in the signal region and 318 events in the control region, leaving an "excess" of 129 events.

This result roughly implies that some 42 events of the 171 are due to poorly calibrated vertex and EMTiming times. Of course this is an oversimplification since we know the assumption that the number of events in the control region should equal the number of events in the signal region for SM backgrounds is false. However, it

does allow us to appreciate the importance of the calibrations in effecting the final answer.

VITA

Jonathan Asaadi [redacted] He graduated from the University of Iowa with a B.S. in Physics in June 2004. He joined Texas A&M in the fall of 2004 as a graduate student in Physics. He received his M.S. in December 2007, specializing in experimental particle physics. In the spring of 2008 he began working as part of the CDF collaboration in experimental particle physics. He received a Ph.D. in Physics in August 2012. His permanent mailing address is the Department of Physics, TAMU MS4242, College Station, TX 77843.